

# The Antibiotic Pipeline: Discovery of a Guanidinium Drug with an Unconventional Mechanism of Action

Dominik Schum

Vollständiger Abdruck der von der TUM School of Natural Sciences der Technischen  
Universität München zur Erlangung eines  
Doktors der Naturwissenschaften (Dr. rer. nat.)  
genehmigten Dissertation.

Vorsitz: Prof. Dr. Martin Zacharias

Prüfende der Dissertation:

1. Prof. Dr. Stephan Sieber
2. Prof. Dr. Matthias Feige

Die Dissertation wurde am 04.09.2024 bei der Technischen Universität München eingereicht  
und durch die TUM School of Natural Sciences am 11.10.2024 angenommen.



## Introductory Remarks

Under the direction of *Prof. Dr. Stephan A. Sieber*, this doctoral dissertation was completed between February 2021 and August 2024 at the Chair of Organic Chemistry II, Technical University of Munich (TUM).

ChatGPT-4o was used as a language tool without changing the content.

Chemical synthesis and analytics of all guanidinium derivatives were done by *Franziska A. V. Elsen* and can be found, together with all relevant information about author contributions and acknowledgments, in the below-mentioned publication.

Results and methods described in this thesis resulted in the publication of the following peer-reviewed article, published in *JACS Au*, accepted 24<sup>th</sup> June.

### *Publication*

**Dominik Schum\***, Franziska A. V. Elsen\*, Stuart Ruddell, Kenji Schorpp, Howard Junca, Mathias Müsken, Shu-Yu Chen, Michaela K. Fiedler, Thomas Pickl, Dietmar H. Pieper, Kamyar Hadian, Martin Zacharias, Stephan A. Sieber<sup>+</sup>. 'Screening Privileged Alkyl Guanidinium Motifs under Host-Mimicking Conditions Reveals a Novel Antibiotic with an Unconventional Mode of Action.' *JACS Au* (2024).

\* contributed equally

<sup>+</sup> corresponding author

"Reprinted with permission from **Schum, Dominik, et al. 'Screening Privileged Alkyl Guanidinium Motifs under Host-Mimicking Conditions Reveals a Novel Antibiotic with an Unconventional Mode of Action.'** *JACS Au* (2024). Copyright 2024 American Chemical Society."

### *Publications not mentioned in this dissertation*

Maximilian Hohmann\*, Valentina Brunner, Widya Johannes, **Dominik Schum**, Laura M. Carroll, Tianzhe Liu, Daisuke Sasaki, Johanna Bosch, Thomas Clavel, Stephan A. Sieber, Georg Zeller, Markus Tschurtschenthaler<sup>+</sup>, Tobias A. M. Gulder<sup>+</sup>, Klaus-Peter Janßen<sup>+</sup> (2024). 'Bacillamide D produced by *Bacillus cereus* from the mouse intestinal bacterial collection (miBC) is a potent cytotoxin in vitro.' *Communications Biology*, 7(1) (2024), 655.

## *Conference Presentation*

'Target Analysis of Guanidinium Antibiotics':

Poster at the 13<sup>th</sup> International Activity-Based Protein Profiling Meeting, 17<sup>th</sup> – 19<sup>th</sup> July 2023,  
Tel Aviv, Israel

## ABSTRACT

Antimicrobial resistance poses an urgent threat to humanity, as bacteria can quickly develop mechanisms to resist antibiotics, rendering these drugs ineffective. Therefore, there is a critical need for new antibacterials with novel mechanisms of action to stay ahead in the fight against pathogens.

In this thesis, a new antibiotic targeting methicillin-resistant *Staphylococcus aureus* (MRSA) was identified, and its mechanism of action was thoroughly investigated. Previous studies indicated that guanidinium compounds increase cellular accumulation, especially in Gram-negative bacteria, making them interesting drug candidates for antibiotic development. By preselecting guanidinium motifs as screening compounds in the presence of sodium bicarbonate as a host-mimicking condition, the hit rate of the screening was successfully increased by 13% compared to the screening without NaHCO<sub>3</sub>. The most promising compound, **L15**, exhibited the highest activity against MRSA (MIC = 1.5 μM) and *Escherichia coli* (MIC = 12.5 μM). Structure-activity relationship studies then revealed that the guanidinium group is essential for **L15**'s antibacterial activity.

To determine the mechanism of action of **L15**, extensive molecular biological and biochemical studies were conducted. Affinity-based protein profiling identified the essential signal peptidase IB (SpsB) as a target, which was validated through activity assays and binding site identification studies. The binding mode was further explored using docking and molecular dynamics. Proteomics studies supported these findings, revealing an upregulation of autolysins, enzymes that degrade the cell wall by breaking down peptidoglycan. This led to an upregulation of proteins involved in cell wall stress and remodeling. In addition, electron microscopy studies indicated an accumulation of cytoplasmic proteins likely due to dysfunctional protein secretion. The data suggest that **L15** targets the bacterial cell membrane, either directly by interacting with and causing membrane depolarization or indirectly through SpsB activation, leading to dysregulated protein secretion and, ultimately, cell death.

Overall, this thesis underscores the importance of rethinking antibiotic development through unconventional strategies to discover novel antibiotics. In-depth mechanism of action studies enhance our understanding of bacterial targets and their physiological roles, which can be leveraged to develop more effective antibiotics.

# ZUSAMMENFASSUNG

Die antimikrobielle Resistenz stellt eine dringende Bedrohung für die Menschheit dar, da Bakterien schnell Mechanismen entwickeln können, um gegen Antibiotika resistent zu werden, wodurch diese Medikamente unwirksam werden. Daher besteht ein dringender Bedarf an neuen antibakteriellen Wirkstoffen mit neuartigen Wirkmechanismen, um im Kampf gegen Krankheitserreger einen Schritt voraus zu sein.

In dieser Arbeit wurde ein neues Antibiotikum gegen den Methicillin-resistenten *Staphylococcus aureus* (MRSA) identifiziert und seine Wirkungsweise eingehend untersucht. Frühere Forschungsarbeiten deuteten darauf hin, dass Guanidinium-Verbindungen die zelluläre Akkumulation insbesondere in gramnegativen Bakterien erhöhen, was sie zu attraktiven Kandidaten für die Entwicklung von Antibiotika macht. Durch die Vorauswahl von Guanidinium-Motiven als Screening-Verbindungen in Gegenwart von Natriumhydrogencarbonat als wirtsähnliche Bedingung konnte die Trefferquote des Screenings im Vergleich zum Screening ohne NaHCO<sub>3</sub> um 13 % erhöht werden. Die vielversprechendste Verbindung, **L15**, zeigte die höchste Aktivität gegen MRSA (MIC = 1,5 µM) und *Escherichia coli* (MIC = 12,5 µM). Studien zur Struktur-Aktivitäts-Beziehung zeigten, dass die Guanidinium-Gruppe für die antibakterielle Aktivität von **L15** entscheidend ist.

Um den Wirkmechanismus von **L15** zu bestimmen, wurden umfangreiche molekularbiologische und biochemische Studien durchgeführt. Durch affinitätsbasierte Proteinprofilierung wurde die essenzielle Signalpeptidase IB (SpsB) als Ziel identifiziert, welche durch Aktivitätsassays und Studien zur Identifizierung der Bindungsstelle validiert wurde. Der Bindungsmodus wurde mit Hilfe von Docking und Molekulardynamik weiter erforscht. Proteomik-Studien bestätigten diese Ergebnisse und zeigten eine Hochregulierung von Autolysinen, Enzymen, die die Zellwand durch den Abbau von Peptidoglykan degradieren. Darüber hinaus zeigten elektronenmikroskopische Untersuchungen eine Anhäufung von zytoplasmatischen Proteinen, die wahrscheinlich auf eine gestörte Proteinsekretion zurückzuführen ist. Die Daten deuten darauf hin, dass **L15** auf die bakterielle Zellmembran abzielt, entweder direkt durch Interaktion mit und Depolarisierung der Membran oder indirekt durch Aktivierung von SpsB, was zu einer gestörten Proteinsekretion und schließlich zum Zelltod führt.

Insgesamt unterstreicht diese Arbeit, wie wichtig es ist, die Entwicklung von Antibiotika durch unkonventionelle Strategien neu zu überdenken, um neue Antibiotika zu entdecken. Eingehende Studien über Wirkmechanismen verbessern unser Verständnis der bakteriellen

Zielstrukturen und ihrer physiologischen Rolle, was zur Entwicklung wirksamerer Antibiotika genutzt werden kann.

## Danksagung

Ich kann mich noch genau an den Tag zurück erinnern, an dem ich meine Masterarbeit der OCII-Gruppe von *Stephan* online präsentiert habe und daraufhin auch mit einzelnen PhDs gesprochen habe. Die Entscheidung meinen Doktor zu machen war nicht selbstverständlich, aber ich bin sehr dankbar dafür, dass mir dieser Weg ermöglicht wurde.

An dieser Stelle möchte ich mich ganz herzlich bei meinem Doktorvater, *Stephan Sieber*, bedanken: für sein Vertrauen mich in seine Gruppe trotz der zweieinhalb jährigen Pause vom akademischen Umfeld aufzunehmen, für seine Unterstützung bei meinen Projekten, für seine Umsicht und Freundlichkeit. Ich habe mich in der Zeit während meiner Doktorarbeit sehr gut aufgehoben gefühlt, und konnte zusätzlich meine persönlichen Interessen verfolgen.

Das Arbeitsumfeld in der OCII-Gruppe ist einzigartig: die Bereitschaft sich gegenseitig zu unterstützen, füreinander da zu sein, Zeit bei gemeinsamen Aktivitäten zu verbringen, Spaß zu haben, viel zu lachen. Es macht unheimlich viel Freude in die Arbeit zu gehen, wenn man weiß, dass man dort gemeinsam in einer sehr angenehmen und lockeren Atmosphäre arbeiten kann und sich angenommen fühlt. Eines meiner persönlichen Highlights waren die viele Kuchen und die regelmäßigen Kaffeepausen. Ich möchte mich bei allen ehemaligen und aktuellen PhDs, PostDocs und Masteranden, welche meine Zeit am Lehrstuhl sehr bereichert haben, bedanken: *Yasmine, Franzi, Leo, Laura, Konsti, Alex, Max, Sara, Antonia, Nina W., Maxi, Joshua, Martin K., Wei, E, Katrin, Mary, Markus, Tao, Annina, Robin, Aleksandra, Manu, Micha, Thomas G., Ines, Caro, Thesi, Patta, Stewie, Martin P., Isabel, Jan, Davide, Angela, Till, Didi, Seppi, Zollo, Robert, Frani, Kora, Andrei, Ricky, Aziza, Ekaterina, Thomas S., Raffi, Vicky* und *Sissy*. Zusätzlich möchte ich mich ganz herzlich bei meinen Praktikanten *Thomas S., Niels, Manu* und *Konstantin S.*, und bei meinen HiWis *Rahel, Anna* und *Leo* für ihre Hilfe bei meinen Projekten bedanken!

Ohne euch alle wäre und ist die OCII-Gruppe nicht das was sie ist! Jeder einzelne trägt dabei einen Teil zur Gesamtheit bei! Vielen herzlichen Dank auch an *Nina B.* für die Organisation im AK Sieber und alles darüber hinaus, an unsere ehemalige Sekretärin *Christina* und ihre Nachfolgerin *Babsi*, an unsere technische Assistenz *Mona* und *Katja*, welche für unsere Arbeit unerlässlich sind und dafür sorgen, dass alles bestmöglich funktioniert.

Besonderen Dank möchte ich *Yasmine, Davide, Isabel, Rahel* und *Martin P.* aussprechen. Mit euch habe ich sehr viel Zeit verbracht, sei es bei gemeinsamen Mittagessen, Tee- und Kaffeepausen, tiefen Gesprächen, privaten Aktivitäten. Ihr habt mich während meines PhDs und darüber hinaus auf unterschiedliche Weise unterstützt, und habt mir geholfen meinen persönlichen Weg zu beschreiten. Danke für eure Freundschaft und für die gemeinsame Zeit!



Zudem möchte ich all meinen Freunden aus dem Studium, meinen Münchener Freunden, und ehemaligen Schulfreunden für die schöne Zeit während meiner Doktorarbeit bedanken.

*Thea, Christian* und *Janina*: Ihr seid unglaubliche tolle Menschen! Ich bin sehr dankbar dafür euch als Freunde zu haben! Ich brauche an dieser Stelle auch nicht mehr zu sagen. Danke für alles! Ich liebe euch!

*Günter, Patrick* und *Nils*: Ihr seid wie große Brüder für mich! Ich verbringe unheimlich gerne Zeit mit euch! Danke dass ihr Teil meines Lebens seid!

Großer Dank gilt auch für meine Familie, meine Eltern, Geschwister und Verwandten, die immer für mich da sind und mich trotz räumlicher Distanz stets auf meinem Weg begleiten. Ich bin sehr dankbar dafür, zu wissen, dass ich nicht alleine bin und dass ihr immer in Reichweite seid. Danke an euch, Mama und Papa, dass ihr mir und meinen Brüdern eine wunderbare Kindheit ermöglicht habt!

Zuletzt möchte ich mich bei dir, *Mark*, bedanken! Für alles was du mir gibst, was du mir gezeigt hast und ich auf meinem persönlichen Weg gelernt habe. Für deine grenzenlose Unterstützung, dein umfassendes Verständnis, die gemeinsame Zeit miteinander, für viele tolle Tage, jeden kleinen Moment. Ich bin unheimlich dankbar dafür mit dir zusammen durchs Leben zu gehen, an deiner Seite zu wachsen und neue Erfahrungen zu machen. Danke dafür, dass du so bist wie du bist!

*'Enjoy the little things in life because one day you'll look back and realize they were the big things.'*

– Kurt Vonnegut

## Table of Content

### I. INTRODUCTION

1. Antimicrobial Resistance Crisis .....	1
2. Finding Novel Antibiotics – Strategies for Antibiotic Mining.....	3
3. Guanidine-Bearing Molecules as Antibiotic Drugs.....	6
4. Antibiotic Target Identification by Chemical Proteomics .....	9
5. Aim of this Doctoral Thesis .....	11

### II. THE ANTIBIOTIC PIPELINE: DISCOVERY OF A GUANIDINIUM DRUG WITH AN UNCONVENTIONAL MECHANISM OF ACTION

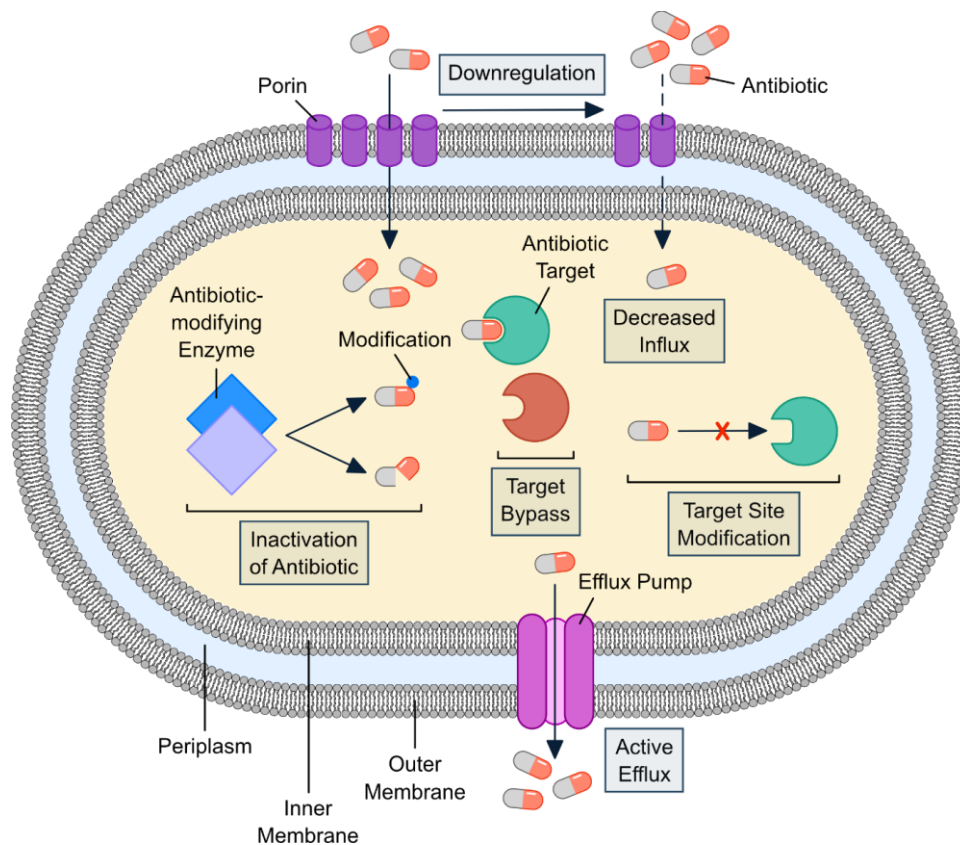
1. Results and Discussion .....	12
1.1. Screening of Guanidinium Compounds under Host-Mimicking Conditions and Antimicrobial Activity of Hit Compounds .....	12
1.2. Antimicrobial Activity of L15's Chemical Derivatives .....	14
1.3. Bacterial Uptake and Influence of Cell Density on Antimicrobial Activity of L15 .....	16
1.4. Cytotoxic and Hemolytic Activity of L15 and Derivatives .....	17
1.5. Membrane-Targeting Properties of L15 and Derivatives .....	19
1.6. Kinetics of L15's Action, Resistance Development of L15-Treated <i>S. aureus</i> and Genomic Sequencing of L15-Resistant Mutants .....	22
1.7. Growth of <i>S. aureus</i> under L15 Stress and Global Proteome Changes.....	25
1.8. Protein Target Identification by Affinity-Based Protein Profiling .....	31
1.9. Morphological Changes in L15-Treated <i>S. aureus</i> by Electron Microscopy .....	33
1.10. Target Validation Studies by an <i>in vitro</i> FRET Assay and Molecular Dynamics..	35
1.11. Binding Site Identification Studies by isoDTB Affinity-Based Protein Profiling.....	40
2. Conclusion .....	42
3. Supplementary Information.....	43
3.1. Supplementary Tables S1 – S2 .....	43

4.	Methods .....	59
4.1.	HTS Guanidinium Library and Screen .....	59
4.2.	Chemical Compounds .....	59
4.3.	Cell Culture.....	59
4.4.	Bacterial Strains .....	59
4.5.	Plasmids .....	60
4.6.	Minimum Inhibitory Concentration Assay .....	60
4.7.	Hemolysis Assay in Sheep Blood .....	61
4.8.	Human Metabolic Activity Assay.....	61
4.9.	Membrane Depolarization Assay .....	62
4.10.	Electron Microscopy Experiments .....	62
4.11.	Time-Kill Assay .....	63
4.12.	Minimum Bactericidal Concentration.....	63
4.13.	Frequency of Resistance Assay .....	63
4.14.	Growth Curves Experiments.....	64
4.15.	Bacterial Genomics (Sequencing of FoR mutants).....	64
4.16.	Gel-based Fluorescent Labeling.....	65
4.17.	Preparative Labeling for LC-MS/MS Analysis .....	66
4.18.	Full Proteome Analysis.....	67
4.19.	LC-MS/MS Measurements and Data Analysis with timsTOF Pro .....	69
4.20.	Expression and Purification of MBP-tagged <i>S. aureus</i> SpsB in <i>E. coli</i> .....	71
4.21.	Binding Site Identification by isoDTB A/BPP .....	72
4.22.	Preparation of Membrane Fractions Harboring <i>S. aureus</i> SpsB in <i>E. coli</i> .....	76
4.23.	FRET-based SpsB Assay with Membrane-bound SpsB.....	77
4.24.	Molecular Dynamics (MD) Simulations.....	77
5.	Abbreviations .....	79
6.	References .....	83
7.	License Agreement .....	99

# I. INTRODUCTION

## 1. Antimicrobial Resistance Crisis

Antimicrobial resistance (AMR) occurs when microorganisms become less susceptible to medications over time<sup>1</sup>. This aggravates treatment efficacy, leading to a longer persistence of infections and a higher probability of disease transmission. Mutual engagement of microorganisms and their environment led to the evolution of intriguing defense mechanisms over millions of years<sup>2,3</sup>. As a result, resistance development existed long before the introduction of antibacterials to treat infectious diseases<sup>4</sup>. Today, pathogenic bacteria are becoming increasingly difficult to treat due to natural and acquired resistance mechanisms<sup>5</sup> (Figure 1), rendering antibiotics ineffective and causing a rising death rate from bacterial infections. The scale of AMR was evident in 2019, directly causing 1.27 million global deaths and being associated with nearly 5 million deaths<sup>6</sup>.



**Figure 1:** The molecular mechanisms behind acquired antibiotic resistance in bacteria include several strategies. One common method is the inactivation of the antibiotic through chemical modification or enzymatic degradation. Bacteria can also bypass the antibiotic target by expressing an alternative protein with the same function. Additionally, the target itself can be altered to prevent the antibiotic from binding. Resistance can also result from decreased antibiotic influx due to the downregulation of porins, and active efflux which expel the antibiotic from the cell. This figure was created with Affinity Designer 2.0

By 2050, this number could rise to 10 million deaths per year, making AMR one of the leading causes of death worldwide<sup>7</sup>. Multidrug-resistant bacteria are particularly concerning due to limited treatment success with commonly used antibiotics. The World Health Organization (WHO) recently released a report on bacterial priority pathogens to guide research and development in combating the AMR crisis<sup>8</sup>. This report updates the high-burden bacteria list from 2017, highlighting the Gram-positive bacteria *Enterococcus faecium*, *Staphylococcus aureus*, and the Gram-negative bacteria *Klebsiella pneumoniae*, *Acinetobacter baumannii*, *Pseudomonas aeruginosa*, and *Enterobacter* species (acronym ESKAPE) as still belonging to the high-risk group, underscoring the urgent need for new antibiotics and the minor improvements in treating those species within the last years.

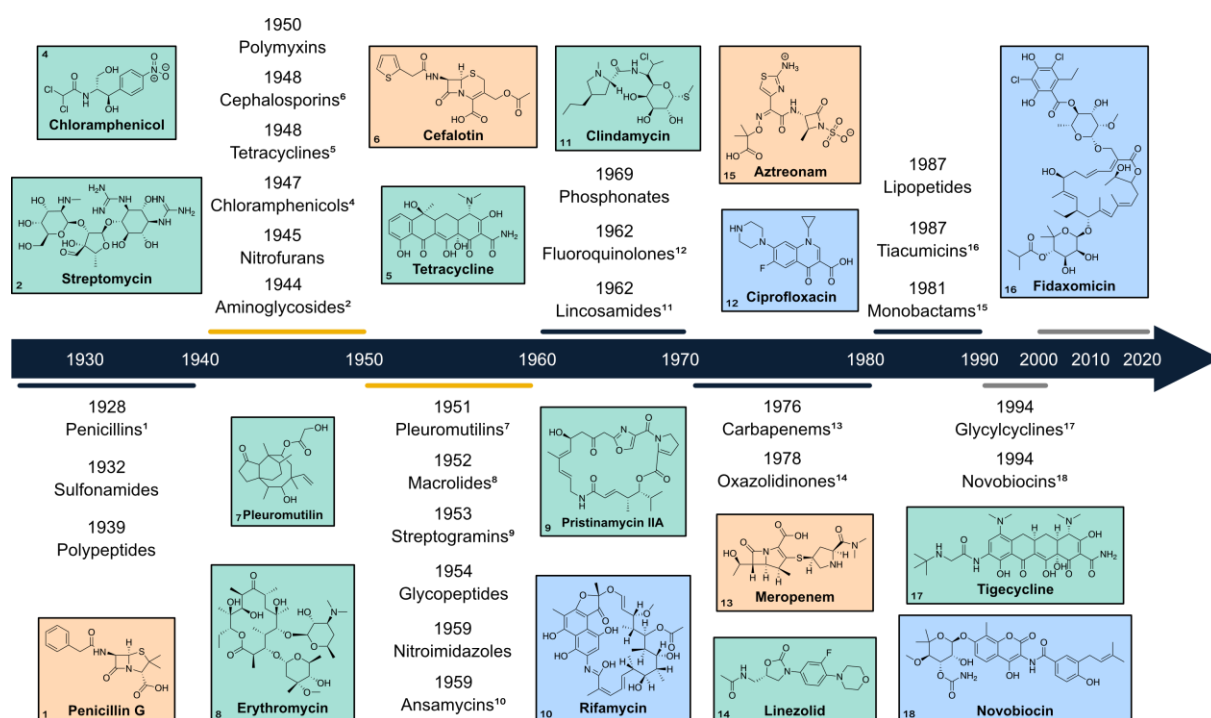
Unfortunately, the clinical pipeline of antibacterial products is insufficient to address AMR, with only 97 candidates in clinical development (phase I-III), according to a recent WHO report<sup>9</sup>. Most developed antibiotics are variations of already existing ones, and only a few novel antibiotic classes have been introduced in the last decades<sup>10,11</sup>. Although bacterial cells are predicted to possess about 300 genes with an essential role<sup>12</sup>, most antibiotics target a narrow range of cellular components<sup>13</sup>, such as protein synthesis, RNA/DNA, the cell wall, and folate metabolism. Resistance develops through random mutations in genes encoding the antibiotic target or affecting the antibiotic's mechanism of action (MoA)<sup>14</sup>. In addition, resistance genes can be transferred among bacteria *via* horizontal gene transfer<sup>15</sup>.

Selective pressure, often due to the overuse of antibiotics in healthcare systems and agriculture, exacerbates resistance development<sup>16,17</sup>. Socio-economic disparities worsen the crisis, especially in low- and middle-income countries (LMICs), where access to antibiotics is limited, but disease rates are higher, making AMR a global issue<sup>18,19</sup>. Pharmaceutical companies face challenges, including (1) a low success rate in discovering new antibacterials<sup>20</sup>, (2) rapid resistance development<sup>21</sup>, and (3) economic and governmental hurdles, comprising regulatory aspects and pricing<sup>22-24</sup>. Beyond the clinical burden, AMR will cause high costs on national healthcare systems in the future<sup>25,26</sup>.

Consequently, policymakers must act now to create new guidelines and take appropriate measures to control this crisis. More conservative antibiotic prescription practices are necessary, reserving antibiotics for cases where common treatments fail<sup>27</sup>, thereby preserving the efficacy of highly effective antibiotics. Companies need more governmental support and financial incentives to combat AMR<sup>28</sup>. Furthermore, promoting the conservative and targeted use of antibiotics and increasing international support for LMICs through awareness campaigns and healthcare improvements are crucial<sup>29</sup>.

## 2. Finding Novel Antibiotics – Strategies for Antibiotic Mining

The discovery of penicillin by Alexander Fleming in 1928 marked the beginning of the modern antibiotic era<sup>30</sup>. However, synthetic sulfonamides were the first antibiotic class used in clinical practice during the 1930s<sup>31</sup>. Most antibiotic classes were discovered by screening natural product extracts during the *Golden Age* of antibiotics (1940 – 1960) and remain in clinical use today (Figure 2). Unfortunately, since 1987, only a few new antibiotic classes have been introduced, and this *Discovery Void* has persisted until today<sup>32</sup>. In the 21<sup>st</sup> century, most of the approved antibiotics are typically derivatives of existing classes, targeting known mechanisms<sup>33</sup>.



**Figure 2:** Timeline showing the history of antibiotic discovery<sup>34–38</sup>. Years of discovery indicate the first report in the literature. Antibiotic targets are color-coded: protein synthesis (green), RNA/DNA (orange), and cell wall (orange). Yellow label = *Golden Age*, grey label = *Discovery Void*. This figure was created with Affinity Designer 2.0.

In natural product-based mining approaches, bacteria are treated with extracts of fermentation broth or natural products to assess a growth inhibition effect, following chromatographic fractionation and structure elucidation of bioactive compounds<sup>39</sup>. A major drawback of this method is the labor-intensive process, often leading to the rediscovery of already-identified antibiotics<sup>40</sup>. Conversely, the growing resistance against most available antibiotics emphasizes the urgent need for developing novel antibiotics with unprecedented MoAs to prevent acquired resistance development<sup>41–44</sup>.

Chemical synthesis approaches have enhanced the efficacy of naturally sourced antibiotics, such as aminoglycosides<sup>45</sup>, tetracyclines<sup>46</sup>,  $\beta$ -lactams<sup>47</sup>, and macrolides<sup>48</sup>, by expanding their

chemical scaffolds. In addition, fully synthetic compounds have broadened the antibiotic spectrum, leading to the discovery of novel classes like quinolones<sup>49</sup> and oxazolidinones<sup>50</sup>. Many natural-derived antibiotics can now be fully synthesized, enabling a more cost-efficient industrial-scale production than fermentative methods<sup>51</sup>. Despite a wide range of screening technologies, whole-cell empirical screenings remain the most efficient, covering all protein targets involved in bacterial killing<sup>52</sup>.

Technological advancements have enabled high-throughput screening<sup>53</sup> (HTS) of chemical libraries in whole cells or through targeted approaches like antisense screening<sup>54</sup>. This method identifies hit compounds not detectable in wild-type strains based on the differential expression of an essential gene. Drug repurposing<sup>55</sup> and virtual screenings also provide valuable tools for antibiotic discovery. The latter approach is guided by computational biology and molecular docking, enabling targeted *in silico* methods, but requires knowledge of the enzyme's 3D structure and active site for effective docking experiments<sup>56</sup>. Although machine-learning approaches exist to tackle these drawbacks<sup>57</sup>, a significant disadvantage of virtual screenings remains their generally weak predictive power, which results in many false positives<sup>58</sup>. Overall, expanding the chemical space and maximizing structural diversity is crucial for identifying novel antibiotics, regardless of the screening technique used<sup>59</sup>. Technological and scientific advances in molecular genomics<sup>60</sup>, combinatorial chemistry<sup>61</sup>, structural biology<sup>62</sup>, and artificial intelligence<sup>63</sup> have expanded the possibilities for antibiotic drug discovery and will aid in addressing the AMR crisis in the future<sup>64</sup>.

Following the decline of novel antibiotics after the *Golden Era*, new screening campaigns were launched but met with limited success<sup>65</sup>, highlighting the need for innovative approaches. Enhancing screening conditions by mimicking the host physiological conditions that bacteria encounter during infection can increase hit rates. For example, sodium bicarbonate, part of the extracellular fluid, was found to potentiate antibiotic activity, as shown in a focused library screen of guanidinium antibiotics<sup>66</sup>. NaHCO<sub>3</sub> can alter bacterial gene expression<sup>67</sup> and dissipate the pH gradient of the cellular membrane, affecting the bacterial proton motive force (PMF). Changes in the PMF influence antibiotic activity by affecting uptake mechanisms or inhibiting efflux<sup>68</sup>. However, the enhancement of antibiotic efficacy in susceptibility testing due to sodium bicarbonate may not apply to all antibiotics, as demonstrated with the macrolide azithromycin in *Salmonella*<sup>69</sup>.

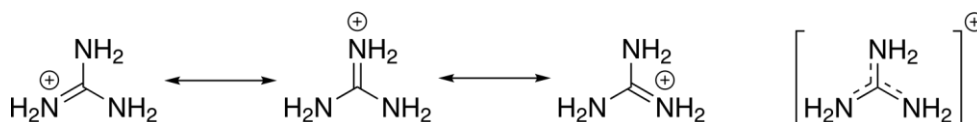
Addressing the restricted uptake of small molecules, particularly in Gram-negative bacteria<sup>70–72</sup>, can be achieved using compounds with functional groups that enhance bacterial uptake. The eNTRY<sup>73</sup> rules provide guidelines for facilitating compound uptake in Gram-negative bacteria, with primary amines<sup>74</sup> and guanidinium<sup>75</sup> groups proving to be promising structural motifs. According to these rules, compounds are more likely to accumulate in Gram-negative



bacteria if they have an ionizable **Nitrogen**, low **Three-dimensionality** (globularity less than 0.25), and fewer than five **Rotatable** bonds. For guanidinium compounds, a higher amphiphilic moment is positively correlated with greater accumulation, and up to eight rotatable bonds are tolerated. The utility of these rules could be already demonstrated by the conversion of narrow-spectrum antibiotics into broad-spectrum ones<sup>76</sup>.

### 3. Guanidine-Bearing Molecules as Antibiotic Drugs

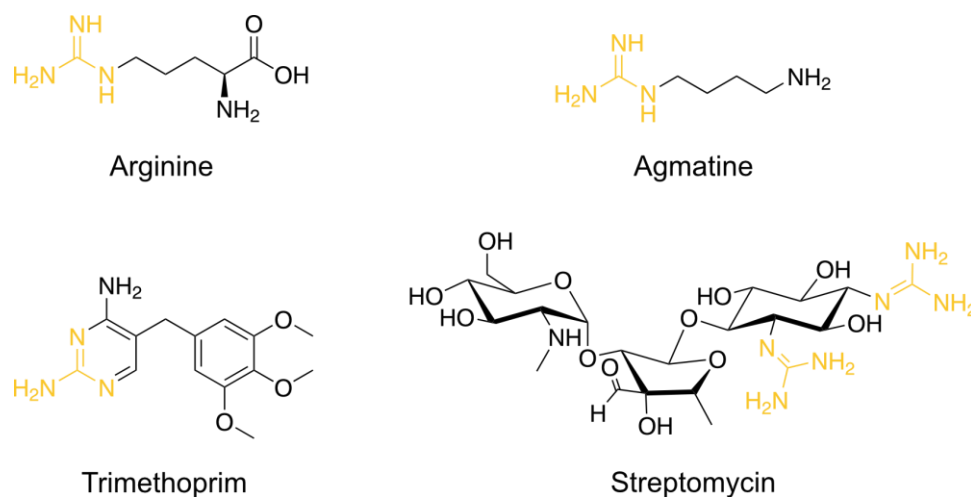
In the 19<sup>th</sup> century, *Strecker* first isolated guanidine as a byproduct of guanine's oxidative degradation<sup>77</sup>. The guanidine functionality exhibits unique chemical properties and structural features, making it valuable for biopharmaceutical and chemical applications<sup>78–80</sup>. Chemically, the guanidine moiety can act as both a nucleophile and an electrophile<sup>81</sup>, depending on the chemical environment. Its high stability and basicity ( $pK_A = 13.6$ ) are due to electron delocalization through various resonance forms in its protonated state (Figure 3).



**Figure 3:** Resonance structures of the guanidine group in its protonated form.

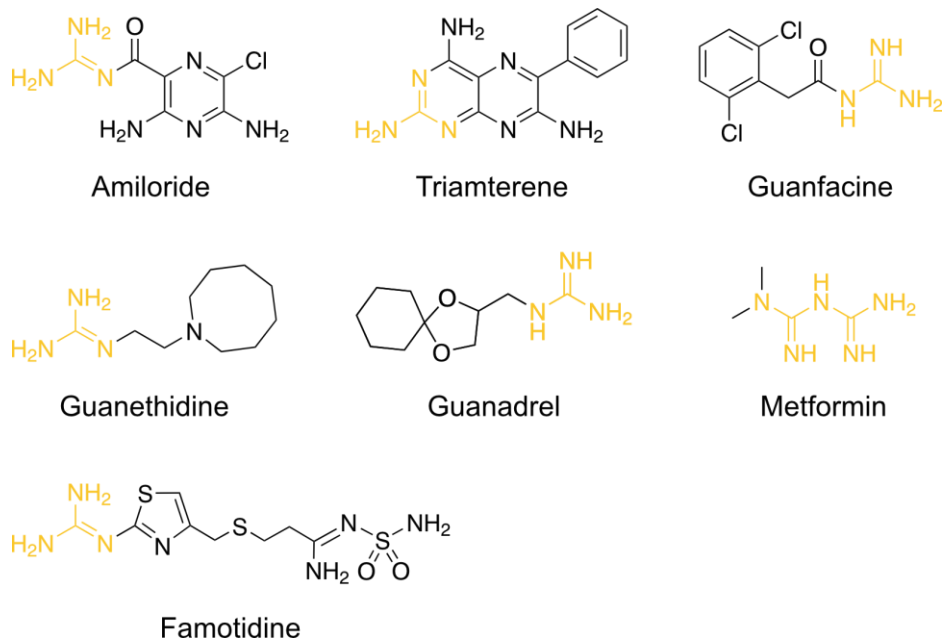
In addition, guanidine can function as H-bond donor, acceptor, and Lewis base. Upon protonation, the guanidine group forms a guanidinium cation with H-bond donor functionality and weak Brønsted acidity<sup>82</sup>. At physiological pH, the guanidine group is protonated and positively charged, allowing it to interact noncovalently with protein targets through H-bonding and interactions with negatively charged anions<sup>83</sup>. Despite some safety concerns with basic molecules having positively charged groups and a ClogP value above 3<sup>84</sup>, which can cause intracellular accumulation of phospholipids<sup>85</sup>, derivatizing guanidine-functionalized compounds enables fine-tuning of their chemical properties and reactivity. These features make guanidine valuable in synthetic and medicinal chemistry.

In nature, the guanidine functionality is ubiquitous in both higher eukaryotes and microorganisms<sup>86</sup>. The diversity of guanidine natural products underscores the importance of bioactive molecules for potential therapeutic applications, highlighting the need for in-depth research into antibiotics derived from natural products. Notable guanidine-bearing molecules include the amino acid arginine, the neurotransmitter agmatine, the synthetic antibiotic trimethoprim, and the natural antibiotic streptomycin (Figure 4).



**Figure 4:** Biomolecules with guanidine functionalities derived from nature (arginine, agmatine, streptomycin) and chemical synthesis (trimethoprim).

Nevertheless, there is a wide variety of guanidine natural products originating from different sources<sup>87</sup>, forming their own class of natural compounds. Researchers utilize the guanidine functionality to synthesize biologically active compounds, many of which exhibit antibiotic activity effective against bacteria<sup>88,89</sup>, mycobacteria<sup>90,91</sup>, fungi<sup>92,93</sup>, *Plasmodium falciparum*<sup>94,95</sup>, and tumor cells<sup>96,97</sup>. For example, guanidinomethyl biaryl compounds have shown significant antibacterial activity in both Gram-positive and Gram-negative strains by targeting the bacterial cell division protein FtsZ, which is an often overlooked antibiotic target<sup>98</sup>. In addition, antimicrobial peptides, which offer a promising approach to treat multidrug-resistant bacteria, can be functionalized with guanidine groups<sup>99</sup>. These positively charged compounds destabilize and disrupt cell membranes through ionic interactions with negatively charged lipids<sup>100</sup>. Furthermore, several human-targeted drugs on the market contain guanidine groups<sup>101–105</sup> (Figure 5). The most well-known example is the biguanide metformin<sup>106</sup>, an antidiabetic drug used as a first-line treatment for type II diabetes.



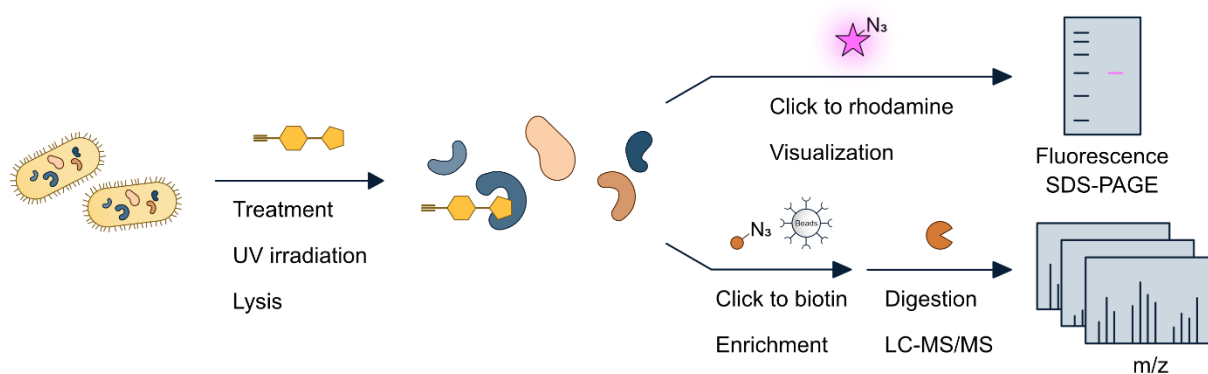
**Figure 5:** List of some human-targeted drugs with guanidine functionalities. Amiloride, triamterene, guanfacine, guanethidine, and guanadrel are cardiovascular drugs to primarily treat hypertension. Metformin is an antidiabetic, and famotidine an antihistaminic drug. The latter is used as an H<sub>2</sub> blocker to reduce stomach acid production.

In summary, molecules with guanidine groups have proven to be efficient in treating various diseases, emphasizing the significant value of this functional group for the biopharmaceutical industry and healthcare systems.

## 4. Antibiotic Target Identification by Chemical Proteomics

Target identification strategies encompass various technologies, including genomics and proteomics<sup>107,108</sup>. In proteomics, technological advances in bioinformatics and mass spectrometry (MS) have led to novel strategies, enhancing specificity, sensitivity, and throughput<sup>109,110</sup>. Among the different MS technologies used in drug discovery<sup>111</sup>, activity-based protein profiling (ABPP) stands out for its unbiased drug target identification. ABPP employs affinity chromatography, followed by high-resolution MS data acquisition and downstream target deconvolution<sup>112</sup>. This technology was pioneered by *Cravatt*<sup>113</sup> and *Bogyo*<sup>114</sup> and initially applied to study large enzyme families and later for target elucidation of small molecules from phenotypic drug screens<sup>115–117</sup>. ABPP is based on activity-based probes (ABPs), which are small molecules featuring a reactive group for covalent attachment to target proteins and an affinity handle for downstream analysis. The reactive group, often an electrophilic moiety or “electrophilic warhead”, interacts with nucleophilic residues in the target protein’s active site. The affinity handle, typically a terminal alkyne or azide, ensures chemical inertness and minimal interference in biological systems. Probe-labeled proteins can be functionalized with fluorophores for visualization or affinity tags (e.g., biotin) for pull-down experiments, each carrying an azide functionality, *via* biorthogonal reactions<sup>118</sup>. The copper (I)-catalyzed *Huisgen* cycloaddition, known as the click reaction, combines the azide of the affinity tag with the alkyne of the probe. In 2022, *Sharpless*, *Medal*, and *Bertozzi* were awarded the Nobel Prize in Chemistry for their work on click chemistry and biorthogonal reactions, which are used to study complex cellular processes<sup>119</sup>. The ABP-bound proteins linked to a biotin handle can be enriched using streptavidin before LC-MS/MS analysis. Comparing ABP-treated samples to DMSO controls helps identify drug targets, but additional target validation is needed to confirm the respective protein targets<sup>120</sup>. Especially recent advances in sample processing, including automatization<sup>121</sup> and enrichment on magnetic beads<sup>122</sup>, have streamlined ABPP sample preparation, facilitating direct drug target identification and enhancing the understanding of enzymatic activity and mechanism for future drug design<sup>123</sup>.

However, not all ligandable proteins have nucleophilic residues that can be harnessed for ABPP. To address this, affinity-based probes (A/BPs) of noncovalent drugs have been developed, which can be activated *in situ* using UV irradiation for covalent attachment to target proteins in an affinity-based protein profiling (A/BPP) approach (Figure 6).



**Figure 6:** Schematic representation of affinity-based protein profiling workflow to visualize protein targets by fluorescence SDS-PAGE or target enrichment using mass spectrometry. The probe-labeled proteome is either clicked to rhodamine azide for fluorescence visualization or to biotine azide for protein enrichment using streptavidin beads, following downstream processing and LC-MS/MS analysis. This figure was created with Affinity Designer 2.0.

AfBPs possess a photo-reactive group (e.g., diazirine, aryl azide, or benzophenone) that forms a reactive species upon UV exposure, facilitating binding to nearby protein targets<sup>124</sup>. Of course, while developing A(f)BPs, one must ensure the probe retains its biological activity before conducting A(f)BPP experiments. These approaches have enabled the identification of various drugs and natural products, potentially enhancing the discovery of novel antibiotics<sup>125,126</sup>.

## 5. Aim of this Doctoral Thesis

Given the rapid emergence of bacterial resistance to common antibiotics, there is an urgent need for drugs with novel mechanisms of action to address the impending antimicrobial resistance crisis.

The goal of this doctoral thesis was to (1) discover a novel guanidinium antibacterial drug effective against methicillin-resistant *Staphylococcus aureus* and (2) elucidate its mechanism of action. Through enhanced screening conditions, a hit compound was identified. Initial structure-activity relationship studies offered valuable insights into the compound's structural characteristics, which can be leveraged for future drug optimization. Subsequent in-depth biochemical analysis further characterized the compound's profile, and mechanism of action studies pinpointed the cellular target, which was validated through comprehensive follow-up studies.

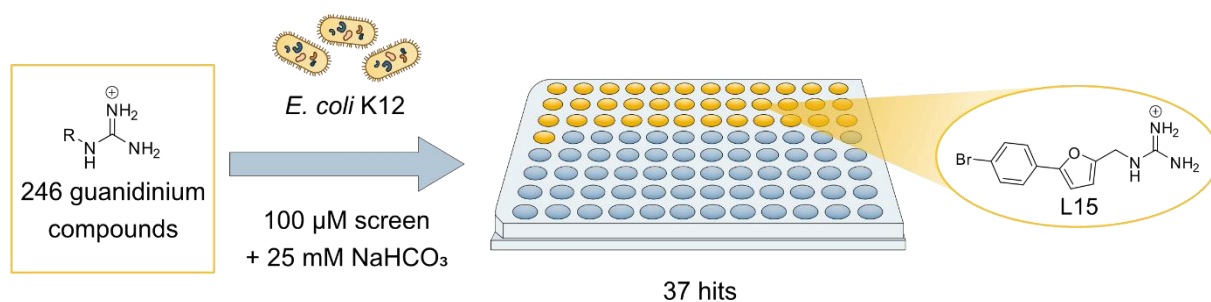
In summary, this streamlined workflow enabled a thorough analysis of a novel guanidinium antibiotic and shed light on its mechanism of action.

## II. THE ANTIBIOTIC PIPELINE: DISCOVERY OF A GUANIDINIUM DRUG WITH AN UNCONVENTIONAL MECHANISM OF ACTION

### 1. Results and Discussion

#### 1.1. Screening of Guanidinium Compounds under Host-Mimicking Conditions and Antimicrobial Activity of Hit Compounds

To encounter the unmet need to target Gram-negative bacteria, a screening library of 246 commercially available guanidinium compounds was designed by *Stuart Ruddell* and used for this study. The guanidinium group as a guiding motif was chosen to enhance cellular uptake and to strengthen H-bond interactions with protein targets<sup>75,86</sup>. The underlying principle is based on the previously postulated eNTRY rules, which are guidelines for compound accumulation in Gram-negative bacteria<sup>74</sup>. The library was first tested in *E. coli* K12 (LB medium) at a concentration of 100  $\mu$ M by *Kenji Schorpp* (Figure 7).

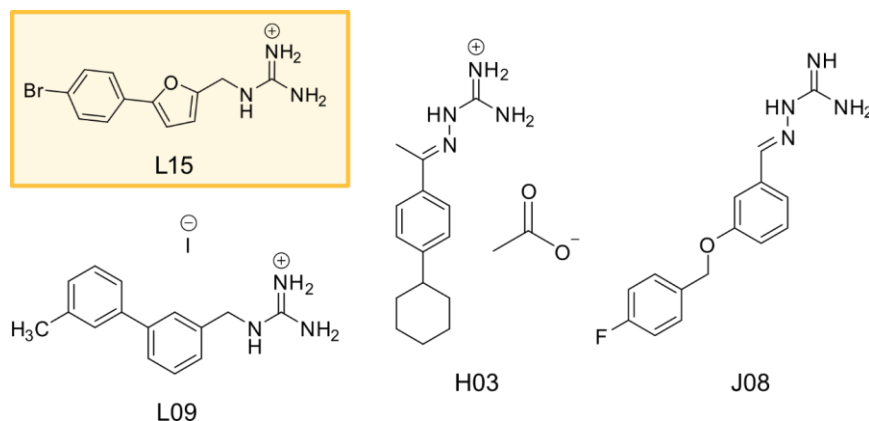


**Figure 7:** Schematic representation of the HTS. A guanidinium library comprising 246 compounds was screened in *E. coli* K12 using 25 mM  $NaHCO_3$  as an additive. The structure of the hit compound L15 is shown. This figure was adapted from a previous study<sup>66</sup>.

This screen revealed six hit molecules that prevented bacterial growth completely. Importantly, the addition of 25 mM  $NaHCO_3$  further improved the antibiotic hit rate up to 37 compounds (Table S1), demonstrating that screening under host physiological conditions is an important need to enhance the success rate of antibiotic libraries<sup>67,68</sup>.

To narrow down the number of antibiotic hits, two additional screens at 50  $\mu$ M and 20  $\mu$ M were performed, and the four most potent molecules (L15, H03, J08, and L09, Figure 8) were investigated in subsequent studies.





**Figure 8:** Chemical structures of the four most potent compounds **L15**, **H03**, **J08**, and **L09**. This figure was adapted from a previous study<sup>66</sup>.

Minimum inhibitory concentrations (MICs) were determined in a panel of 12 Gram-positive and Gram-negative pathogens to evaluate the spectrum of their antibiotic activity (Table 1).

**Table 1:** Biological activity of **L15**, **H03**, **J08**, and **L09** in a panel of pathogenic bacterial strains, including ESKAPE pathogens, in the presence of 25 mM NaHCO<sub>3</sub>(\*). The data represent average values of n = 3 biologically independent experiments per compound. This figure was adapted from a previous study<sup>66</sup>.

Bacterial strain	MIC [ $\mu$ M]* <b>L15</b>	MIC [ $\mu$ M]* <b>H03</b>	MIC [ $\mu$ M]* <b>J08</b>	MIC [ $\mu$ M]* <b>L09</b>
<b><i>Escherichia coli</i> K12</b>	<b>12.5</b>	<b>50.0</b>	<b>50.0</b>	<b>25.0</b>
<i>Escherichia coli</i> 536	12.5	50.0	50.0	25.0
<i>Escherichia coli</i> CFT073	25.0	50.0	50.0	25.0
<i>Pseudomonas aeruginosa</i> PAO1	> 100	100	> 100	> 100
<i>Acinetobacter baumannii</i> DSM 30007	> 100	50.0	25.0	> 100
<i>Klebsiella pneumoniae</i> DSM 30104	100	25.0	50.0	50.0
<i>Enterobacter cloacae</i> DSM 30054	50.0	25.0	50.0	100
<i>Salmonella enterica</i> serovar enteritidis	> 100	100	100	> 100
<i>Staphylococcus aureus</i> USA300 Lac (JE2)	1.56	6.25	12.5	1.56
<i>Enterococcus faecium</i> DSM 20477	100	6.25	12.5	100
<i>Enterococcus faecium</i> DSM 17050	100	6.25	50.0	> 100
<i>Enterococcus faecalis</i> V583	100	6.25	50.0	> 100
<i>Listeria monocytogenes</i> EGD-e	50.0	3.13	6.25	100

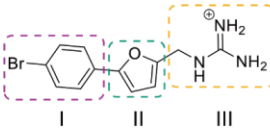
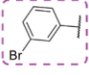
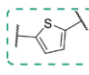
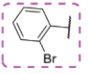
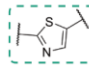
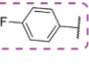
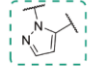
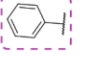
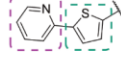
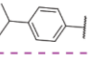
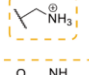
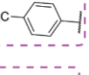
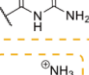
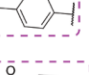
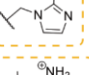
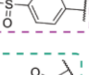
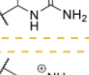

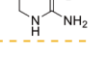
Compounds **J08** and **L09** displayed overall moderate activity against most of the tested bacteria, with some strains being more sensitive to either one of the compounds. The broadest activity spectrum was observed for compound **H03**, displaying low micromolar activity (3.13 – 6.25  $\mu$ M) against all tested Gram-positive strains and moderate activity (25.0 – 50.0  $\mu$ M) against most of the tested Gram-negative strains. The highest antibiotic activity against Gram-positive methicillin-resistant *S. aureus* USA300 Lac (JE2) (MRSA, 1.56  $\mu$ M) and Gram-negative *E. coli* 536 (12.5  $\mu$ M) was observed for compound **L15**.

Various approved drugs show a similar antibiotic activity against *S. aureus* USA300 Lac (JE2)<sup>127</sup>, demonstrating the high potency of **L15** to treat MRSA. Interestingly, **L15**'s inability to prevent the growth of other Gram-positive bacteria (MIC > 50 – 100  $\mu$ M) suggests either

limited uptake or a more strain-specific MoA. For the subsequent studies, **L15** was chosen as the lead compound for two reasons: (1) **L15** showed excellent activity against both *S. aureus* USA300 and *E. coli* 536 and a narrow activity spectrum. (2) **H03** was excluded from further studies, despite its overall high activity, due to its similar structure to a known FtsZ-targeting antibiotic<sup>98</sup>.

## 1.2. Antimicrobial Activity of L15's Chemical Derivatives

To better understand the structural motifs of **L15** and their importance in driving antibiotic activity, structure-activity relationship (SAR) studies with 18 chemical derivatives (**D01** – **D18**) of **L15** were conducted (Figure 9). Derivatives were systematically synthesized by *Franziska A. V. Elsen* and tested for their antibiotic activity in *S. aureus* and *E. coli*. The compound was divided into three parts, consisting of the phenyl ring (I), the 5-membered heterocycle (II), and the functional alkyl guanidinium moiety (III). Different substitution patterns were then designed to identify key structural motives for **L15**'s antibiotic activity and to further improve its potency.

		MIC [ $\mu$ M]		MIC [ $\mu$ M]			
		<i>S. aureus</i>	<i>E. coli</i>	<i>S. aureus</i>	<i>E. coli</i>		
		1.56	12.5	1.56	12.5		
D01		1.56	12.5	D10		0.78	25.0
D02		3.13	25.0	D11		6.25	100
D03		6.25	50.0	D12		6.25	50.0
D04		6.25	50.0	D13		50.0	> 100
D05		0.78	50.0	D14		100	100
D06		1.56	50.0	D15		> 100	> 100
D07		1.56	50.0	D16		25.0	50.0
D08		50	> 100	D17		1.56	25.0
D09		> 100	> 100	D18		1.56	25.0

**Figure 9:** Chemical derivatives of **L15** (**D01** – **D18**) and their respective antibacterial activity in *S. aureus* USA300 Lac (JE2) and *E. coli* 536. On top, the structure of **L15** is shown. Structural parts of the compound are color-coded. The data represent average values of  $n = 3$  biologically independent experiments per compound. This figure was adapted from a previous study<sup>66</sup>.

The position of the bromo substituent at the phenyl ring (**D01** and **D02**) had no or only minor effect on the antibiotic activity. Replacing bromine with fluorine (**D03**) or omitting the alkyl substitution at the phenyl ring completely (**D04**) resulted in a slight reduction of MIC (6.25  $\mu\text{M}$  in *S. aureus* and 50  $\mu\text{M}$  in *E. coli*). By substituting bromine with different alkyl substituents, including isopropyl (**D05**), trifluoromethyl (**D06**), and *tert*-butyl (**D07**), the antibiotic activity against *S. aureus* was either retained (1.56  $\mu\text{M}$ ) or enhanced (0.78  $\mu\text{M}$ ), indicating that this position tolerates substitutions by functional groups. Changing the bromine to a methylsulfonyl substituent (**D08**) reduced the antibiotic activity (50.0  $\mu\text{M}$  – > 100  $\mu\text{M}$ ).

Next, the role of the 5-membered heterocycle was analyzed in more detail. Interestingly, significantly lower antibiotic activity was observed (> 100  $\mu\text{M}$ ) by omitting the phenyl ring (**D09**), indicating that this moiety may be crucial for compound uptake and target engagement, respectively. The highest antibiotic activity against *S. aureus*, with a MIC of 0.78  $\mu\text{M}$ , was observed when replacing the furan with a thiophene ring (**D10**). However, this resulted in a slight activity drop against *E. coli* (25.0  $\mu\text{M}$ ). Attempts to change the furan ring to thiazole (**D11**) or pyrazole (**D12**) led to a drop in the activity against *S. aureus* (6.25  $\mu\text{M}$ ) and with a more pronounced effect in *E. coli* (> 50  $\mu\text{M}$ ). The molecular rigidity was enhanced<sup>128,129</sup> by introducing a neighboring pyridine substituent (**D13**), reducing the antibiotic activity against *S. aureus* (50  $\mu\text{M}$ ) and *E. coli* (> 100  $\mu\text{M}$ ).

In the next step, the role of the functional alkyl guanidinium moiety was investigated. According to the eNTRY rules, primary amines show a higher rate of cellular uptake in Gram-negative bacteria<sup>74</sup>. Interestingly, the respective primary amine (**D14**) derivative significantly reduced the antibiotic activity against both *S. aureus* and *E. coli* (100  $\mu\text{M}$ ), indicating the importance of **L15**'s guanidinium group for cellular uptake and its MoA. Conversely, susceptibility testing of **D14** in membrane-deficient *E. coli*  $\Delta\text{BamB}$  strain did not increase its antibiotic activity (100  $\mu\text{M}$  against *E. coli* BW25113  $\Delta\text{BamB}$  and wild-type *E. coli* BW25113), indicating that the compound's intrinsic features do not impair the cellular uptake of **D14**. Attempts to reduce the basicity<sup>129,130</sup> by replacing the guanidinium group with an acyl guanidine (**D15**) led to the same reduction in antibiotic activity against *S. aureus* and *E. coli* as was already observed for **D09** (> 100  $\mu\text{M}$ ). Introducing a 2-aminoimidazole (**D16**) led to a drop in the MIC (25.0  $\mu\text{M}$  in *S. aureus* and 50.0  $\mu\text{M}$  in *E. coli*). An adjacent methyl (**D17**) or methylene (**D18**) substituent retained antibiotic activity against *S. aureus* (1.56  $\mu\text{M}$ ) or slightly reduced it against *E. coli* (25.0  $\mu\text{M}$ ).

In summary, by dissecting **L15**'s scaffold, insights into key structural elements driving antibiotic activity were obtained. The electronic properties of the phenyl ring (**D01** – **D04**) and its substitutions (**D05** – **D08** and **D13**) influence the antibiotic activity of **L15**. Furthermore, the guanidinium group and phenyl ring are important for **L15**'s antibiotic activity, as its primary

amine (**D14**) and aminoimidazole (**D16**) derivatives as well as removing the phenyl ring (**D09**) significantly reduce their antibiotic activity. Substitutions of the furan ring (**D10 – D12**) are better tolerated, with the thiophene (**D10**) derivative showing the highest observed antibiotic activity in *S. aureus*. The introduction of additional methyl or methylene groups (**D17** and **D18**) does not affect the antibiotic activity in *S. aureus*, but an adjacent acyl group (**D15**) significantly reduces it. The data suggest that some structural flexibility is tolerated but also that protein target binding interactions of the guanidinium group might be necessary to evoke the full potential of **L15**.

### 1.3. Bacterial Uptake and Influence of Cell Density on Antimicrobial Activity of L15

**L15**'s uptake into Gram-negative bacteria was investigated in membrane-deficient ( $\Delta$ BamB) and efflux pump-deficient ( $\Delta$ TolC) strains of *E. coli* BW25113. No increase in antibiotic activity was observed in the mutant strains, indicating that target engagement was already sufficient. Interestingly, in the presence of the membrane permeabilizer polymyxin B nonapeptide (PMBN, 1  $\mu$ g/mL)<sup>128</sup>, the antibiotic activity was enhanced by 2- or 4-fold, respectively (Table 2). This result shows that **L15**'s uptake is either slightly still impaired despite the guanidinium group or there is a synergistic effect with polymyxin B, causing the higher activity.

**Table 2:** Biological activity of **L15** in the membrane- and efflux pump-deficient *E. coli* strains ( $\Delta$ BamB and  $\Delta$ TolC) in the presence of 25 mM NaHCO<sub>3</sub>(\*). A possible role of the membrane was analyzed by adding membrane permeabilizer polymyxin B nonapeptide (PMBN). The data represent average values of n = 3 biologically independent experiments per condition. This table was adapted from a previous study<sup>66</sup>.

Bacterial strain	MIC [ $\mu$ M]* <b>L15</b>	
	no PMBN	1 $\mu$ g/mL PMBN
<i>E. coli</i> BW25113	6.25	3.13
<i>E. coli</i> BW25113 $\Delta$ TolC, JW5503	12.5	3.13
<i>E. coli</i> BW25113 $\Delta$ BamB, JW2496	6.25	6.25

During susceptibility testing of **L15**, cell inoculum-dependent differences in activity were observed, indicating that **L15** is prone to the inoculum effect (IE) compared to vancomycin as a control antibiotic (Table 3). The IE describes an increase in the MIC when the bacterial cell inoculum increases<sup>131,132</sup>. However, the changes in **L15**'s antibiotic activity were only minor compared to what is traditionally defined as IE<sup>133</sup>, and might be caused by enzymatic degradation<sup>134</sup> or inhibition<sup>135</sup> of the antibiotic compound, lowering the number of active drug molecules compared to the number of cells<sup>136,137</sup>.

**Table 3:** Inoculum effect<sup>131</sup> of **L15** in *S. aureus* USA300 Lac (JE2). Biological activity (MIC) of **L15** in *S. aureus* USA300 Lac (JE2) evaluated at different initial cell inoculum in the presence of 25 mM NaHCO<sub>3</sub>(\*). The data represent average values of n = 3 biologically independent experiments per condition. The same experiment was performed in n = 1 biological replicate for vancomycin as a positive control antibiotic. CFU/mL was calculated from cell dilutions that were used as cell inoculum (OD<sub>600</sub> = 5.0 of o/n culture) of n = 1 biological replicate. Here, the MacFarland dilution equals roughly the 1:10000 dilution.

<i>S. aureus</i> USA300 Lac (JE2) dilution (initial cell inoculum)	MIC [ $\mu$ M]* <b>L15</b>	MIC [ $\mu$ M]* <b>Vancomycin</b>	CFU/mL (of initial cell inoculum)
MacFarland	1.56	1.56	-
1:10000	1.56	1.56	-
1:1000	1.56	1.56	1050000
1:100	3.13	1.56	11500000
1:10	12.5	3.13	90000000
1:1	50.0	12.5	300000000
Undiluted	>100	n.a.	1450000000

As most bacterial infections have a cell burden higher than  $5 \times 10^5$  CFU/mL, the clinical significance of the IE needs to be precisely evaluated and considered for the antibiotic's dosage<sup>131</sup>. However, the IE may play a minor role in academic studies, but the concentration of **L15** for subsequent experiments should be adjusted accordingly.

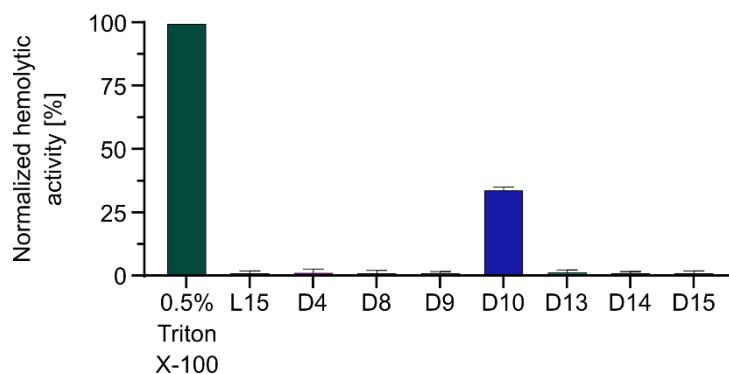
#### 1.4. Cytotoxic and Hemolytic Activity of L15 and Derivatives

Cellular toxicity against human HeLa cells was tested for **L15** and its chemical derivatives (**D01** – **D18**) by a proliferation assay (MTT assay). The half-maximal inhibitory concentration (IC<sub>50</sub>) values ranged from 1.2 to > 100  $\mu$ M for all compounds with antibacterial activity, indicating general toxicity and a correlation with their antibacterial activity (Figure 9). Vice versa, compounds showing a low antibacterial activity (**D08**, **D09**, **D13**, and **D15**) in susceptibility assays showed a decreased human toxicity (IC<sub>50</sub> values > 50  $\mu$ M), except for the primary amine (**D14**) derivative (IC<sub>50</sub> of 9.6 – 14.9 despite high observed MIC of 100  $\mu$ M) (Table 4).

**Table 4:** Biological activity of **L15**, **H03**, **J08**, and **L09**, and synthesized derivatives (**D01 – D18**) in HeLa cells. The data represent values of 95% confidence interval of  $n = 3$  biologically independent experiments per compound. This table was adapted from a previous study<sup>66</sup>.

Compound	IC <sub>50</sub> [μM]
<b>L15</b>	4.0 – 5.7
<b>H03</b>	1.6 – 1.8
<b>J08</b>	3.0 – 3.6
<b>L09</b>	2.2 – 6.1
<b>D01</b>	2.9 – 5.6
<b>D02</b>	2.0 – 3.4
<b>D03</b>	4.7 – 11.5
<b>D04</b>	5.6 – 22.5
<b>D05</b>	2.3 – 3.3
<b>D06</b>	1.6 – 2.2
<b>D07</b>	2.0 – 6.3
<b>D08</b>	> 100
<b>D09</b>	> 100
<b>D10</b>	0.8 – 1.7
<b>D11</b>	7.1 – 14.5
<b>D12</b>	8.8 – 25.7
<b>D13</b>	> 100
<b>D14</b>	9.6 – 14.9
<b>D15</b>	> 50
<b>D16</b>	6.3 – 9.1
<b>D17</b>	3.0 – 5.6
<b>D18</b>	1.6 – 2.2

To exclude membrane-targeting properties of the guanidinium group, the hemolytic activity of **L15** and some derivatives (**D04**, **D08**, **D09**, **D10**, **D13**, **D14**, and **D15**) was assessed in sheep blood solution. Derivatives were selected to cover a broad range of antibacterial activity. Among them, only the thiophene (**D10**) derivative showed hemolytic activity (35% hemolysis at 100 μM) (Figure 10), indicating that the observed human cytotoxicity is most likely not caused by membrane disruption.

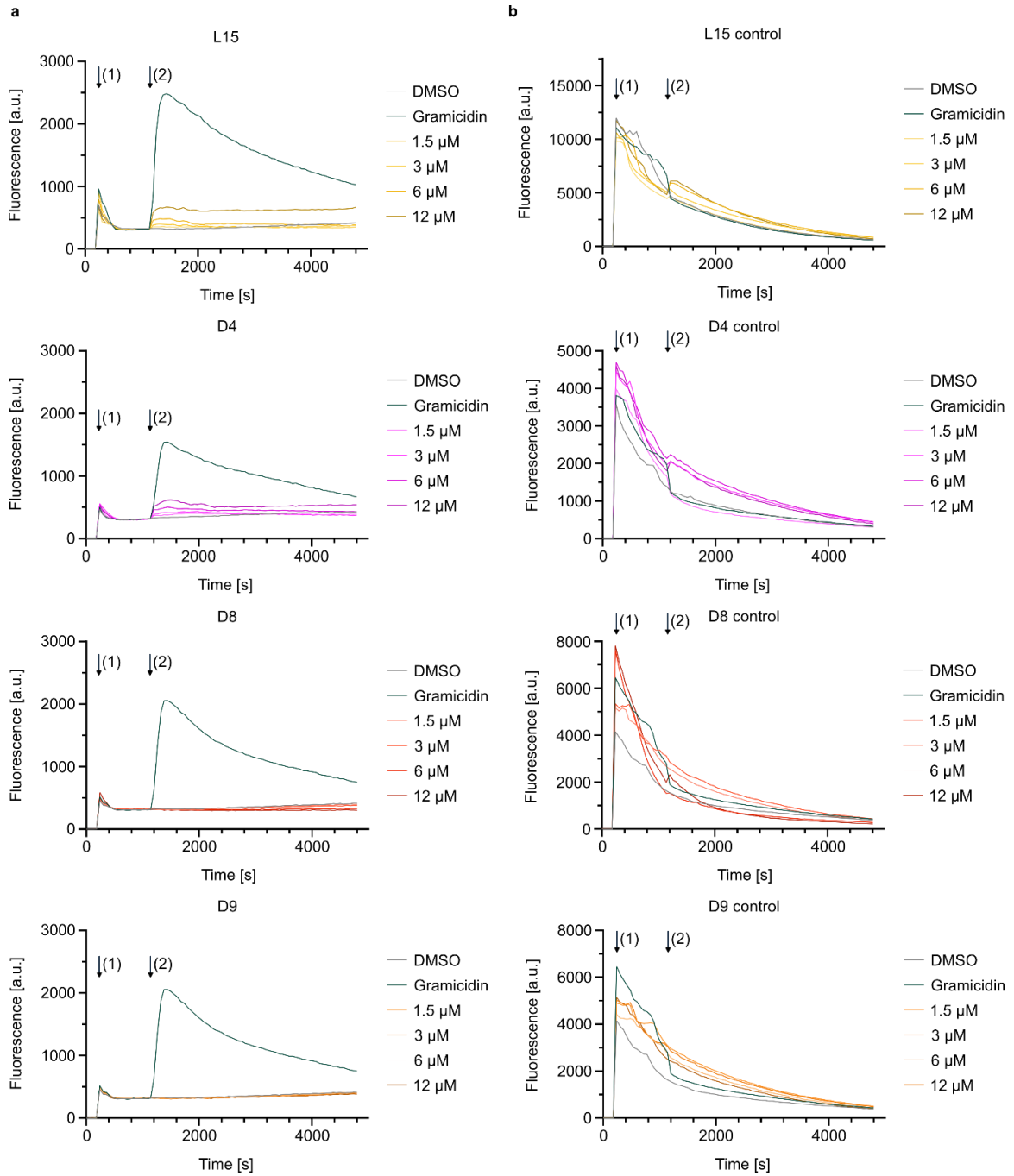


**Figure 10:** Hemolytic activity of **L15** and some chemical derivatives in sheep blood solution. The fluorescence was measured at OD<sub>540nm</sub> and normalized to 0.5% Triton X-100 as a positive control. The data represent mean values  $\pm$  s.d. of averaged triplicates of  $n = 3$  biologically independent experiments per compound. This figure was adapted from a previous study<sup>66</sup>.

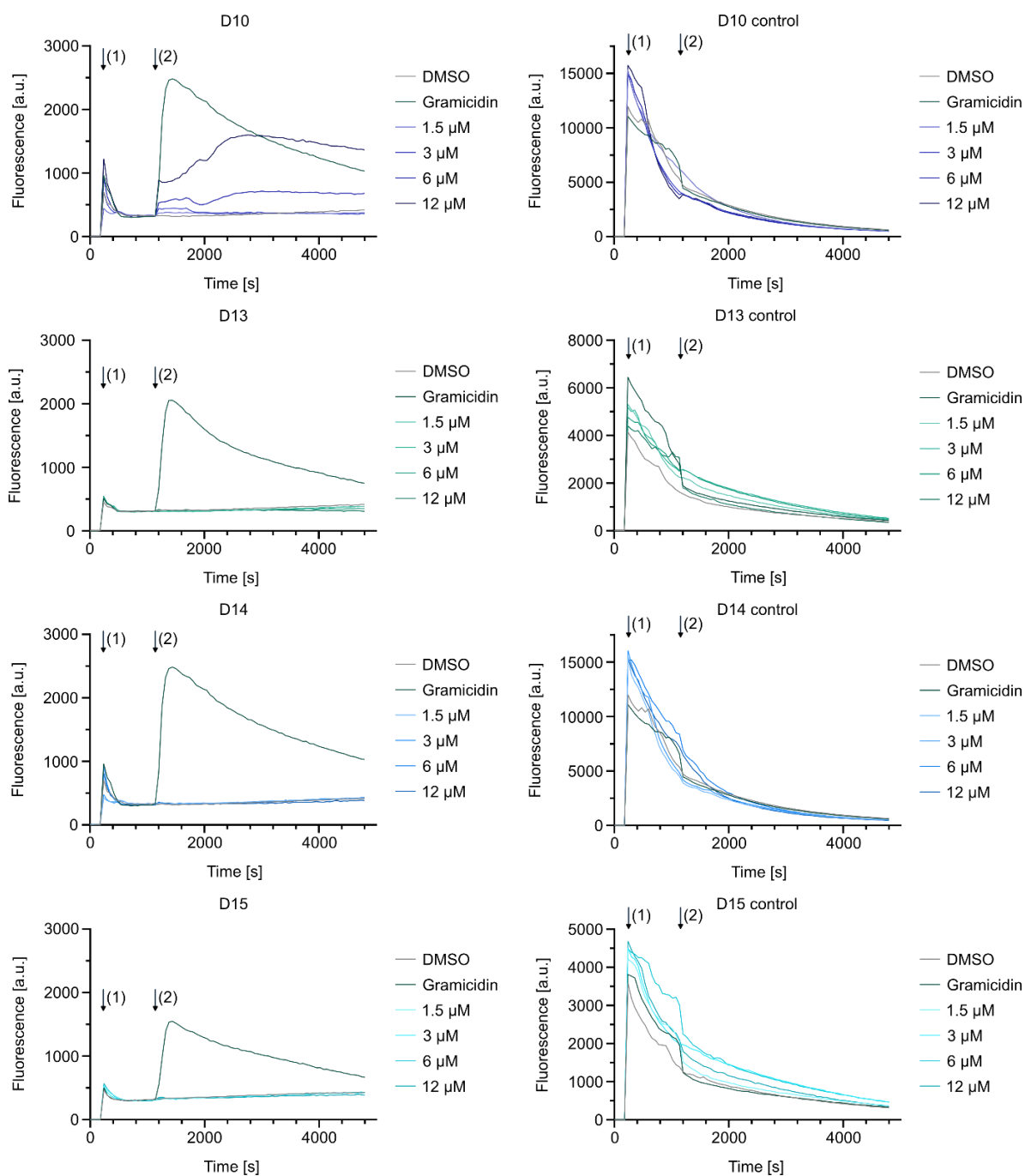
By comparing the obtained biological activity data (susceptibility, proliferation, and hemolysis assays), **L15** showed the best activity profile among the tested compounds and was thus selected for subsequent studies. These were conducted in *S. aureus* due to **L15**'s higher potency compared to its antibacterial activity against *E. coli*.

### 1.5. Membrane-Targeting Properties of L15 and Derivatives

Although the initial hemolysis data showed only a weak effect of the thiophene (**D10**) derivative to act on the membrane, the ability of **L15** and some derivatives (**D04**, **D08**, **D09**, **D10**, **D13**, **D14**, and **D15**) to affect the bacterial membrane was analyzed by a membrane depolarization assay<sup>138</sup>. For this, the fluorescence of membrane potential-sensitive dye 3,3'-dipropylthiadicarbocyanine iodide (DiSC<sub>3</sub>(5)) was recorded upon compound treatment and compared to gramicidin (1  $\mu$ M) as a positive control. Membrane depolarization was only observed for **L15**, **D04**, and **D10** at higher concentrations (6  $\mu$ M and 12  $\mu$ M, Figure 11), corroborating that the higher inoculum size in the membrane depolarization assay (OD<sub>600</sub> = 0.3) might increase the MIC and thus no effects on the bacterial membrane were observed at lower concentrations (1.5  $\mu$ M and 3  $\mu$ M).







**Figure 11:** Membrane depolarization of **L15** and derivatives in *S. aureus* USA300 Lac (JE2) cells. (a) The fluorescence of membrane potential-sensitive dye DiSC<sub>3</sub>(5) was recorded at  $\lambda_{\text{ex}} = 610$  nm and  $\lambda_{\text{em}} = 660$  nm. The black arrows indicate the addition of DiSC<sub>3</sub>(5) (1) and compound (2), respectively. As a positive control, 1  $\mu\text{M}$  gramicidin was used. (b) Fluorescence of DiSC<sub>3</sub>(5) in the absence of cells, but otherwise, in the same conditions as in (a). The data are representative for  $n = 3$  biologically independent experiments per condition. This figure was adapted from a previous study<sup>66</sup>.

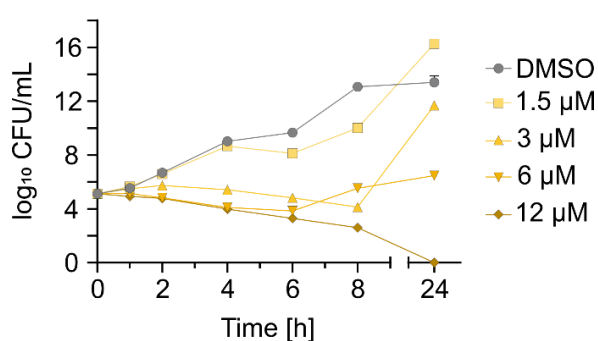
Compared to the membrane depolarization of gramicidin, the observed effects for **L15** and **D04** are negligible. The highest impact on membrane depolarization was observed for **D10**, correlating with its highest antibacterial activity among all tested derivatives. In contrast, the derivatives with a low antibiotic activity (**D08**, **D09**, **D13**, and **D15**) in susceptibility and

proliferation assays did not affect the bacterial membrane at all. Interestingly, the primary amine (**D14**) derivative did not show any change in fluorescence, although its' observed cellular toxicity in HeLa cells. This result corroborates the finding that the observed human toxicity is not caused by an unspecific membrane-targeting effect.

According to the obtained results, the functional guanidinium group by itself is not causing toxicity by targeting the membrane, as no membrane depolarization was observed for some **L15** derivatives (**D08**, **D09**, **D13**, and **D15**). By comparing the gathered biological activity data (susceptibility, proliferation, and hemolysis assays), the substituent patterns at the phenyl ring towards higher polar moieties seem to affect the membrane less, as well as the presence of a primary amine group (**D14**). In the case of **D15**, a possible intermolecular interaction of the guanidinium group with cell membrane components might be impaired because of the acyl group. However, these hypotheses are highly speculative and are not proven so far.

### 1.6. Kinetics of L15's Action, Resistance Development of L15-Treated *S. aureus* and Genomic Sequencing of L15-Resistant Mutants

Time-kill studies were initially performed to assess the mechanism and kinetics of **L15**'s action on *S. aureus* growth (Figure 12), revealing a bactericidal effect towards the highest tested concentration (12  $\mu\text{M}$ ). For time-kill experiments, the cell inoculum was approx. 10-fold greater than the Clinical and Laboratory Standards Institute (CLSI)-recommended inoculum size of  $5 \times 10^5$  CFU/mL (MacFarland dilution) for MIC susceptibility testing<sup>139</sup>. The expected **L15** concentration to inhibit growth should still be 1.56  $\mu\text{M}$  (Figure 9). However, a reduced growth was only seen for 3  $\mu\text{M}$  and higher **L15** concentrations.



**Figure 12:** Time-kill curves of *S. aureus* USA300 Lac (JE2) cells treated with different **L15** concentrations. The data represents  $n = 2$  biologically independent experiments per concentration. This figure was adapted from a previous study<sup>66</sup>.

According to the obtained results, **L15** shows a dual mechanism: bacteriostatic effects at low concentrations (3  $\mu\text{M}$  and 6  $\mu\text{M}$ ) and a transition to its bactericidal cell killing at high concentrations (12  $\mu\text{M}$ ). This phenomenon has already been observed for other antibiotics<sup>140</sup>. The bactericidal mechanism could be further confirmed by assessing the minimum bactericidal

concentration (MBC), referred to as the lowest compound concentration that reduces more than 99.9% of the initial cell inoculum (3-log<sub>10</sub> reduction). **L15**'s MBC value was calculated to be 3.13 μM, with an MBC to MIC ratio of 2, indicating a bactericidal mechanism (MBC/MIC ratios of ≤ 4)<sup>98,141</sup>. Interestingly, cell growth was rescued after 24 h when treated with 3 μM and 6 μM **L15**, suggesting that a small cell population endured **L15** stress and developed a resistance mechanism.

A possible resistance development was assessed by frequency of resistance (FoR) experiments, and a FoR value in the range of 2.3x10<sup>-8</sup> – 2.8x10<sup>-8</sup> at 6 μM **L15** was obtained, displaying low resistance development<sup>142</sup> (Table 5).

**Table 5:** CFUs growing on **L15**-containing agar plates to determine the frequency of resistance. FoR values were calculated by dividing the number of resistant colonies that grew on **L15**-containing plates by the total number of the initial cell inoculum. The data are representative of n = 2 biologically independent experiments. This table was adapted from a previous study<sup>66</sup>.

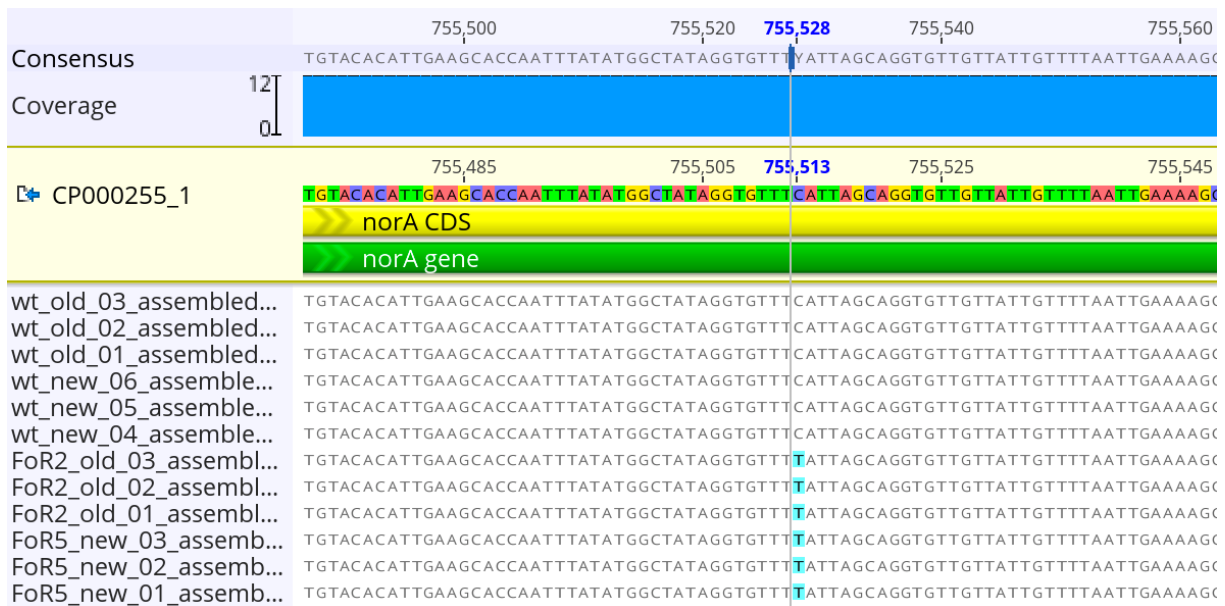
CFU/mL of test inoculum	Colonies on 6 μM <b>L15</b> -containing plate	Frequency of resistance (FoR)
0.64x10 <sup>9</sup> CFU/mL	18	2.8x10 <sup>-8</sup>
0.62x10 <sup>9</sup> CFU/mL	14	2.3x10 <sup>-8</sup>

Colonies that grew on agar plates containing 6 μM **L15** (**L15**-resistant mutants) showed increased MIC values (Table 6), confirming a reduced susceptibility towards **L15**.

**Table 6:** Biological activity of **L15** in *S. aureus* USA300 Lac (JE2) mutants generated by FoR assay in the presence of 25 mM NaHCO<sub>3</sub>(\*). The data represent average values of n = 3 biologically independent experiments per mutant. This table was adapted from a previous study<sup>66</sup>.

<i>S. aureus</i> USA300 Lac (JE2) FoR mutants	MIC [μM]* <b>L15</b>
Mutant_1	12.5
Mutant_2	12.5
Mutant_3	12.5

To assess if the mechanism of resistance is linked to a putative target of **L15**, performed genomic sequencing of the generated mutants was performed by *Howard Junca*. Interestingly, one single conversed mutation was found that was restricted to the mutant strains only. The mutation appeared as a single nucleotide polymorphism (SNP) in position 75513 (reference genome CP000255) in the multidrug efflux pump NorA<sup>143,144</sup> (UniProt ID: A0A0H2XGK0), changing C to T and thereby leading to a change in amino acid from S to L in position 366 (Figure 13).



**Figure 13:** Visualization of the observed SNP in the *norA* gene. L15-resistant mutants of *S. aureus* USA300 Lac (JE2) (labeled FoR2 or FoR5, *old* and *new*) were obtained from FoR assays and compared to wild-types (labeled wt *old* and *new*). The affected base shows a change from C to T at position 755513. The data show results from  $n = 3$  biologically independent replicates from two independent experiments. The mutated nucleotide is highlighted in cyan. Visualization was done with Minimap2<sup>145</sup>. This figure was adapted from a previous study<sup>66</sup>.

The role of efflux pumps as an intrinsic resistance mechanism is a common obstacle that complicates antibiotic treatment in general<sup>146</sup>. NorA belongs to the Major Facilitator Superfamily of multidrug efflux pumps, which is dependent on the PMF and harnesses the transport of protons for efflux shuffle<sup>147</sup>. It is crucial in causing low-level resistance towards hydrophilic fluoroquinolone antibiotics and other substrates such as biocides, dyes, and quaternary ammonium compounds<sup>148</sup>. Interestingly, the affected amino acid position 366 is completely conserved in all *S. aureus* genomes reported so far, addressing this position to study NorA's efflux mechanism and to develop future NorA inhibitors. Susceptibility of the L15-resistant mutants towards the fluoroquinolones **ciprofloxacin** and **norfloxacin** was not significantly altered (2-fold decrease in MIC), indicating a negligible effect on fluoroquinolone resistance (Table 7). The higher activity of the fluoroquinolones in L15-resistant mutants might be explained by a structural change in NorA, decreasing the efflux of these antibiotics.

**Table 7:** Biological activity of **L15**, and the fluoroquinolones **ciprofloxacin** and **norfloxacin** in *S. aureus* USA300 Lac (JE2), **L15**-resistant mutants (FoR mutants), and *S. aureus* USA300 Lac (JE2)  $\Delta norA$  transposon mutant ( $\Delta norA$  transposon mutant from Nebraska transposon mutant library<sup>149</sup>), with and without 25 mM NaHCO<sub>3</sub>(\*). The data represent average values of n = 3 biologically independent experiments per condition. This table was adapted from a previous study<sup>66</sup>.

Bacterial strain	MIC [ $\mu$ M]* <b>L15</b>				MIC [ $\mu$ M]* <b>Ciprofloxacin</b>		MIC [ $\mu$ M]* <b>Norfloxacin</b>	
	25 mM NaHCO <sub>3</sub>		No NaHCO <sub>3</sub>		25 mM NaHCO <sub>3</sub>	No NaHCO <sub>3</sub>	25 mM NaHCO <sub>3</sub>	No NaHCO <sub>3</sub>
	No reserpine	20 $\mu$ g/mL reserpine	No reserpine	20 $\mu$ g/mL reserpine	-	-	-	-
<i>S. aureus</i> USA300 Lac (JE2)	1.56	1.56	12.5	3.13	50.0	25.0	> 100	100
FoR mutant	6.25	6.25	25.0	12.5	25.0	12.5	100	25.0
$\Delta norA$ transposon mutant	0.78	0.78	12.5	3.13	50.0	25.0	100	50.0

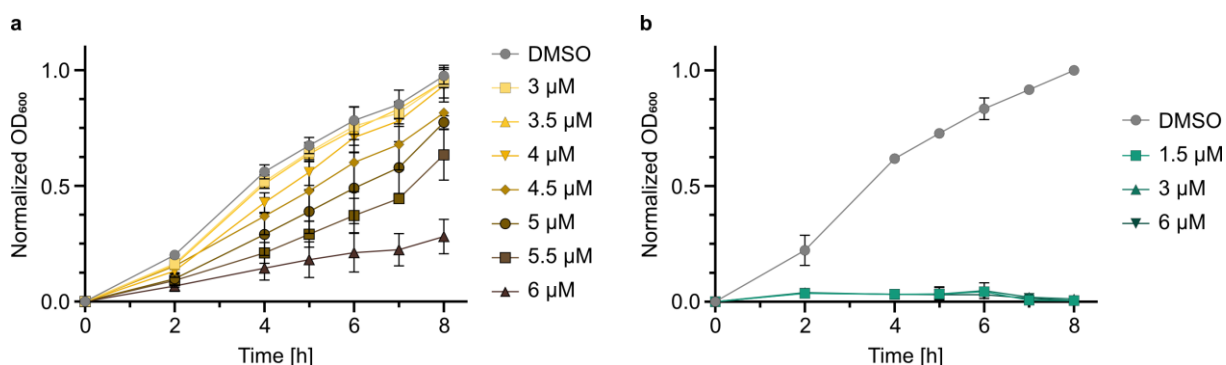
*S. aureus* lacking NorA (*S. aureus* USA300 Lac (JE2)  $\Delta norA$ <sup>149</sup>) enhanced **L15**'s activity (2-fold decrease in MIC), demonstrating the relevance of NorA for reducing the concentration of **L15** by selective efflux and explaining the reduced susceptibility of the **L15**-resistant mutants. By adding the efflux pump inhibitor reserpine<sup>150</sup> (33  $\mu$ M), the activity of **L15** against the tested strains was higher (2-fold and 4-fold) in the absence of NaHCO<sub>3</sub>, suggesting that **L15** is prone to efflux and a target substrate of NorA. In a previous study, NaHCO<sub>3</sub> was shown to act on the PMF by dissipating the pH gradient<sup>68</sup>. This change in pH could reduce the efflux activity of NorA, but in the presence of reserpine, the effect of NaHCO<sub>3</sub> vanishes and no change in **L15**'s activity is observed anymore. The PMF could also be involved in fluoroquinolone activity and might explain the lower susceptibility towards **ciprofloxacin** and **norfloxacin** in the presence of NaHCO<sub>3</sub>.

However, the mechanism of resistance is not directly linked to **L15**'s mechanism of action. Besides the conserved mutation in the *norA* gene, no additional consistent gene mutations were obtained during sequencing.

### 1.7. Growth of *S. aureus* under L15 Stress and Global Proteome Changes

To further elucidate the mechanism of action of **L15**, global proteome changes in the presence of **L15** were investigated. Before starting with these experiments, the optimal **L15** concentration needed to be assessed. Interestingly, *S. aureus* growth showed an **L15** concentration-dependent behavior and corroborated the previously detected IE, explaining

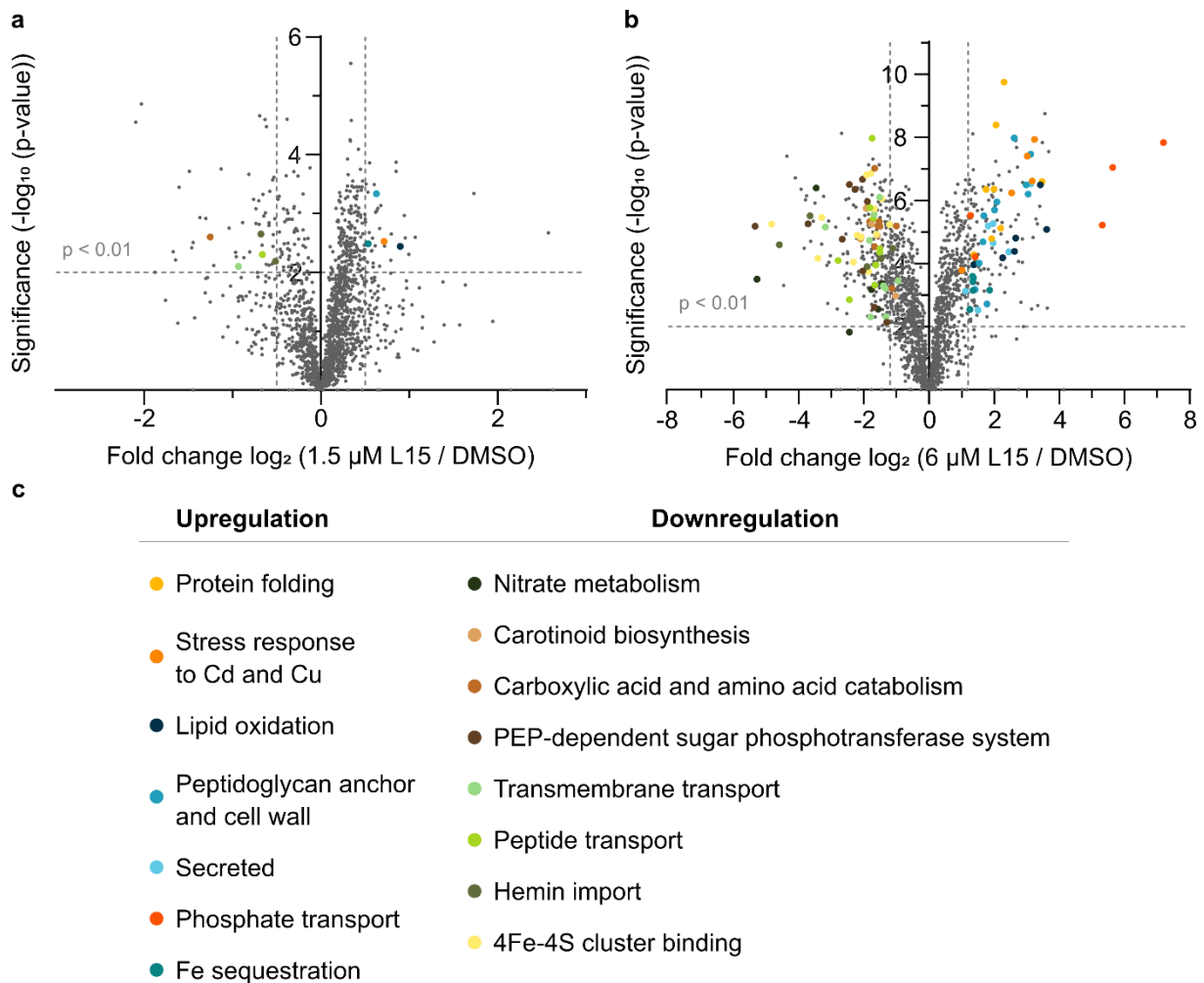
why cell growth is only impaired at higher MIC (Figure 14a) compared to what was observed in standard susceptibility assays (Figure 9). In contrast, vancomycin completely abolished growth even at the lowest concentration (1.5  $\mu\text{M}$ ) (Figure 14b).



**Figure 14:** Normalized growth curves of *S. aureus* USA300 Lac (JE2) cells treated with various concentrations of **L15** (a) or **vancomycin** (b) as a positive control. The data represent mean values  $\pm$  s.d. of averaged technical triplicates of  $n = 2$  biologically independent experiments per concentration.

For growth studies, the cell inoculum was approx. 100-fold greater than the CLSI-recommended inoculum size of  $5 \times 10^5$  CFU/mL (MacFarland dilution) for MIC susceptibility testing. According to the MIC calculations conducted with different cell inoculums (Table 3), the expected **L15** concentration to inhibit *S. aureus* growth should be 3.13  $\mu\text{M}$ . As there is no significant change in cell growth at 3  $\mu\text{M}$  **L15**, additional factors need to be considered to explain the observed growth (e.g., inoculum size calculation and culture conditions).

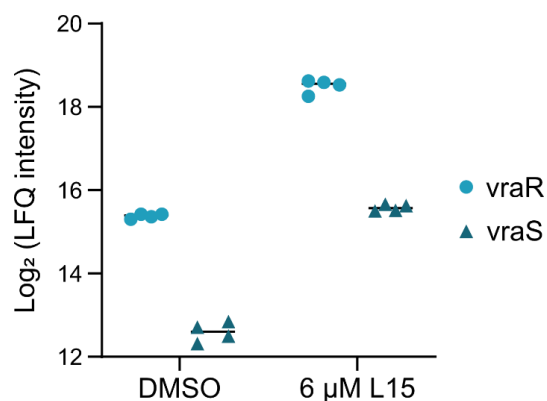
To obtain a global proteomic picture of *S. aureus*' stress response towards **L15**, different compound concentrations (1.5  $\mu\text{M}$ , 3  $\mu\text{M}$ , 4.5  $\mu\text{M}$ , 5  $\mu\text{M}$ , 5.5  $\mu\text{M}$ , and 6  $\mu\text{M}$ ) were applied based on the previous growth studies (Figure 14). The data shows a global stress response with an **L15** concentration-dependent increase of functionally up- and downregulated proteins (Figure 15, Table S2).



**Figure 15:** Full proteome analysis of *S. aureus* USA300 Lac (JE2). Scatter plots of *S. aureus* full proteome treated with 1.5  $\mu$ M (a) and 6  $\mu$ M (b) L15 compared to DMSO. The vertical and horizontal dashed lines represent a  $\log_2$ -fold change ratio of 0.5 (1.5  $\mu$ M L15) or 1.2 (6  $\mu$ M L15) and a  $-\log_{10}$  p-value of 2. Colored dots show functionally enriched proteins that were up- and downregulated. (c) Table of functionally enriched up- and downregulated proteins using STRING<sup>151</sup> analysis. PEP = Phosphoenolpyruvate. This figure was adapted from a previous study<sup>66</sup>.

Upregulated proteins with the highest fold change values were part of the phosphate import, suggesting that *S. aureus* copes with the L15 stress with higher phosphate levels. Also, an increased virulence was observed by upregulation of proteins involved in iron sequestration (staphyloferrin B synthesis) and secreted proteins that act as virulence factors (clfA, clfB, flgJ, flr, isdC, isdH, lytM, sasF, sceD, sdrC, sdrE, ssaA, and sspP) and autolysins (flgJ, lytM, and sceD). This global rewiring in protein expression upon antibiotic stress is accompanied by higher levels of chaperones and proteins involved in cell wall remodeling and lipid oxidation, suggesting an overall impact on the cell membrane at higher L15 concentrations (Figure 15).

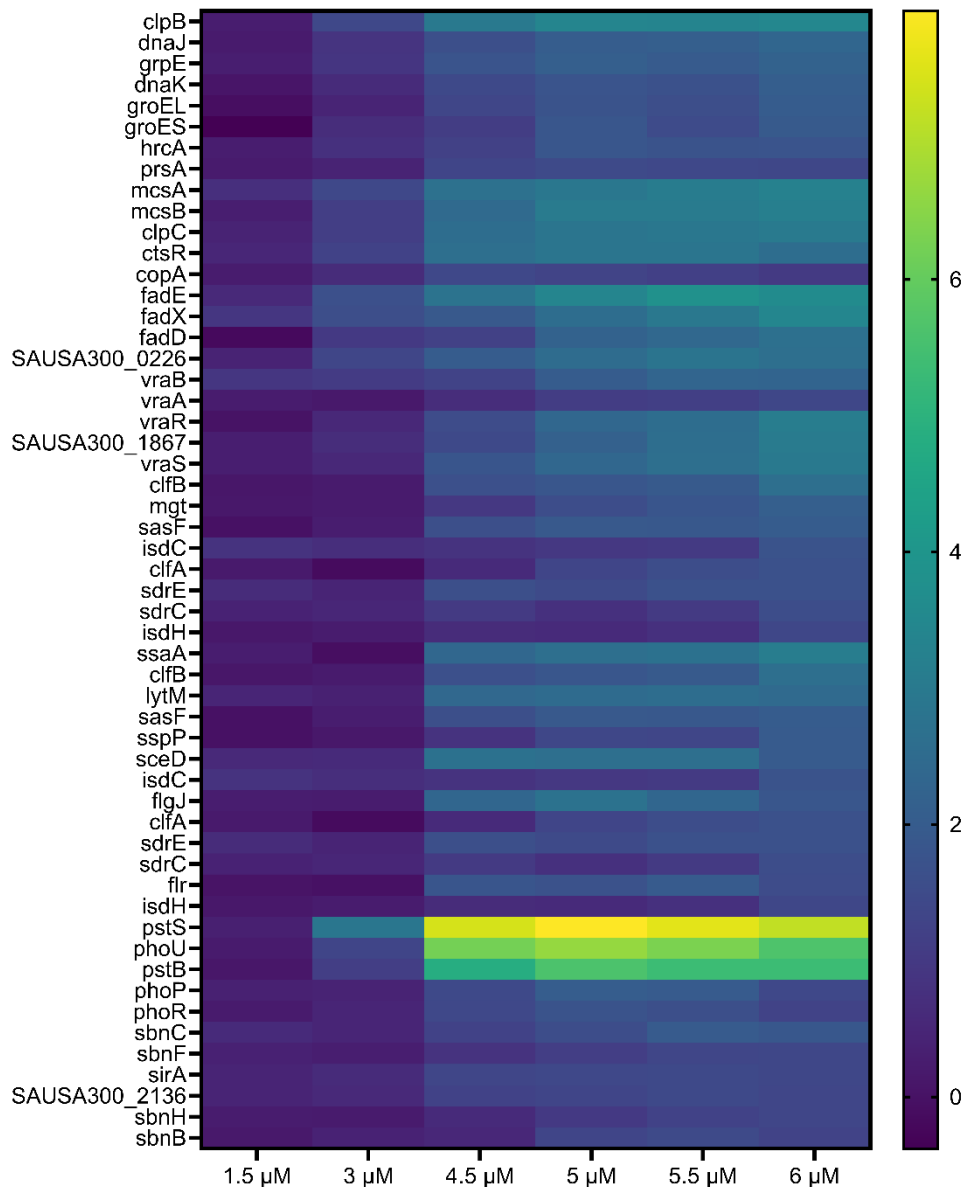
To encounter cell wall stress, *S. aureus* reacts by higher expression of the two-component system VraSR<sup>152–155</sup> (Figure 16).



**Figure 16:** Relative LFQ intensities of *vraR* (UniProt ID: A0A0H2XGC9) and *vraS* (UniProt ID: A0A0H2XJC3) measured by mass spectrometry. *S. aureus* USA300 Lac (JE2) cells were treated with **L15** (6 μM) and compared to DMSO. The data represent n = 4 biologically independent replicates. This figure was adapted from a previous study<sup>66</sup>.

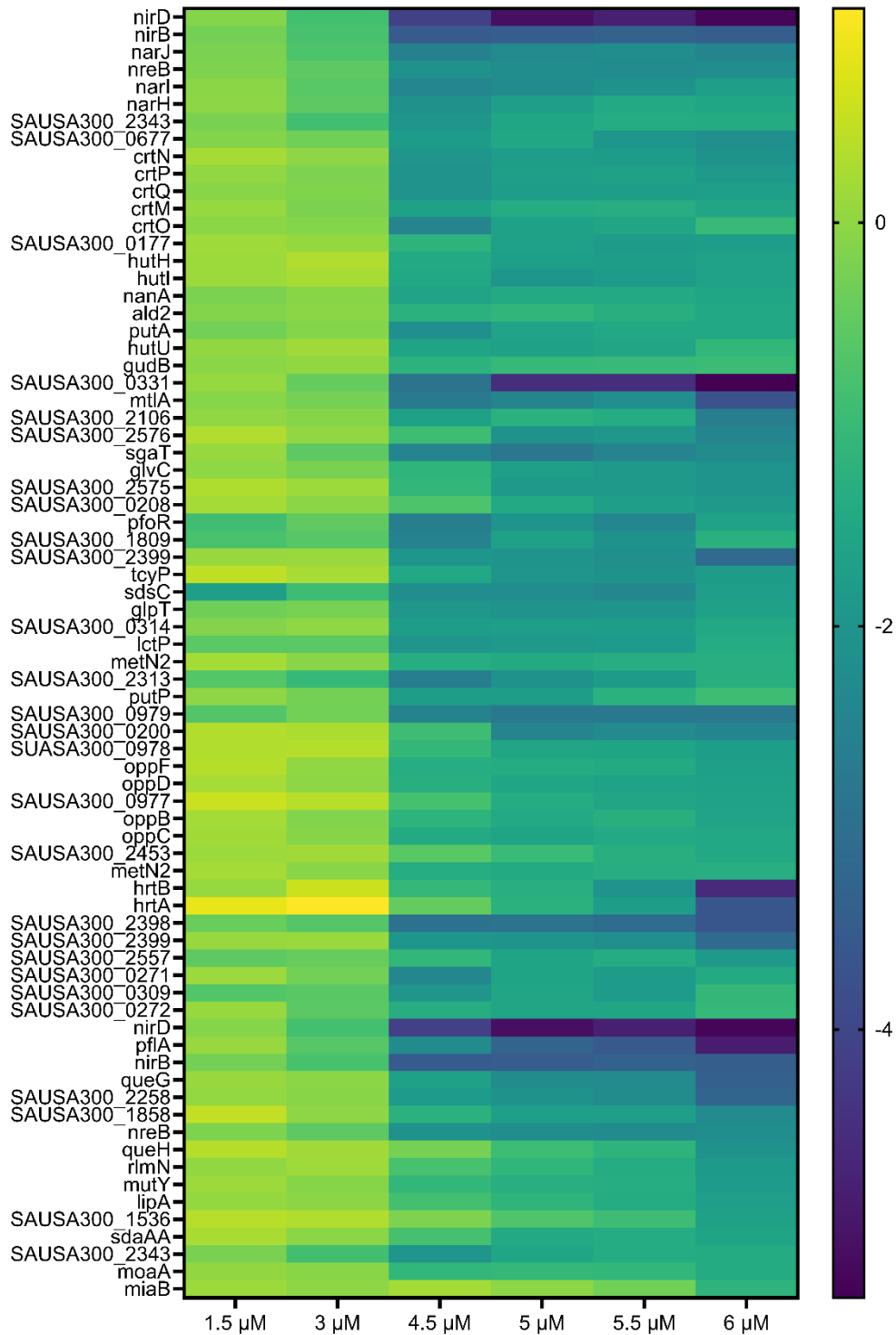
Interestingly, treatment with 1.5 μM and 3 μM **L15** had barely an effect on the proteome level (Figure 17, Figure 18), indicating that higher compound concentrations are needed to exert a stress response. This finding was also reflected in the observed growth behavior, showing that *S. aureus* growth is not impaired at 3 μM **L15** (1.5 μM **L15** not applied) (Figure 14a).





**Figure 17:** Heatmap of upregulated proteins of *S. aureus* USA300 Lac (JE2) in response to L15 treatment at different concentrations. Gene names are shown. The data represent  $n = 4$  biologically independent replicates. The heatmap was created with *GraphPad Prism* 10.01.

In contrast, many proteins involved in different transport systems are downregulated (Table S2), indicating that the cellular transport system is impaired due to cell wall remodeling processes. By downregulating proteins needed to synthesize staphyloxanthin, *S. aureus* can change the chemical composition of the cell membrane and might save precursor substrates for peptidoglycan synthesis<sup>156</sup>. In addition, proteins involved in nitrate metabolism, carboxylic acid catabolism, and iron-sulfur cluster binding were also downregulated.

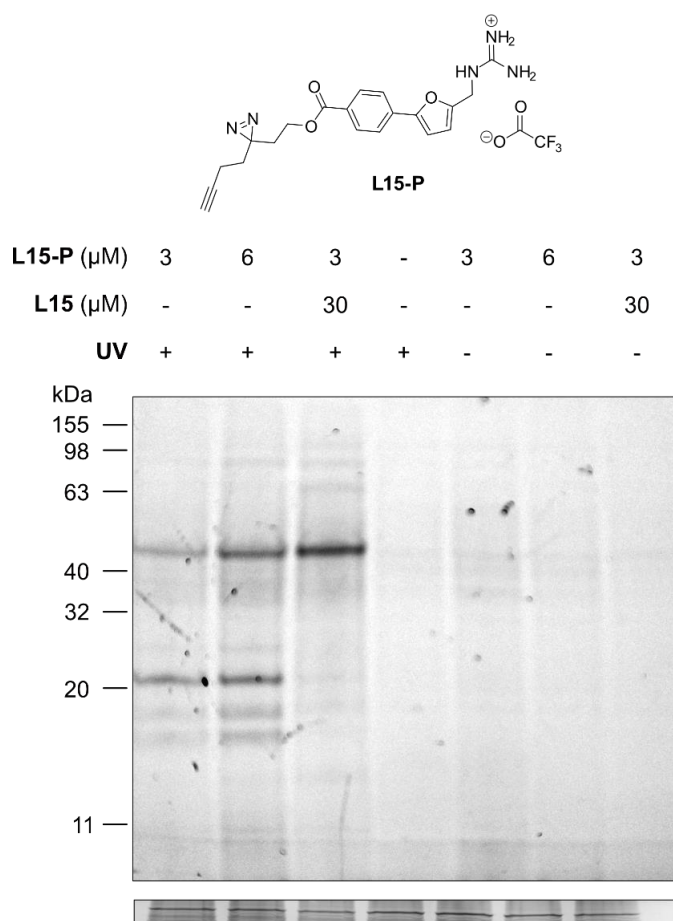


**Figure 18:** Heatmap of downregulated proteins of *S. aureus* USA300 Lac (JE2) in response to L15 treatment at different concentrations. Gene names are shown. The data represent n = 4 biologically independent replicates. The heatmap was created with *GraphPad Prism* 10.01.

Taken together, L15 induces complex proteomic changes in *S. aureus* in order to cope with the evoked antibiotic stress.

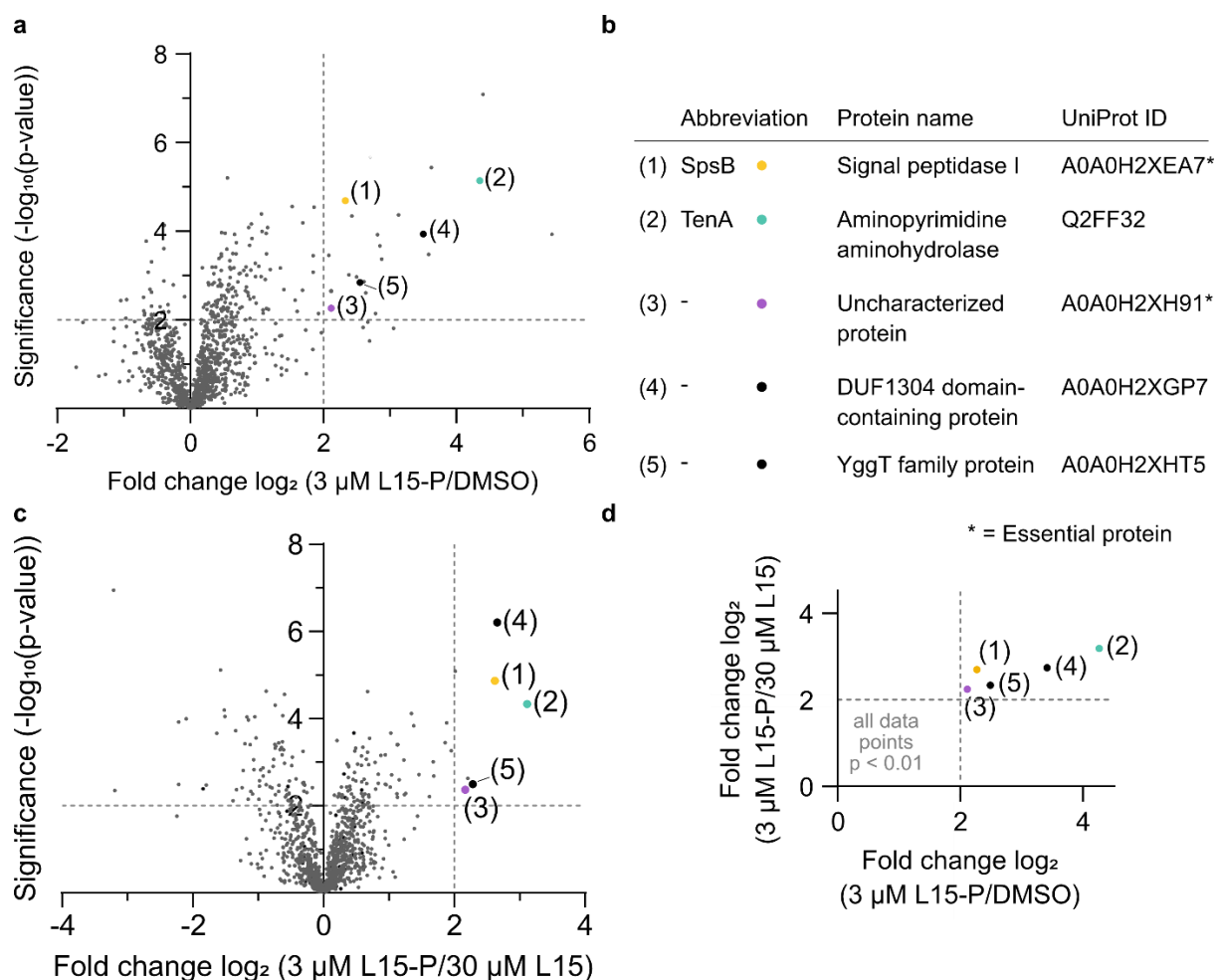
## 1.8. Protein Target Identification by Affinity-Based Protein Profiling

Having a first glimpse of **L15**'s mechanism of action, target identification studies were performed by affinity-based protein profiling. For this, *S. aureus* cells were treated with the photoaffinity probe **L15-P** (Figure 19), equipped with a diazirine moiety for covalent photo-crosslinking to direct protein targets and an alkyne handle for downstream analysis. The minimal photo-crosslinker was introduced at the *para* position of the phenyl ring, which showed high tolerability towards functionalization. An initial experiment confirmed a retained activity of **L15-P** in *S. aureus* (MIC = 1.56  $\mu\text{M}$ ). A gel-based labeling was then performed where *S. aureus* cells were treated with **L15-P**, following subsequent UV irradiation, cell lysis, and functionalization with rhodamine azide using click chemistry to visualize target proteins by fluorescent SDS-PAGE (Figure 6). Several proteins could be labeled in a concentration-dependent manner, and further successfully outcompeted by a 10-fold excess of **L15** (Figure 19), displaying possible protein targets. In contrast, one protein band at around 45 kDa showed an increased intensity in the competition experiment for unknown reasons.



**Figure 19:** Chemical structure of the photo-affinity probe **L15-P** and fluorescence SDS-PAGE of *S. aureus* USA300 Lac (JE2) probe-labeled cells. The competition with a ten-fold excess of **L15** (30  $\mu\text{M}$ ) is shown. The data are representative for  $n = 3$  biologically independent experiments per condition. This figure was adapted from a previous study<sup>66</sup>.

Next, quantitative A/BPP studies were performed (Figure 20). The probe-treated cells were initially clicked to biotin azide for subsequent enrichment on streptavidin beads and enzymatic digestion before subjecting them to LC/MS-MS analysis (Figure 6). Proteins that displayed a p-value of  $< 0.01$  and a  $\log_2$ -fold enrichment value of  $> 2$  were classified as a hit (Figure 20a). To reduce the background and unspecific binding, a competitive A/BPP with a 10-fold excess of **L15** was conducted, narrowing the number of potential protein targets down to five (Figure 20b, c, d), two of them being essential for *S. aureus* viability: an uncharacterized protein (Uniprot ID: A0A0H2XH91) and the signal peptidase IB<sup>157</sup> (SpsB, Uniprot ID: A0A0H2XEA7).



**Figure 20:** Target identification experiments of **L15-P** in *S. aureus* USA300 Lac (JE2) by A/BPP. (a) Scatter plot of *S. aureus*-treated cells (3  $\mu\text{M}$  **L15-P**) compared to DMSO. (b) Table of enriched proteins in both A/BPP (a) and competitive A/BPP (c) experiments, including two essential [(1) and (3)] and three non-essential proteins [(2), (4) and (5)]. (c) Scatter plot of *S. aureus*-treated cells in a competitive A/BPP experiment using a ten-fold excess of **L15** (3  $\mu\text{M}$  **L15-P** and 30  $\mu\text{M}$  **L15**) compared to DMSO. (d) Scatter plot including both A/BPP experiments [(a) and (c)] to highlight successfully outcompeted proteins. The vertical and horizontal dashed lines in all scatter plots represent a  $\log_2$ -fold enrichment ratio of 2 and a  $-\log_{10}$  p-value of 2. A two-sample students' t-test, including permutation-based multiple testing correction (false discovery rate (FDR) = 0.05), was performed for all relevant comparisons to calculate the fold-change and statistical relevance. The data represent  $n = 4$  biologically independent replicates. This figure was adapted from a previous study<sup>66</sup>.

Among the non-essential proteins, an aminopyrimidine aminohydrolase (Uniprot ID: Q2FF32) was highly enriched in both experiments, considering it to be involved in **L15**'s mechanism of action. However, a following susceptibility assay of the corresponding TenA transposon mutant (*S. aureus* USA300 Lac (JE2)  $\Delta tenA^{149}$ ) did not prove to be affected by **L15**, showing no significant shift in MIC (Table 8).

**Table 8:** Biological activity of **L15** in *S. aureus* USA300 Lac (JE2) and *S. aureus* USA300 Lac (JE2)  $\Delta tenA$  transposon mutant ( $\Delta tenA$  transposon mutant from Nebraska transposon mutant library<sup>149</sup>) in presence of 25 mM NaHCO<sub>3</sub>(\*). The data represent average values of n = 3 biologically independent experiments per group.

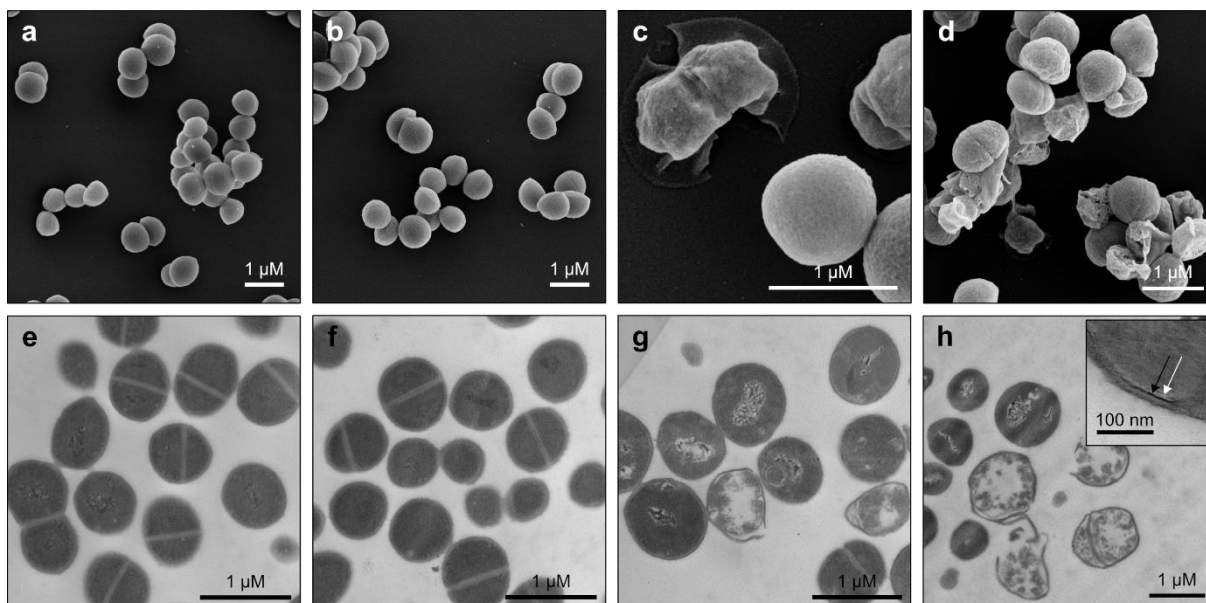
Bacterial strain	MIC [ $\mu$ M]* <b>L15</b>
<i>S. aureus</i> USA300 Lac (JE2)	1.56
$\Delta tenA$ transposon mutant	1.56

Lacking any functional assignment of the essential uncharacterized protein, SpsB target validation was prioritized. This enzyme displays a crucial role in protein secretion by cleaving signal peptides of its substrates. In previous studies, inhibition and activation of SpsB demonstrated a lethal effect on *S. aureus* cells<sup>42,158–160</sup>. While enzyme inhibition is a more common mechanism, activation is less studied. In the case of SpsB, the first detected activator molecule **PK150** enhances enzyme turnover up to 3-fold, measured in an *in vitro* Förster resonance energy transfer (FRET) assay. As a consequence, autolysins are released in an uncontrolled manner, leading to cell lysis and subsequent killing<sup>42</sup>.

Considering SpsB to be involved in **L15**'s mechanism of action, the upregulation of secreted SpsB substrate proteins (proteins with the functional enrichment term 'Secreted') and the proteins involved in cell wall remodeling observed in the full proteome studies may be explained (Table S2).

### 1.9. Morphological Changes in L15-Treated *S. aureus* by Electron Microscopy

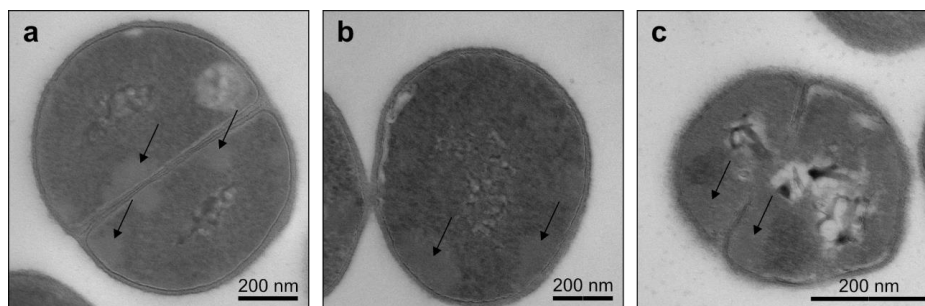
Before starting with SpsB validation studies, morphological changes of **L15**-treated *S. aureus* cells were analyzed using electron microscopy (EM). EM studies were performed by *Mathias Müssen*. To assess appropriate **L15** concentrations, where morphological changes could be visualized, MIC values of different inoculum sizes were used. The MIC at OD<sub>600</sub> = 0.5 (cell density for **L15** treatment in EM studies) was determined to be 12.5  $\mu$ M (Table 3). Based on this, three different concentrations were chosen for EM studies (3  $\mu$ M, 12.5  $\mu$ M, and 48  $\mu$ M) (Figure 21).



**Figure 21:** Scanning electron microscopy [(a) – (d)] and transmission electron microscopy [(e) – (h)] images of *S. aureus* USA300 Lac (JE2) cells treated with DMSO [(a) and (e)] or **L15** [3  $\mu$ M (b) and (f), 12.5  $\mu$ M (c) and (g), and 48  $\mu$ M (d) and (h)]. Healthy cells have a round and smooth coccal shape [(a) and (b)]. Higher **L15** concentrations reveal changes in cell morphology [(c), (d)]. Close-up window (h) shows the intermediate layer (black arrow) and the electron transparent lipid layer (white arrow) of the cell membrane. The data represent  $n = 2$  biologically independent experiments per condition. Scale bars represent 1  $\mu$ m and 100 nm (detail h). This figure was adapted from a previous study<sup>66</sup>.

Treatment at 3  $\mu$ M **L15** did not significantly change cell morphology (Figure 21b, f), but with increasing compound concentrations, more pronounced effects were observed. Deformation of the overall cell shape was already observed at 12.5  $\mu$ M **L15** (Figure 21c, g), while more severe damage in the form of DNA rearrangement (Figure 21g, h) and cell death with the release of cytoplasmic components (Figure 21d, h) was visible at the highest tested **L15** concentration (48  $\mu$ M). In addition, the lipid layer of the cytoplasmic membrane was affected at 48  $\mu$ M (Figure 21h close-up), suggesting that the cell wall is part of **L15**'s mechanism of action.

SpsB as a putative target could induce the observed morphological changes, although the phenotype looks different to previous EM studies of the SpsB-targeting antibiotic **PK150**<sup>42</sup>, indicating that SpsB is not the sole target of **L15**. Interestingly, EM images also revealed cytoplasmic accumulation of proteins<sup>161,162</sup> that could be caused by dysregulation of SpsB, leading possibly to incomplete protein secretion and, finally, killing of *S. aureus* cells (Figure 22).

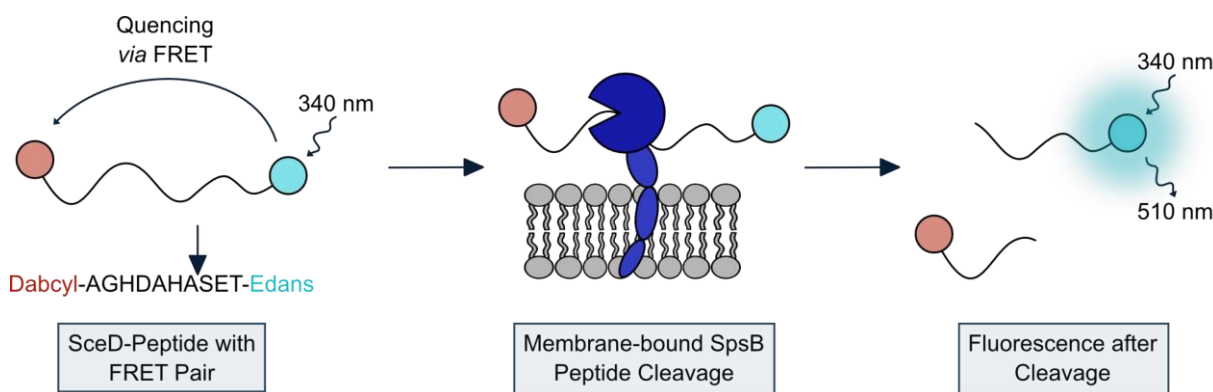


**Figure 22:** Transmission electron microscopy images of *S. aureus* USA300 Lac (JE2) cells treated with **L15** [12.5  $\mu$ M (a) and (b), and 48  $\mu$ M (c)]. Protein accumulations are indicated by the black arrows. The data represent  $n = 2$  biologically independent experiments per condition. Scale bars represent 200 nm.

These findings further strengthen the possible involvement of the cell wall in **L15**'s mechanism of action, either directly or indirectly through the interaction of SpsB.

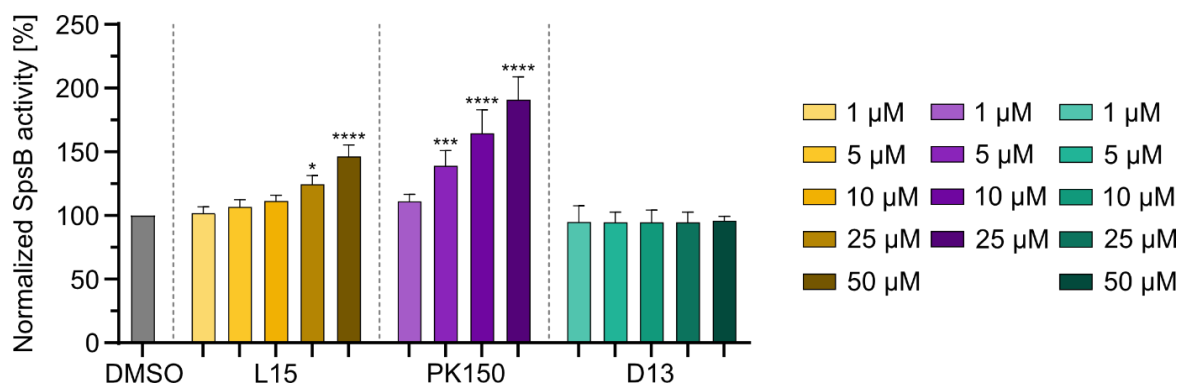
### 1.10. Target Validation Studies by an *in vitro* FRET Assay and Molecular Dynamics

To assess the role of SpsB as a target of **L15**, validation studies by an already established and validated FRET assay were performed<sup>42</sup>. In short, recombinantly overexpressed full-length *S. aureus* SpsB in *E. coli* membranes, purified by *Michaela K. Fiedler*, were treated with the respective compounds. To assess SpsB activity, the cleavage rate was determined by adding a synthetic FRET-based SpsB substrate and measuring the emitted fluorescence (Figure 23).



**Figure 23:** Schematic representation of FRET assay to assess SpsB activity *in vitro*. Membrane-bound SpsB cleaves the modified SceD-peptide between A and S (indicated by an arrow). Consequently, the FRET fluorophore 5-((2-aminoethyl)amino)-1-naphthalenesulfonic (EDANS) acid gets separated from the quencher 4-(4-dimethylaminophenylazo)benzoic (DABCYL) acid, which results in fluorescence emission of EDANS at 510 nm. This figure was adapted from a previous study<sup>163</sup>.

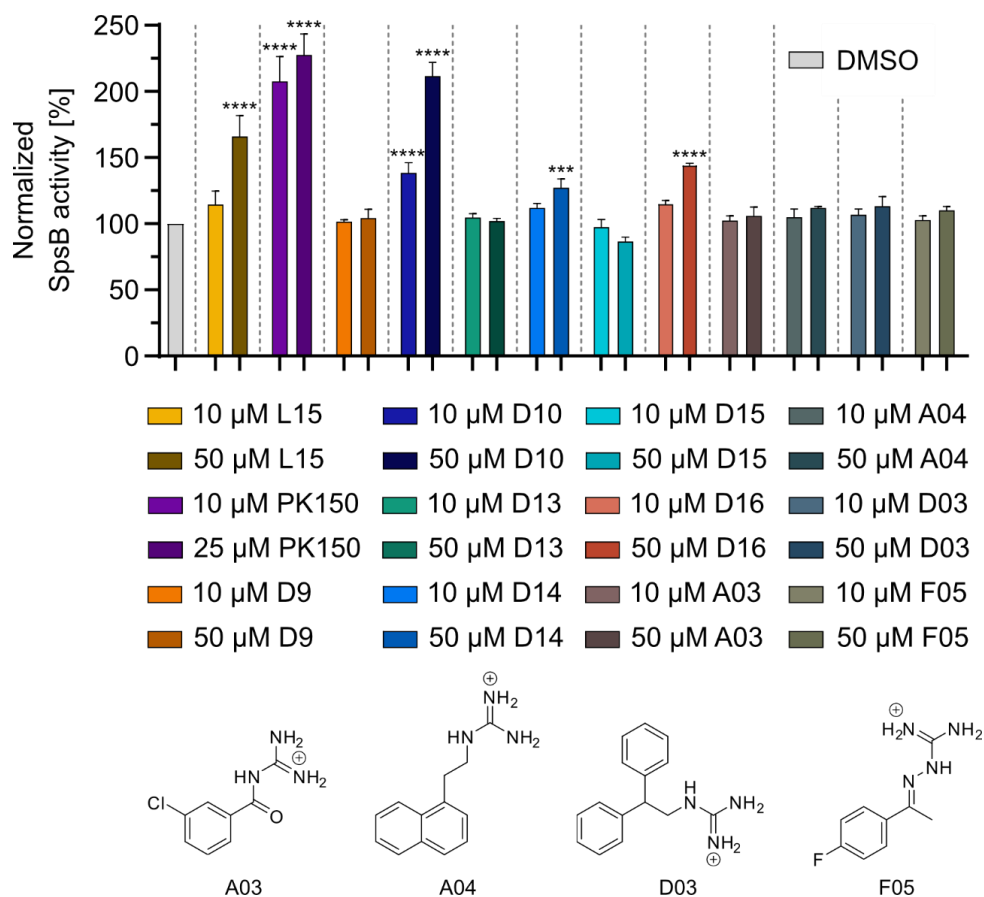
**L15** and the positive control **PK150** showed both a concentration-dependent increase in SpsB activity (Figure 24), whereas **D13**, a less active (MIC = 50  $\mu$ M) but structurally similar derivative of **L15**, showed no effect.



**Figure 24:** Concentration-dependent cleavage of FRET substrate by membrane-bound wild-type SpsB in the presence of **L15**, **D13**, and **PK150**. Membranes were extracted from *E. coli* BL21(DE3) pLysS cells harboring pET-55-DEST-SpsB. Substrate cleavage rates were normalized to DMSO-treated samples from the induced membranes. Background activity from non-induced membranes was subtracted before normalization. The data represent mean values  $\pm$  s.d. of averaged triplicates of  $n = 3$  biologically independent experiments per group. P-values were calculated with one-way ANOVA statistical testing for compound- versus DMSO-treated groups: p-value  $< 0.05$  (\*),  $< 0.01$  (\*\*),  $< 0.001$  (\*\*\*), and  $< 0.0001$  (\*\*\*\*). This figure was adapted from a previous study<sup>66</sup>.

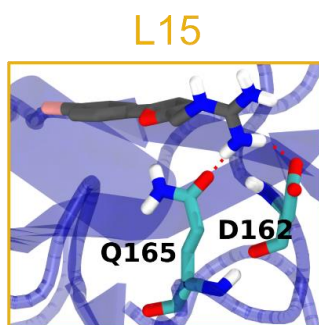
The specificity of **L15** to activate SpsB was proved by comparing its activity to additional compounds from the guanidinium library (**A03**, **A04**, **D03**, and **F05**), that did not show SpsB activation (Figure 25). Those compounds possess different structural features but lacked antibacterial activity in the initial HTS, indicating that the observed effect was not caused by the guanidinium group itself nor induced by membrane-acting properties of these compounds. Besides **L15**, the primary amine (**D14**) and the 2-aminoimidazole (**D16**) derivatives showed a minor activation effect on SpsB activity at 50  $\mu\text{M}$ , indicating that there is still target engagement but to a lesser extent. **D09**, lacking the phenyl ring, did not show an effect, strengthening the necessity of the phenyl ring for **L15**'s biological activity. Interestingly, the thiophene (**D10**) derivative with the highest antibiotic activity (MIC = 0.78  $\mu\text{M}$ ) showed the strongest enhancement in SpsB activation, suggesting stronger target binding of this compound. Overall, SpsB activation of the tested **L15** derivatives correlates with their observed antibacterial activity (Figure 9).





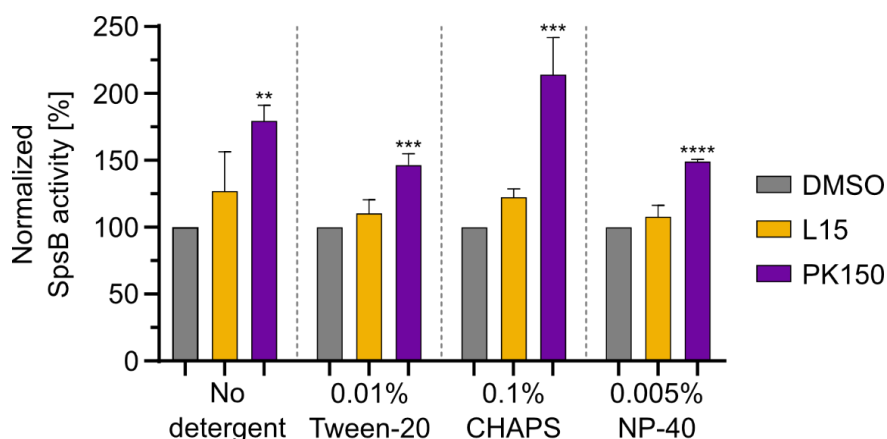
**Figure 25:** Compound-enhanced (10 μM and 50 μM) cleavage of FRET substrate by membrane-bound wild-type SpsB in the presence of various guanidinium compounds, including some derivatives of **L15**. Membranes were extracted from *E. coli* BL21(DE3) pLysS cells harboring pET-55-DEST-SpsB. Substrate cleavage rates were normalized to DMSO-treated samples from the induced membranes. Background activity from non-induced membranes was subtracted before normalization. The data represent mean values ± s.d. of averaged technical duplicates of n = 3 biologically independent experiments per group. P-values were calculated with one-way ANOVA statistical testing for compound- versus DMSO-treated groups: p-value < 0.05 (\*), < 0.01 (\*\*), < 0.001 (\*\*\*), and < 0.0001 (\*\*\*\*). Structures of **A03**, **A04**, **D03**, and **F05** originated from the HTS and were chosen as additional control compounds for the FRET assay. This figure was adapted from a previous study<sup>66</sup>.

Molecular docking experiments of SpsB with bound **L15** were done by *Shu-Yu Chen* and revealed the presence of two H-bonds that are involved in compound binding. The higher activation by **L15** compared to **D14** might therefore be explained by the ability of the guanidinium group to form two H-bonds with D162 and Q165 (Figure 26), whereas the primary amine (**D14**) derivative might lack one of these interactions, highlighting the possible important role of the guanidinium group for SpsB binding.



**Figure 26:** H-bonds of **L15**'s guanidinium group with SpsB residues D162 and Q165. This figure was adapted from a previous study<sup>66</sup>.

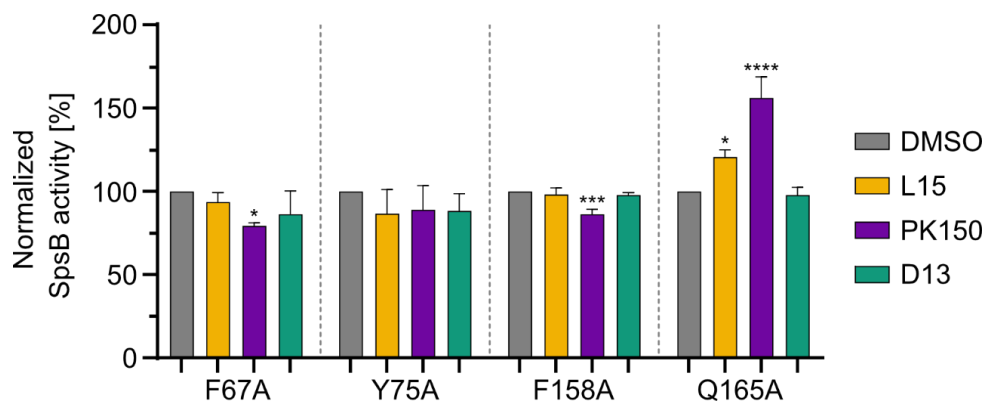
Disturbing the membrane by unspecific compound effects (e.g., accumulation) could influence conformational changes of SpsB and thereby change its activity. To prevent compound aggregation, different detergents below their critical micellar concentrations were tested. Both **L15** and **PK150** still enhanced SpsB turnover, demonstrating a compound-specific effect on SpsB activity (Figure 27).



**Figure 27:** Cleavage of FRET substrate by membrane-bound wild-type SpsB in the presence of **L15**- and **PK150** (10  $\mu$ M) with or without the addition of detergents (below critical micellar concentration: 0.01% Tween-20<sup>164</sup>, 0.001% NP-40<sup>165</sup>, 0.1% CHAPS = 1.6 mM < (5.4 – 11) mM<sup>166,167</sup>). Membranes were extracted from *E. coli* BL21(DE3) pLysS cells harboring pET-55-DEST-SpsB. Substrate cleavage rates were normalized to DMSO-treated samples from the induced membranes. Background activity from non-induced membranes was subtracted before normalization. The data represent mean values  $\pm$  s.d. of averaged triplicates of  $n = 3$  biologically independent experiments per group. P-values were calculated with one-way ANOVA statistical testing for compound- versus DMSO-treated groups: p-value < 0.05 (\*), < 0.01 (\*\*), < 0.001 (\*\*\*), and < 0.0001 (\*\*\*\*). This figure was adapted from a previous study<sup>66</sup>.

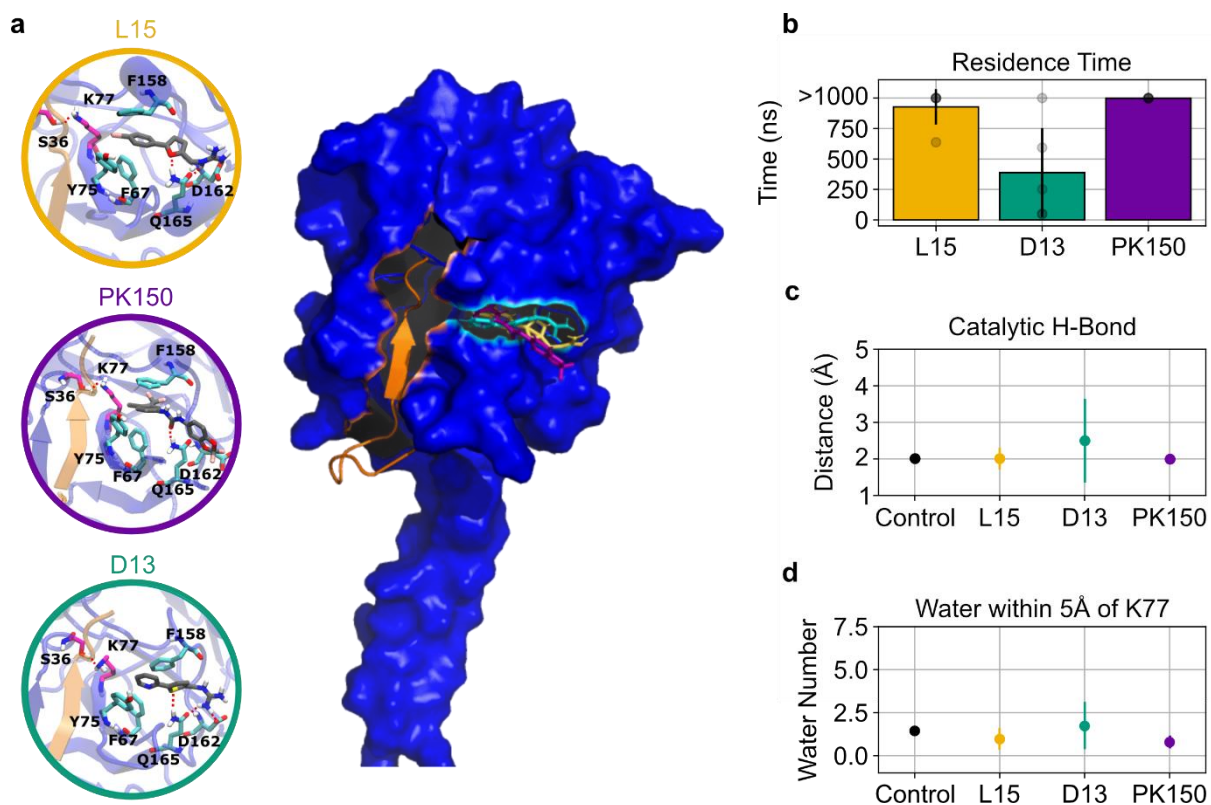
Previous studies on SpsB activation elucidated the binding mechanism of **PK150** in SpsB<sup>163</sup>. Crucial residues of an allosteric pocket, F67, Y75, and F158, were identified to restrict water entering the active site. By **PK150**'s interaction with these residues, water access is limited, stabilizing the catalytic geometry of the active site and enhancing enzyme turnover. The activation effect of **L15** and **PK150** was lost in F67A, Y75A, and F158A mutants (Figure 28), indicating the binding of **L15** to these residues and explaining the activation mechanism. In

contrast, in the control mutant Q165A, which does not affect compound binding, the activation effect of **L15** and **PK150** was still observable.



**Figure 28:** Cleavage of FRET substrate by membrane-bound wild-type SpsB or respective mutants<sup>163</sup> in the presence of **L15**, **D13**, and **PK150** (10  $\mu$ M). Membranes were extracted from *E. coli* BL21(DE3) pLysS cells harboring pET-55-DEST-SpsB. Substrate cleavage rates were normalized to DMSO-treated samples from the induced membranes. Background activity from non-induced membranes was subtracted before normalization. The data represent mean values  $\pm$  s.d. of averaged triplicates of  $n = 3$  biologically independent experiments per group. P-values were calculated with one-way ANOVA statistical testing for compound- versus DMSO-treated groups: p-value < 0.05 (\*), < 0.01 (\*\*), < 0.001 (\*\*\*), and < 0.0001 (\*\*\*\*). This figure was adapted from a previous study<sup>66</sup>.

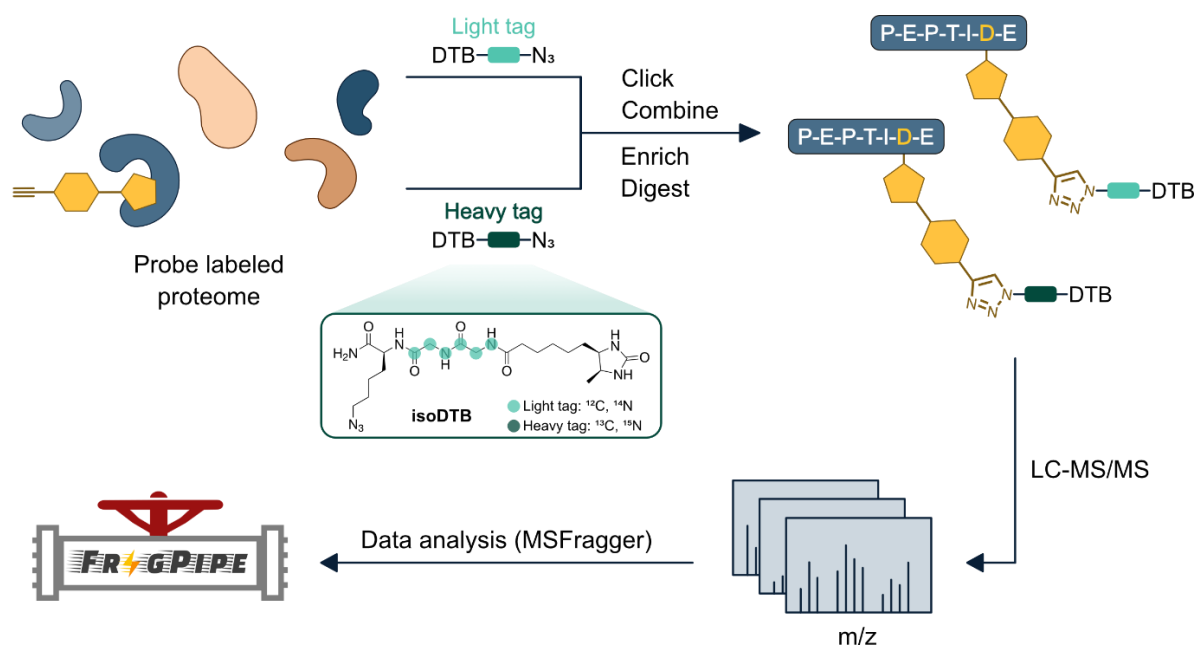
To validate the activation effect of **L15** in SpsB, computational studies were performed by *Shu-Yu Chen*. **L15** was modeled into the previously identified allosteric pocket of SpsB, following subsequent molecular dynamics (MD) studies to analyze enzyme activation (Figure 29). The residence time in holo SpsB (no bound substrate) was higher for **L15** compared to **D13**, correlating with a strong activation effect as previously observed for **PK150**<sup>163</sup> (Figure 29b). H-bond interaction in the catalytic dyad, formed by S36 and K77, was in the optimal required distance for catalysis in the presence of **L15** (Figure 29c). In addition, the catalytic efficiency might be enhanced by a reduced number of water molecules present in the active site (Figure 29d). The optimal requirements for high catalytic efficiency, observed for **L15** and **PK150**, were absent in MD studies with **D13**, which is not able to stabilize the catalytic geometry in the active site of holo SpsB, explaining the specific activation mechanism of **L15**.



**Figure 29:** Molecular dynamics studies of SpsB with bound ligands. (a) Molecular docking of **L15**, **D13**, and **PK150** into the allosteric pocket of SpsB rendered from visual molecular dynamics<sup>168</sup>. During the simulation, **PK150** showed high fluctuation due to the lack of the second H-bond (D162) compared to **L15**. This figure shows one possible docking pose of **PK150**. The red dashed lines highlight H-bonds responsible for catalytic activity (S36 and K77) and binding (D162 and Q165), respectively. (b) Calculated residence time of **L15**, **D13**, and **PK150** in the allosteric pocket of SpsB. Residence times are depicted with the mean (bar plot) and standard deviation  $\pm$  s.d. of  $n = 5$  independently sampled residence times (transparent data points). (c) Catalytic H-bond distance in the catalytic dyad (S36 and K77) induced upon compound binding. (d) Calculated number of water molecules in the vicinity of K77. Filled circles and error bars in c and d show the average  $\pm$  s.d. of  $n = 5$  independent simulations. This figure was adapted from a previous study<sup>66</sup>.

### 1.11. Binding Site Identification Studies by isoDTB Affinity-Based Protein Profiling

With the validated model for SpsB activation by **L15**, the enzymes' binding site was investigated *via* mass spectrometry using isotopically-labeled desthiobiotin (isoDTB) azide tags<sup>169,170</sup>. In short, recombinantly expressed maltose-binding protein (MBP)-tagged SpsB was treated with the photoaffinity probe **L15-P**, and the labeled proteome clicked to either a light or heavy isoDTB tag. Samples were then combined, following enrichment of modified peptides on streptavidin beads, enzymatic digestion, and LC-MS/MS analysis (Figure 30).



**Figure 30:** Schematic representation of the isoDTB A/BPP workflow. The probe-labeled proteome is clicked to light and heavy iso-DTB tags, combined and further processed for LC-MS/MS analysis. Raw MS data was analyzed using MSFragger<sup>171</sup>. This figure was created with Affinity Designer 2.0.

Two modified peptides, VAVNIVGYK (1) and AFGLIDEDQIVGK (2), could be identified that were labeled with **L15-P** (Table 9, Table 10). Peptide 1, which is located in the transmembrane region, could only be modified by **L15-P** in MBP-tagged SpsB due to its inaccessibility under physiological conditions in the native enzyme. However, peptide 2 is located in close proximity to the previously identified allosteric pocket (F67, Y75, and F158), which is crucial for SpsB activation, giving strong evidence that peptide 2 displays the binding site of **L15**.

**Table 9:** Expected and detected mass shifts obtained from the MSFragger OpenSearch<sup>171</sup>. Detected mass shifts were filtered for shifts > 482 Da and mass shift pairs with an exact mass difference of  $6.0075 \pm 0.0010$  Da. This table was adjusted from a previous study<sup>66</sup>.

Expected mass shift (Da)	Detected mass shifts (Da)
838.4419 ( <b>L15-P</b> + heavy tag)	838.4426
832.4344 ( <b>L15-P</b> + light tag)	832.436
	597.357
	591.3506

**Table 10:** Modified closed search analysis using FragPipe<sup>171-175</sup> for binding site identification of **L15-P** to SpsB. This table was adjusted from a previous study<sup>66</sup>.

Identifier	Modified Peptide	Log <sub>2</sub> R Replicate 1	Log <sub>2</sub> R Replicate 2	Log <sub>2</sub> R Replicate 3	Log <sub>2</sub> R Replicate 4	Log <sub>2</sub> R Average
Q2FZT7_D126	AFGLID*EDQIVGK	0.176133	0.352867			0.2645
Q2FZT7_I125	AFGLI*DEDQIVGK			0.343479		0.343479
Q2FZT7_E127	AFGLIDE*DQIVGK				0.028252	0.028252
Q2FZT7_G17	VAVNIVG*YK	0.125478	0.22203	-0.04267	-0.05759	0.061813

## 2. Conclusion

Finding novel antibiotics with unprecedented MoAs still remains very challenging, but is important to tackle AMR in the future.

In this thesis, the success rate of antibiotic hit screening could be significantly enhanced by (1) preselecting the guanidinium group as a privileged scaffold for enhanced bacterial uptake, and (2) mimicking host physiological conditions (25 mM NaHCO<sub>3</sub>). Among the 246 tested compounds (100 μM), six compounds (2%) showed antibacterial activity in the absence of sodium bicarbonate, while 37 compounds (15%) were active in the presence of NaHCO<sub>3</sub>, indicating that this strategy increased antibiotic hit rates. However, there is conflicting evidence regarding whether pH changes are responsible for increased antibiotic activity in susceptibility testing with sodium bicarbonate<sup>69</sup>. This hypothesis has not yet been confirmed for guanidinium antibiotics and requires further investigation in the future.

**L15**, as the most promising compound (MIC = 1.5 μM in *S. aureus*), was selected for SAR studies, revealing the necessity of the guanidinium group for antibacterial activity, as substitution with the corresponding primary amine (**D14**) derivative abolished antibacterial activity. In addition, SAR studies revealed the importance of the phenyl ring for the compound's activity, as well as the positions that tolerated modification. Although **L15** and most of its derivatives showed general toxicity, hemolytic activity was only observed for the thiophene (**D10**) derivative. This compound showed the overall most pronounced effects among the tested derivatives in subsequent experiments (membrane depolarization and FRET-based SpsB assay), suggesting an enhanced target engagement in general. At high concentrations (12 μM), **L15** showed a bactericidal effect as well as an impact on membrane depolarization. Insights from sequencing of **L15**-resistant mutants revealed a mutation in the multidrug efflux pump NorA, indicating an increased efflux of **L15** by NorA as an intrinsic mechanism of resistance. Furthermore, complex proteome changes in *S. aureus* were observed under **L15** stress, with an overall upregulation of stress response systems and proteins involved in cell wall remodeling. The role of the latter in **L15**'s mechanism of action is corroborated by EM studies, showing morphological abnormalities at the cell wall at high compound concentrations (12.5 μM and 48 μM). Chemical proteomics then revealed two essential protein targets. Among them, the bacterial signal peptidase IB, which plays an essential role in the secretion of bacterial proteins, including autolysins, could be validated as a target of **L15** using a FRET-based SpsB assay, molecular dynamics and binding site studies. The computational data suggests binding of **L15** to an allosteric pocket in close proximity to the active site, restricting water access and thereby stabilizing the catalytic geometry, which finally enhances the enzymatic turnover. In addition, dysregulation of protein secretion by activation of SpsB was

further supported by full proteome (upregulation of autolysins) and EM (cytoplasmic aggregation of proteins) studies.

Taken together, the results suggest that **L15** likely operates through a polypharmacological mechanism of action, leading to bacterial cell death. Notably, activating SpsB is an unconventional and less explored approach to dysregulate the bacterial physiology. This disruption in protein secretion could cause uncontrolled release of autolysins and intracellular protein accumulation, which interferes with cellular processes. A similar mechanism has also been observed with the small molecule antibiotic **PK150**<sup>42</sup>, indicating it may be a more common phenomenon with potential physiological significance in *S. aureus*.

By screening privileged guanidinium compounds in conditions that mimic the host environment, the success rate of discovering new antibiotics could be improved. Integrating this strategy with comprehensive MoA studies and a strong target identification platform allowed for the investigation of **L15**'s activity in *S. aureus*. This work underscores the importance of rethinking antibiotic discovery by employing unconventional screening methods and innovative approaches to uncover new antibiotics.

### 3. Supplementary Information

#### 3.1. Supplementary Tables S1 – S2

**Table S1:** Compound list (SMILES and names) from guanidinium HTS. The addition of NaHCO<sub>3</sub> (25 mM) increased the hit rate from 6 to 37 compounds with antibiotic activity in *E. coli* K12. Hits are highlighted in yellow.

Smile	Name	Hit (no NaHCO <sub>3</sub> )	Hit (25 mM NaHCO <sub>3</sub> )
<chem>Cl.NC(=N)NC(=O)C=1C=CC=C(Cl)C1</chem>	N-carbamimidoyl-3-chlorobenzamide hydrochloride	0	0
<chem>Cl.NC(=N)NC(=O)C=1C=CC=C(C1S(=O)(=O)N2CCCCC2)</chem>	N-carbamimidoyl-3-(piperidine-1-sulfonyl)benzamide hydrochloride	0	0
<chem>Cl.NC(=N)NC(=O)NC=1C=CC=C(Cl)C1</chem>	3-carbamimidoyl-1-(3-chlorophenyl)urea hydrochloride	0	0
<chem>I.NC(=N)NCC(C=1C=CC=CC1)C=2C=CC=CC2</chem>	N-(2,2-diphenylethyl)guanidine hydroiodide	0	0
<chem>Cl.COC=1C=C(NC(=N)NC(=N)N)C(OC)=CC1Cl</chem>	1-carbamimidamido-N-(4-chloro-2,5-dimethoxyphenyl)methanimidamide hydrochloride	0	0
<chem>Cl.NC(=N)NC(=N)NC=1C=C(Cl)C=C(Cl)C1</chem>	1-carbamimidamido-N-(3,5-dichlorophenyl)methanimidamide hydrochloride	0	0
<chem>CC(=NNC(=N)N)C=1C=CC(=CC1)N2C=CN=C2</chem>	N-({1-[4-(1H-imidazol-1-yl)phenyl]ethylidene}amino)guanidine	0	0
<chem>CC(=O)O.CC(=NNC(=N)N)C=1C=CC(=CC1)C2CCCCC2</chem>	N-([1-(4-cyclohexylphenyl)ethylidene]amino)guanidine; acetic acid	1	1
<chem>Cl.CC(=O)C=1C=CC(NC(=N)NC(=N)N)=CC1</chem>	N-(4-acetylphenyl)-1-carbamimidamidomethanimidamide hydrochloride	0	0
<chem>NC(=N)NN=CC(=CC=1C=CC=CC1)Cl</chem>	N-[(2-chloro-3-phenylprop-2-en-1-ylidene)amino]guanidine	0	0
<chem>NC(=N)NN=CC=1C=CC(Cl)=C(Cl)C1</chem>	N-[(3,4-dichlorophenyl)methylidene]amino)guanidine	0	1



Br.NC(=N)NCC1COC=2C=CC=CC2O1	N-[(2,3-dihydro-1,4-benzodioxin-2-yl)methyl]guanidine hydrobromide	0	0
I.NC(=N)NCC(CC=1C=CC=CC1)C=2C=CC=C C2	N-(2,3-diphenylpropyl)guanidine hydroiodide	0	1
I.NC(=N)NCC1(CCCC1)C=2C=CC(F)=CC2	N-[(1-(4-fluorophenyl)cyclopentyl)methyl]guanidine hydroiodide	0	0
I.NC(=N)NCC1=CSC=2C=CC=CC12	N-[(1-benzothiophen-3-yl)methyl]guanidine hydroiodide	0	0
Br.COC=1C=CC(=CC1)C(CNC(=N)N)N2CCC CC2	N-[2-(4-methoxyphenyl)-2-(piperidin-1-yl)ethyl]guanidine hydrobromide	0	0
Br.NC(=N)NCCC=1C=CC=C2C=CC=CC12	N-[2-(naphthalen-1-yl)ethyl]guanidine hydrobromide	0	0
I.NC(=N)NCC1CCCN(CC=2C=CC=CC2)C1	N-[(1-benzylpiperidin-3-yl)methyl]guanidine hydroiodide	0	0
I.NC(=N)NCC(=O)NC=1C=CC=C(C#C)C1	2-carbamimidamido-N-(3-ethynylphenyl)acetamide hydroiodide	0	0
I.NC(=N)NCC=1C=C(Br)C=CC1F	N-[(5-bromo-2-fluorophenyl)methyl]guanidine hydroiodide	0	0
I.NC(=N)NCCOC=1C=CC=2C=CC=CC2C1	N-[2-(naphthalen-2-yloxy)ethyl]guanidine hydroiodide	0	1
I.NC(=N)NCC=1C=CC=CC1SC=2C=CC=CC2	N-[(2-(phenylsulfanyl)phenyl)methyl]guanidine hydroiodide	0	1
I.NC(=N)NCCC(C=1C=CC=CC1)C=2C=CC=C C2	N-(3,3-diphenylpropyl)guanidine hydroiodide	0	1
I.CC=1C=CC=C(C1)C2(CNC(=N)N)CCCC2	N-[(1-(3-methylphenyl)cyclopentyl)methyl]guanidine hydroiodide	0	0
I.NC(=N)NCC=1C=CC(CN2CCCCCCC2)=CC 1	N-[(4-{(azocan-1-yl)methyl}phenyl)methyl]guanidine hydroiodide	0	0
Cl.CC=1C=CC=2C=CC=C(NC(=N)N)C2N1	N-(2-methylquinolin-8-yl)guanidine hydrochloride	0	0
CC(=NNC(=N)N)C=1C=CC(=CC1)N2CCCC C2	N-[(1-[4-(azepan-1-yl)phenyl]ethylidene)amino]guanidine	0	1
NC(=N)NN=CC1=CN(N=C1C2=CC=CS2)C=3 C=CC=CC3	N-[(1-phenyl-3-(thiophen-2-yl)-1H-pyrazol-4-yl)methylidene]amino)guanidine	1	1
COC=1C=CC(=CC1)C(=O)C=CNC=2C=CC(=CC2)S(=O)(=O)NC(=N)N	N-(4-[[3-(4-methoxyphenyl)-3-oxoprop-1-en-1-yl]amino]benzenesulfonyl)guanidine	0	0
Cl.NC(=N)NC(=N)NC=1C=CC=2OCOC2C1	N-(2H-1,3-benzodioxol-5-yl)-1-carbamimidamidomethanimidamide hydrochloride	0	0
COC=1C=C(C=NNC(=N)N)C=CC1OC(=O)C2=CC=CO2.O[N+](=O)[O-]	4-[(carbamimidamidoimino)methyl]-2-methoxyphenyl furan-2-carboxylate; nitric acid	0	0
COC=1C=CC(=CC1OC)C2=NN(C=C2C=NNC(=N)N)C=3C=CC=CC3	N-[(3-(3,4-dimethoxyphenyl)-1-phenyl-1H-pyrazol-4-yl)methylidene]amino)guanidine	0	0
COC(=O)C=1C=CC(C=NNC(=N)N)=CC1	methyl 4-[(carbamimidamidoimino)methyl]benzoate	0	0
COC=1C=C(C=NNC(=N)N)C=CC1O	N-[(4-hydroxy-3-methoxyphenyl)methylidene]amino)guanidine	0	0
COC=1C=CC(C=NNC(=N)N)=C(OC)C1OC	N-[(2,3,4-trimethoxyphenyl)methylidene]amino)guanidine	0	0
NC(=N)NN=CC=1C=C(Cl)C=C([N+](=O)[O-])C1O	N-[(5-chloro-2-hydroxy-3-nitrophenyl)methylidene]amino)guanidine	0	0
NC(=N)NN=CC=1C=CC=C(OCC=2C=CC=CC2)C1	N-[(3-(benzyloxy)phenyl)methylidene]amino)guanidine	0	1
CC(=NNC(=N)N)C=1C=CC(F)=CC1	N-[(1-(4-fluorophenyl)ethylidene)amino]guanidine	0	0
NC(=N)NN=CC=1C=CC(C#N)=CC1	N-[(4-cyanophenyl)methylidene]amino)guanidine	0	0
CCOC=1C=CC=C(C=NNC(=N)N)C1O	N-[(3-ethoxy-2-hydroxyphenyl)methylidene]amino)guanidine	0	0
CCOC=1C=CC(C=NNC(=N)N)=CC1OC	N-[(4-ethoxy-3-methoxyphenyl)methylidene]amino)guanidine	0	0
NC(=N)NN=CC=1C=CC(Cl)=C(C1)[N+](=O)[O-]	N-[(4-chloro-3-nitrophenyl)methylidene]amino)guanidine	0	0
CC(=NNC(=N)N)C=1C=CC=C(C1)[N+](=O)[O-]	N-[(1-(3-nitrophenyl)ethylidene)amino]guanidine	0	0



<chem>CC(=NNC(=N)N)C=1C=CC(Cl)=CC1</chem>	N-([1-(4-chlorophenyl)ethylidene]amino)guanidine	0	0
<chem>CC(=NNC(=N)N)C1=CC=CO1</chem>	N-([1-(furan-2-yl)ethylidene]amino)guanidine	0	0
<chem>NC(=N)NN=CC=1C=CC=CC1C(F)(F)F</chem>	N-([2-(trifluoromethyl)phenyl]methylidene)amino)guanidine	0	0
<chem>COC=1C=C(C=NNC(=N)N)C=C(OC)C1O</chem>	N-([4-hydroxy-3,5-dimethoxyphenyl]methylidene)amino)guanidine	0	0
<chem>CC(=NNC(=N)N)C=1C=CC=C(Cl)C1</chem>	N-([1-(3-chlorophenyl)ethylidene]amino)guanidine	0	0
<chem>CC(=NNC(=N)N)C=1C=CC(Cl)=CC1Cl</chem>	N-([1-(2,4-dichlorophenyl)ethylidene]amino)guanidine	0	0
<chem>CC(=O)O.NC(=N)NN=CC=1C=CC=CC1OC(F)F</chem>	N-([2-(difluoromethoxy)phenyl]methylidene)amino)guanidine; acetic acid	0	0
<chem>CC(=O)O.CC(=NNC(=N)N)C1=CC=C(Cl)S1</chem>	N-([1-(5-chlorothiophen-2-yl)ethylidene]amino)guanidine; acetic acid	0	0
<chem>COC=1C=CC(C=NNC(=N)N)C=C(O)C1</chem>	N-([1-(2-hydroxy-4-methoxyphenyl)ethylidene]amino)guanidine	0	0
<chem>CCOC=1C=C(C=NNC(=N)N)C=CC1O.CC(=O)O</chem>	N-([3-ethoxy-4-hydroxyphenyl]methylidene)amino)guanidine; acetic acid	0	0
<chem>COC=1C=CC(C=NNC(=N)N)C=C(OC)C1</chem>	N-([1-(2,4-dimethoxyphenyl)ethylidene]amino)guanidine	0	0
<chem>COC=1C=CC(=CC1OC)C(=NNC(=N)N)C</chem>	N-([1-(3,4-dimethoxyphenyl)ethylidene]amino)guanidine	0	0
<chem>NC(=N)NN=CC=1C=C2OCOC2=CC1[N+](=O)[O-]</chem>	N-([6-nitro-2H-1,3-benzodioxol-5-yl]methylidene)amino)guanidine	0	0
<chem>Cl.NC(=N)NC(=N)NC=1C=CC(F)=C(Cl)C1</chem>	1-carbamimidamido-N-(3-chloro-4-fluorophenyl)methanimidamide hydrochloride	0	0
<chem>CCC=1N=C(NC(=N)N)N=C2C=C(C)C=CC12</chem>	N-(4-ethyl-7-methylquinazolin-2-yl)guanidine	0	1
<chem>CC(=O)O.CC(=NNC(=N)N)C=1C=CC(Cl)=C(Cl)C1</chem>	N-([1-(3,4-dichlorophenyl)ethylidene]amino)guanidine; acetic acid	0	0
<chem>Cl.NC(=N)NC(=N)NC=1C=CC(SC(F)F)=CC1</chem>	1-carbamimidamido-N-([4-(difluoromethyl)sulfanyl]phenyl)methanimidamide hydrochloride	0	0
<chem>I.NC(=N)NCC1=CC=C(Cl)S1</chem>	N-([5-chlorothiophen-2-yl]methyl]guanidine hydroiodide	0	0
<chem>Cl.CC(=NNC(=N)N)C=1C=CC(=CC1)S(=O)(=O)NCC2=CC=CO2</chem>	N-([1-(4-([furan-2-yl]methyl)sulfamoyl]phenyl)ethylidene]amino)guanidine hydrochloride	0	0
<chem>I.NC(=N)NCC=1C=CC(Cl)=CC1Cl</chem>	N-([2,4-dichlorophenyl]methyl]guanidine hydroiodide	0	0
<chem>CC(=NNC(=N)N)C=1C=CC=CC1Cl</chem>	N-([1-(2-chlorophenyl)ethylidene]amino)guanidine	0	0
<chem>NC(=N)NN=CC=1C=CC=C([N+](=O)[O-])C1O</chem>	N-([2-hydroxy-3-nitrophenyl]methylidene]amino)guanidine	0	0
<chem>NC(=N)NN=CC(=CC=1C=CC=CC1)Br</chem>	N-([2-bromo-3-phenylprop-2-en-1-ylidene]amino)guanidine	0	1
<chem>COC=1C=CC(=CC1OC)C(=O)C=CNC=2C=C(C=CC2)S(=O)(=O)NC(=N)N</chem>	N-(4-([3-(3,4-dimethoxyphenyl)-3-oxoprop-1-en-1-yl]amino)benzenesulfonyl)guanidine	0	0
<chem>CC(=NNC(=N)N)CCC=1C=CC=2OCOC2C1.O[N+](=O)[O-]</chem>	N-([4-(2H-1,3-benzodioxol-5-yl)butan-2-ylidene]amino)guanidine; nitric acid	0	0
<chem>CC1=CC(C=NNC(=N)N)=C(C)N1C=2C=C(C=CC2N3CCCC3)S(=O)(=O)N4CCOCC4.O[N+](=O)[O-]</chem>	N-([2,5-dimethyl-1-[5-(morpholine-4-sulfonyl)-2-(pyrrolidin-1-yl)phenyl]-1H-pyrrol-3-yl]methylidene)amino)guanidine; nitric acid	0	0
<chem>Cl.NC(=N)NC(=N)N1CCCC=2C=CC=CC12</chem>	N-(1,2,3,4-tetrahydroquinoline-1-carboximidoyl)guanidine hydrochloride	0	0
<chem>NC(=N)NN=CC=1C=C(Br)C(O)=C(Br)C1</chem>	N-([3,5-dibromo-4-hydroxyphenyl]methylidene]amino)guanidine	0	0
<chem>CC(=CC=1C=CC=CC1)C=NNC(=N)N</chem>	N-([2-methyl-3-phenylprop-2-en-1-ylidene]amino)guanidine	0	0
<chem>COC=1C=C(C=NNC(=N)N)C=C(Br)C1O</chem>	N-([3-bromo-4-hydroxy-5-methoxyphenyl]methylidene]amino)guanidine	0	0
<chem>CCCOC=1C=CC(C=NNC(=N)N)=C(O)C1</chem>	N-([2-hydroxy-4-propoxyphenyl]methylidene]amino)guanidine	0	0

<chem>NC(=N)NN=CC=1C=CC(OCC=2C=CC=CC2)=C(OCC=3C=CC=CC3)C1</chem>	N-({[3,4-bis(benzyloxy)phenyl]methylidene}amino)guanidine	0	0
<chem>CC=1C=CC(=CC1)S(=O)(=O)NC(=N)N</chem>	N-(4-methylbenzenesulfonyl)guanidine	0	0
<chem>CCCCCN1C(=O)C(=NNC(=N)N)C=2C=CC=C12</chem>	N-[(2-oxo-1-pentyl-2,3-dihydro-1H-indol-3-ylidene)amino]guanidine	0	0
<chem>Cl.NC(=N)NC(=N)NC=1C=CC(F)=CC1</chem>	1-carbamimidamido-N-(4-fluorophenyl)methanimidamide hydrochloride	0	0
<chem>Cl.NC(=N)NN=C1C(=O)NC=2C=CC(Br)=CC12</chem>	N-[(5-bromo-2-oxo-2,3-dihydro-1H-indol-3-ylidene)amino]guanidine hydrochloride	0	0
<chem>Cl.CCOC=1C=C(C(=NNC(=N)N)C=CC1OCC(=O)N</chem>	2-{4-[(carbamimidamidoimino)methyl]-2-ethoxyphenoxy}acetamide hydrochloride	0	0
<chem>O.C[C@@H]1CCN([C@H](C1)C(=O)O)C(=O)[C@H](CCCNC(=N)N)NS(=O)(=O)C=2C=CC=C3CC(C)CNC23</chem>	(2R,4R)-1-[(2S)-5-carbamimidamido-2-(3-methyl-1,2,3,4-tetrahydroquinoline-8-sulfonamido)pentanoyl]-4-methylpiperidine-2-carboxylic acid hydrate	0	0
<chem>Br.CN1CCCC(CNC(=N)N)C1</chem>	N-[(1-methylpiperidin-3-yl)methyl]guanidine hydrobromide	0	0
<chem>NC(=N)NC=1C=CC(=CC1C(F)(F)F)N2C=CN=C2</chem>	N-[4-(1H-imidazol-1-yl)-2-(trifluoromethyl)phenyl]guanidine	0	0
<chem>NC(=N)NN=CC1=CC=C(S1)C=2C=CC(Cl)=C2</chem>	N-({[5-(4-chlorophenyl)thiophen-2-yl]methylidene}amino)guanidine	1	1
<chem>COC=1C=C(C=NNC(=N)N)C=C2OCOC21</chem>	N-({[7-methoxy-2H-1,3-benzodioxol-5-yl]methylidene}amino)guanidine	0	0
<chem>NC(=N)NN=CC=1C=CSC1C(F)(F)F</chem>	N-({[2-(trifluoromethyl)thiophen-3-yl]methylidene}amino)guanidine	0	0
<chem>COC1=NSC=C1C=NNC(=N)N</chem>	N-({[3-methoxy-1,2-thiazol-4-yl]methylidene}amino)guanidine	0	0
<chem>Cl.Cl.NC(=N)NCCCC(=O)N1CCOC(C1)C=2C=CC=CC2</chem>	N-[5-oxo-5-(2-phenylmorpholin-4-yl)pentyl]guanidine dihydrochloride	0	0
<chem>CC(=O)N(C1CC1)C2=NC(C=NNC(=N)N)=CS2</chem>	N-[4-[(carbamimidamidoimino)methyl]-1,3-thiazol-2-yl]-N-cyclopropylacetamide	0	0
<chem>NC(=N)NN=CC=1C=CC=C(OCC=2C=CC(F)=CC2)C1</chem>	N-({[3-[(4-fluorophenyl)methoxy]phenyl]methylidene}amino)guanidine	0	1
<chem>COC=1C=CC=C(C1)C2=NNC=C2C=NNC(=N)N</chem>	N-({[3-(3-methoxyphenyl)-1H-pyrazol-4-yl]methylidene}amino)guanidine	0	0
<chem>CC(=NNC(=N)N)C1=CSC(=C1)C2=CSC(C)=N2</chem>	N-({[1-[5-(2-methyl-1,3-thiazol-4-yl)thiophen-3-yl]ethylidene}amino)guanidine	0	0
<chem>NC(=N)NN=CC=1C=CC(OC=2C=CC=CC2F)=C(F)C1</chem>	N-({[3-fluoro-4-(2-fluorophenoxy)phenyl]methylidene}amino)guanidine	1	1
<chem>NC(=N)NN=CC=1C=CN=C2C=CC=CC12</chem>	N-({[quinolin-4-yl]methylidene}amino)guanidine	0	0
<chem>Cl.Cl.NC(=N)NC(=O)C1CCCN(CCC=2C=CC=CC2)C1</chem>	N-carbamimidoyl-1-(2-phenylethyl)piperidine-3-carboxamide dihydrochloride	0	0
<chem>Cl.NC(=N)NC(=O)C=1C=CC=C(C1)C(=O)N2CCCC2</chem>	N-carbamimidoyl-3-(piperidine-1-carbonyl)benzamide hydrochloride	0	0
<chem>NC(=N)NN=CC1=CN=C(S1)N2CCOCC2</chem>	N-({[2-(morpholin-4-yl)-1,3-thiazol-5-yl]methylidene}amino)guanidine	0	0
<chem>Br.CC(C)(O)CN1CC[C@@H](C1)NC(=N)N</chem>	N-[(3S)-1-(2-hydroxy-2-methylpropyl)pyrrolidin-3-yl]guanidine hydrobromide	0	0
<chem>Br.NC(=N)NCC1(CCSC1)N2CCOCC2</chem>	N-({[3-(morpholin-4-yl)thiolan-3-yl]methyl]guanidine hydrobromide	0	0
<chem>I.NC(=N)NCC=1C=CC=C(C1)S(=O)(=O)NCC=2C=CC=C(F)C2</chem>	N-[(3-[(3-fluorophenyl)methyl]sulfamoyl)phenyl]methylguanidine hydroiodide	0	0
<chem>Cl.CC(=CC1=CC=CS1)C(=O)NC(=N)N</chem>	N-carbamimidoyl-2-methyl-3-(thiophen-2-yl)prop-2-enamide hydrochloride	0	0
<chem>Cl.NC(=N)NC(=O)CC=1C=CSC1</chem>	N-carbamimidoyl-2-(thiophen-3-yl)acetamide hydrochloride	0	0
<chem>Cl.NC(=N)NC(=O)C1=CC=C(Cl)O1</chem>	N-carbamimidoyl-5-chlorofuran-2-carboxamide hydrochloride	0	0
<chem>Cl.NC(=N)NC(=O)C=1C=CC=CC1OCC=2C=C(C(Cl)=CC2</chem>	N-carbamimidoyl-2-[(4-chlorophenyl)methoxy]benzamide hydrochloride	0	0
<chem>Br.CN1C=C(C=N1)C(O)CNC(=N)N</chem>	N-[2-hydroxy-2-(1-methyl-1H-pyrazol-4-yl)ethyl]guanidine hydrobromide	0	0
<chem>NC(=N)NN=CC=1C=CC(Cl)=C(C1)C(F)(F)F</chem>	N-({[4-chloro-3-(trifluoromethyl)phenyl]methylidene}amino)guanidine	0	1

NC(=N)NC=1C=CC(=CC1C(F)(F)F)N2C=CC=N2	N-[4-(1H-pyrazol-1-yl)-2-(trifluoromethyl)phenyl]guanidine	0	0
I.CC=1C=CC=C(C1)C=2C=CC=C(CNC(=N)N)C2	N-({3'-methyl-[1,1'-biphenyl]-3-yl)methyl}guanidine hydroiodide	0	1
I.CC(C)NS(=O)(=O)C=1C=CC=C(CNC(=N)N)C1	N-({3-[(propan-2-yl)sulfamoyl]phenyl)methyl}guanidine hydroiodide	0	0
COC=1C=CC(OC=2C=CC(=CC2)S(=O)(=O)N(CCCNC(=N)N)CCCNC(=N)N)=CC1	N-{3-[N-(3-carbamimidamidopropyl)4-(4-methoxyphenoxy)benzenesulfonamido]propyl}guanidine	0	0
I.CC(C)(CNC(=N)N)C=1C=CC=C(F)C1	N-[2-(3-fluorophenyl)-2-methylpropyl]guanidine hydroiodide	0	0
I.NC(=N)NCCC=1C=CC=CN1	N-[2-(pyridin-2-yl)ethyl]guanidine hydroiodide	0	0
CC(=O)O.NC(=N)NN=CC1=CC=C(S1)N2CCCCC2	N-({[5-(piperidin-1-yl)thiophen-2-yl]methylidene}amino)guanidine; acetic acid	0	0
I.NC(=N)NC1CCOCC1	N-(oxan-4-yl)guanidine hydroiodide	0	0
I.NC(=N)NCCC=1C=CC(=CC1)S(=O)(=O)N	N-[2-(4-sulfamoylphenyl)ethyl]guanidine hydroiodide	0	0
Br.NC(=N)NCC(N1CCCC1)C2=CC=CO2	N-[2-(furan-2-yl)-2-(piperidin-1-yl)ethyl]guanidine hydrobromide	0	0
Br.NC(=N)NCCN1CCN(CC=2C=CC=CC2)CC1	N-[2-(4-benzylpiperazin-1-yl)ethyl]guanidine hydrobromide	0	0
I.CC(C)(CNC(=N)N)N1CCC=2C=CC=CC2C1	N-[2-methyl-2-(1,2,3,4-tetrahydroisoquinolin-2-yl)propyl]guanidine hydroiodide	0	0
I.NC(=N)NCC=1C=CN=C(C1)N2CCCC2	N-({[2-(pyrrolidin-1-yl)pyridin-4-yl]methyl}guanidine hydroiodide	0	0
Br.NC(=N)NCC=1C=CC(CN2CCCC2)=CC1	N-({[4-(pyrrolidin-1-yl)methyl]phenyl}methyl)guanidine hydrobromide	0	0
I.NC(=N)NCC(O)C=1C=CC=CC1F	N-[2-(2-fluorophenyl)-2-hydroxyethyl]guanidine hydroiodide	0	0
I.NC(=N)NCC=1C=CC=C(C#N)C1	N-[(3-cyanophenyl)methyl]guanidine hydroiodide	0	0
I.NC(=N)NCC1(CC2CC3CC(C2)C1)C3	N-[(adamantan-1-yl)methyl]guanidine hydroiodide	0	0
I.NC(=N)NCCCCN1CCN(CC1)C=2C=CC=C(C2)C(F)(F)F	N-(4-{4-[3-(trifluoromethyl)phenyl]piperazin-1-yl}butyl)guanidine hydroiodide	0	0
I.CC1CCN(CC1)C(CNC(=N)N)C2=CC=CS2	N-[2-(4-methylpiperidin-1-yl)-2-(thiophen-2-yl)ethyl]guanidine hydroiodide	0	0
I.NC(=N)NCC1(CCCCC1)N2CCCCC2	N-([1-(piperidin-1-yl)cyclohexyl]methyl)guanidine hydroiodide	0	0
I.NC(=N)NCC=1C=CC=NC1	N-[(pyridin-3-yl)methyl]guanidine hydroiodide	0	0
NC(=N)NC1=NC=2C=CC(=CC2N1)S(=O)(=O)N3CCOCC3	N-[6-(morpholine-4-sulfonyl)-1H-1,3-benzodiazol-2-yl]guanidine	0	0
CC(=O)O.CC1=CC=C(C=NNC(=N)N)S1	N-({[5-methylthiophen-2-yl]methylidene}amino)guanidine; acetic acid	0	0
CC(=O)O.CC=1C=CSC1C=NNC(=N)N	N-({[3-methylthiophen-2-yl]methylidene}amino)guanidine; acetic acid	0	0
CC(=O)O.CC(=NNC(=N)N)C=1C=CC(=CC1)N2CCOCC2	N-({[1-[4-(morpholin-4-yl)phenyl]ethylidene]amino}guanidine; acetic acid	0	0
CCCN1CCC(=NNC(=N)N)CC1.CC(=O)O	N-[(1-propylpiperidin-4-ylidene)amino]guanidine; acetic acid	0	0
NC(=N)NN=C1C=2C=CC=CC2C=3C=CC=CC13	N-[(9H-fluoren-9-ylidene)amino]guanidine	0	0
CC(=O)O.NC(=N)NN=CC=1C=CC(OC(F)F)=C1	N-({[4-(difluoromethoxy)phenyl]methylidene}amino)guanidine; acetic acid	0	0
NC(=N)NN=C1C(=O)NC=2C=CC=CC12	N-[(2-oxo-2,3-dihydro-1H-indol-3-ylidene)amino]guanidine	0	0
Br.NC(=N)NCC=1C=CC=CN1	N-[(pyridin-2-yl)methyl]guanidine hydrobromide	0	0
I.NC(=N)NCC1CCCO1	N-[(oxolan-2-yl)methyl]guanidine hydroiodide	0	0
I.NC(=N)NCCCN1CCCC1	N-[3-(pyrrolidin-1-yl)propyl]guanidine hydroiodide	0	0
NC(=N)NCCN1CCOCC1.OC(=O)C(=O)O	N-[2-(morpholin-4-yl)ethyl]guanidine; oxalic acid	0	0
CC(=O)O.NC(=N)NN=C1CCC(CC1)C=2C=CC=CC2	N-[(4-phenylcyclohexylidene)amino]guanidine; acetic acid	0	0
CC(=NNC(=N)N)C1CCCC1	N-[(1-cyclohexylethylidene)amino]guanidine	0	0

Br.CN(C)C(CNC(=N)N)C1=CC=CS1	N-[2-(dimethylamino)-2-(thiophen-2-yl)ethyl]guanidine hydrobromide	0	0
NC(=N)NCC=1C=CC=2OCCCC2C1.OS(=O)(=O)C(F)(F)F	N-[(2,3-dihydro-1-benzofuran-5-yl)methyl]guanidine; trifluoromethanesulfonic acid	0	0
I.CC(C)C(CNC(=N)N)N(CC=C)CC=C	N-{2-[bis(prop-2-en-1-yl)amino]-3-methylbutyl}guanidine hydroiodide	0	1
I.NC(=N)NCC=1C=CC(CN2CCOCC2)=CC1	N-[(4-[(morpholin-4-yl)methyl]phenyl)methyl]guanidine hydroiodide	0	0
COC=1C=CC(CC(=NNC(=N)N)C)=CC1	N-[[1-(4-methoxyphenyl)propan-2-ylidene]amino]guanidine	0	0
Br.CC1=CCN(CCNC(=N)N)CC1	N-[2-(4-methyl-1,2,3,6-tetrahydropyridin-1-yl)ethyl]guanidine hydrobromide	0	0
I.CC=1C=CC(OC=2C=C(CNC(=N)N)C=CN2)=CC1C	N-[[2-(3,4-dimethylphenoxy)pyridin-4-yl]methyl]guanidine hydroiodide	0	0
I.CC(NC(=N)N)C=1C=CC=CC1	N-(1-phenylethyl)guanidine hydroiodide	0	0
I.CN(CCNC(=N)N)C1CC1	N-{2-[cyclopropyl(methyl)amino]ethyl}guanidine hydroiodide	0	0
Br.NC(=N)NCCCNC=1C=CC(=CN1)C(F)(F)F	N-(3-[[5-(trifluoromethyl)pyridin-2-yl]amino]propyl)guanidine hydrobromide	0	0
I.CC1=CC=C(CCNC(=N)N)O1	N-[2-(5-methylfuran-2-yl)ethyl]guanidine hydroiodide	0	0
NC(=N)NN=CC=1C=CC=CC1Br	N-[[2-(bromophenyl)methylidene]amino]guanidine	0	0
NC(=N)NC(=O)NC=1C=CC(C#N)=C(CI)C1	3-carbamimidoyl-1-(3-chloro-4-cyanophenyl)urea	0	0
NC(=N)NN=CC1=CN(N=C1C=2C=CC=CC2)C=3C=CC=CC3	N-[[1-(3-diphenyl-1H-pyrazol-4-yl)methylidene]amino]guanidine	0	1
CC=1C=C2N=C(NC(=N)N)N=C(C)C2=CC1C	N-(4,6,7-trimethylquinazolin-2-yl)guanidine	0	1
Cl.NC(=N)NC=1C=CC(=CC1)C(F)(F)F	N-[4-(trifluoromethyl)phenyl]guanidine hydrochloride	0	0
NC(=N)NC1=NC=2C=CC=CC2O1	N-(1,3-benzoxazol-2-yl)guanidine	0	0
Cl.CCCC1CCN(CC1)C(=N)NC(=N)N	N-(4-propylpiperidine-1-carboximidoyl)guanidine hydrochloride	0	0
NC(=N)NC1=NC=2C=CC=CC2N1	N-(1H-1,3-benzodiazol-2-yl)guanidine	0	0
Cl.COC=1C=C(OC)C(=CC1Cl)C(=NNC(=N)N)C	N-[[1-(5-chloro-2,4-dimethoxyphenyl)ethylidene]amino]guanidine hydrochloride	0	0
Cl.CC1=NN(C(Cl)=C1C=NNC(=N)N)C=2C=C=C(C2)C(F)(F)F	N-[[5-(5-chloro-3-methyl-1-[3-(trifluoromethyl)phenyl]-1H-pyrazol-4-yl)methylidene]amino]guanidine hydrochloride	1	1
CC(=O)O.CC(=NNC(=N)N)C=1C=CC=C(C1)C(F)(F)F	N-[[1-[3-(trifluoromethyl)phenyl]ethylidene]amino]guanidine; acetic acid	0	0
Cl.NC(=N)NCC=1C=CC=CC1F	N-[(2-fluorophenyl)methyl]guanidine hydrochloride	0	0
Cl.NC(=N)NCCC=1C=CC=CC1F	N-[2-(2-fluorophenyl)ethyl]guanidine hydrochloride	0	0
CC=1NC=2C=CC=CC2C1C=NNC(=N)N	N-[[2-(2-methyl-1H-indol-3-yl)methylidene]amino]guanidine	0	0
COC=1C=CC(C=NNC(=N)N)=CC1O	N-[[3-(3-hydroxy-4-methoxyphenyl)methylidene]amino]guanidine	0	0
CC1=NN(CC=2C=CC(Cl)=CC2Cl)C(Cl)=C1C=NNC(=N)N	N-[[5-(5-chloro-1-[(2,4-dichlorophenyl)methyl]-3-methyl-1H-pyrazol-4-yl)methylidene]amino]guanidine	1	1
NC(=N)NN=C1CCCOC=2C=CC(Br)=CC12	N-[(7-bromo-2,3,4,5-tetrahydro-1-benzoxepin-5-ylidene)amino]guanidine	0	0
Cl.Cl.NC(=N)NCCCN(CC=1C=CC(=CC1)C=2C=CC=CC2)S(=O)(=O)CCCNC(=N)N	N"-[3-[N-[[1,1'-biphenyl]-4-yl]methyl]3-carbamimidamidopropanesulfonamido]propyl]guanidine dihydrochloride	0	0
I.CC(C)C(C)=1C=CC(=CC1)C(C)C(C)CNC(=N)N	N-[2-(4-tert-butylphenyl)-2-methylpropyl]guanidine hydroiodide	0	1
I.CC(C)C=1C=CC(=CC1)C2(CNC(=N)N)CCC2	N-[[1-[4-(propan-2-yl)phenyl]cyclopentyl]methyl]guanidine hydroiodide	0	1
NC(=N)NCCS(=O)(=O)N(CCNC(=N)N)CC=1C=CC(=CC1)C=2C=CC=CC2N	N"-[3-[[[1,1'-biphenyl]-4-yl]methyl](2-carbamimidamidoethyl)sulfamoyl]propyl]guanidine	0	0

I.CC(C)(C)C=1C=CC(=CC1)C2(CNC(=N)N)CC2	N-[[1-(4-tert-butylphenyl)cyclobutyl]methyl]guanidine hydroiodide	0	1
I.COC=1C=CC(=CC1)C2(CNC(=N)N)CC2	N-[[1-(4-methoxyphenyl)cyclopropyl]methyl]guanidine hydroiodide	0	0
Br.CN(CC=1C=CC=CC1)C(=O)CNC(=N)N	N-benzyl-2-carbamimidamido-N-methylacetamide hydrobromide	0	0
Br.NC(=N)NCC1=CN(N=C1C=2C=CC=CC2)C=3C=CC=CC3	N-[[1,3-diphenyl-1H-pyrazol-4-yl]methyl]guanidine hydrobromide	0	1
CC(=NNC(=N)N)C=1C=CC=2SC=3C=CC=CC3NC2C1	N-[[1-(10H-phenothiazin-2-yl)ethylidene]amino]guanidine	0	1
Br.COC(=O)C=1C=C(CNC(=N)N)OC1C	methyl 5-(carbamimidamidomethyl)-2-methylfuran-3-carboxylate hydrobromide	0	0
I.CC(C)N(C)S(=O)(=O)C=1C=CC(CNC(=N)N)=CC1	N-[[4-[methyl(propan-2-yl)sulfamoyl]phenyl]methyl]guanidine hydroiodide	0	0
I.CC(C)OC=1C=CC(CNC(=N)N)=CC1	N-[[4-(propan-2-yloxy)phenyl]methyl]guanidine hydroiodide	0	0
I.COCCOC=1C=CC=CC1CNC(=N)N	N-[[2-(2-methoxyethoxy)phenyl]methyl]guanidine hydroiodide	0	0
I.NC(=N)NCCC=1C(Cl)=CC=CC1Cl	N-[2-(2,6-dichlorophenyl)ethyl]guanidine hydroiodide	0	0
I.CC(C)N(CCNC(=N)N)C(C)C	N-[2-bis(propan-2-yl)amino]ethyl]guanidine hydroiodide	0	0
I.NC(=N)NCC(C1=CNC=2C=CC=CC12)C=3C=CC=CC3Cl	N-[2-(2-chlorophenyl)-2-(1H-indol-3-yl)ethyl]guanidine hydroiodide	0	1
I.NC(=N)NCCCS(=O)(=O)C=1C=CC=CC1	N-[3-(benzenesulfonyl)propyl]guanidine hydroiodide	0	0
I.NC(=N)NCC=1C=CC(=NC1)N2C=CC=N2	N-[[6-(1H-pyrazol-1-yl)pyridin-3-yl]methyl]guanidine hydroiodide	0	0
I.NC(=N)NC1CCN(CC=2C=CC(Cl)=CC2)CC1	N-[[1-[(4-chlorophenyl)methyl]piperidin-4-yl]methyl]guanidine hydroiodide	0	0
I.CCN(CC)C(=O)C=1C=CC(CNC(=N)N)=CC1	4-(carbamimidamidomethyl)-N,N-diethylbenzamide hydroiodide	0	0
I.CC=1C=C(Br)C=CC1NC(=O)CCNC(=N)N	N-(4-bromo-2-methylphenyl)-3-carbamimidamidopropanamide hydroiodide	0	0
I.NC(=N)NCC=1C=CC=C2C=CC=NC12	N-[(quinolin-8-yl)methyl]guanidine hydroiodide	0	0
I.COC=1C=CC(=CC1)C2CC2NC(=N)N	N-[2-(4-methoxyphenyl)cyclopropyl]guanidine hydroiodide	0	0
I.NC(=N)NCC=1C=CN=C(C1)N2CCN(CC2)C=3C=CC(F)=CC3	N-[[2-[4-(4-fluorophenyl)piperazin-1-yl]pyridin-4-yl]methyl]guanidine hydroiodide	0	0
I.NC(=N)NCC=1C=CC(CN2CCC=3C=CC=CC23)=CC1	N-[[4-[(2,3-dihydro-1H-indol-1-yl)methyl]phenyl]methyl]guanidine hydroiodide	0	1
I.CCN(CC)C(CNC(=N)N)C=1C=CC=CC1Cl	N-[2-(2-chlorophenyl)-2-(diethylamino)ethyl]guanidine hydroiodide	0	0
I.CC(C)COC=1C=CC(=CC1)C(C)(C)CNC(=N)N	N-[2-methyl-2-[4-(2-methylpropoxy)phenyl]propyl]guanidine hydroiodide	0	1
I.NC(=N)NCC1(CCCC1)SC=2C=CC=CC2	N-[[1-(phenylsulfanyl)cyclopentyl]methyl]guanidine hydroiodide	0	1
I.NC(=N)NCC=1C=CC=CC1CN2CCN(CC2)C=3C=CC=CC3	N-[[2-[(4-phenylpiperazin-1-yl)methyl]phenyl]methyl]guanidine hydroiodide	0	0
I.CC(C)C=1C=CC(=CC1)C(CNC(=N)N)NC(=O)OC(C)(C)C	tert-butyl N-(2-carbamimidamido-1-[4-(propan-2-yl)phenyl]ethyl)carbamate hydroiodide	0	0
I.NC(=N)NCC1(CCCC1)C=2C(F)=CC=CC2F	N-[[1-(2,6-difluorophenyl)cyclopentyl]methyl]guanidine hydroiodide	0	0
I.COC=1C=CC(=CC1)C2(CNC(=N)N)CCCC2	N-[[1-(4-methoxyphenyl)cyclohexyl]methyl]guanidine hydroiodide	0	0
I.NC(=N)NCCSCC=1C=CC=C2C=CC=CC12	N-(2-[[naphthalen-1-yl]methyl]sulfanyl)ethyl]guanidine hydroiodide	0	1
I.COC=1C=CC=CC1OC=2C=CC(CNC(=N)N)=CC2	N-[[4-(2-methoxyphenoxy)phenyl]methyl]guanidine hydroiodide	0	0

I.NC(=N)NCC1=CC=C(O1)C=2C=CC(Br)=CC2	N-[[5-(4-bromophenyl)furan-2-yl]methyl]guanidine hydroiodide	0	1
I.CCN(CC)C(CNC(=N)N)CC=1C=CC=CC1	N-[2-(diethylamino)-3-phenylpropyl]guanidine hydroiodide	0	1
I.NC(=N)NCC(N1CCCC1)C=2C(F)=CC=CC2C1	N-[2-(2-chloro-6-fluorophenyl)-2-(pyrrolidin-1-yl)ethyl]guanidine hydroiodide	0	0
I.NC(=N)NCC1CCC(CC1)C=2C=CC=CC2	N-[[4-(phenylcyclohexyl)methyl]guanidine hydroiodide	0	1
Br.NC(=N)NCC(O)COC=1C=CC=2OCOC2C1	N-[3-(2H-1,3-benzodioxol-5-yloxy)-2-hydroxypropyl]guanidine hydrobromide	0	0
NC(=N)NN=CC=1C=CC=CC1F	N-[[2-(2-fluorophenyl)methylidene]amino]guanidine	0	0
Cl.NC(=N)NC(=N)N1CCCC(CC=2C=CC=CC2)CC1	N-(4-benzylpiperidine-1-carboximidoyl)guanidine hydrochloride	0	0
COC=1C=CC(C=NNC(=N)N)=C(Cl)C1OC	N-[[2-(2-chloro-3,4-dimethoxyphenyl)methylidene]amino]guanidine	0	0
Cl.NC(=N)NC(=N)NCCC(=1C=CC(Cl)=CC1)N	{N}^"-[2-(4-chlorophenyl)ethyl]carbamidamido]methanimidamide hydrochloride	0	0
COC=1C=C(CNC(=N)N)C=CN1.COC=1C=C(CNC(=N)N)C=CN1.OS(=O)(=O)O	bis(N-[[2-(methoxypyridin-4-yl)methyl]guanidine]); sulfuric acid	0	0
NC(=N)NN=C1C(=O)N(CC=2C=CC=CC2Cl)C=3C=CC=CC13	N-[[1-[[2-(chlorophenyl)methyl]-2-oxo-2,3-dihydro-1H-indol-3-ylidene]amino]guanidine	0	0
CCC(=N)NCC(=N)N)C=1C=C(Cl)C=C(Cl)C1O	N-[[1-(3,5-dichloro-2-hydroxyphenyl)propylidene]amino]guanidine	0	0
Cl.COC(=O)C=1C=CC(NC(=N)N)=CC1	methyl 4-carbamimidamidobenzoate hydrochloride	0	0
NC(=N)NC=1C=CC=C(Cl)C1	N-(3-chlorophenyl)guanidine	0	0
Cl.NC(=N)NCC=1C=CC=C2C=CC=CC12	N-[[naphthalen-1-yl)methyl]guanidine hydrochloride	0	0
CCN1C(=O)C(=N)NCC(=N)N)C=2C=CC=CC12	N-[[1-ethyl-2-oxo-2,3-dihydro-1H-indol-3-ylidene]amino]guanidine	0	0
Cl.CC1=NN(C(OC=2C=CC(F)=CC2)=C1C=NC(=N)N)C=3C=CC=CC3	N-[[5-(4-fluorophenoxy)-3-methyl-1-phenyl-1H-pyrazol-4-yl]methylidene]amino]guanidine hydrochloride	0	0
I.NC(=N)NCC=1C=CC(OCC=2C=CC=CC2)=C1C	N-[[4-(benzyloxy)phenyl]methyl]guanidine hydroiodide	0	1
CCOC=1C=C(C=N)N)C=CC1OC	N-[[3-(ethoxy-4-methoxyphenyl)methylidene]amino]guanidine	0	0
Br.NC(=N)NCC=1C=CC=CC1CN2CCOCC2	N-[[2-[(morpholin-4-yl)methyl]phenyl]methyl]guanidine hydrobromide	0	0
Br.NC(=N)NCC1=NN=CN1C=2C=CC=CC2	N-[[4-(4-phenyl-4H-1,2,4-triazol-3-yl)methyl]guanidine hydrobromide	0	0
Br.NC(=N)NCCCN1CCN(CC1)C=2N=CC=CN2	N-[3-[4-(pyrimidin-2-yl)piperazin-1-yl]propyl]guanidine hydrobromide	0	0
Br.NC(=N)NCC(O)C=1C=CC(=CC1)[N+](=O)[O-]	N-[2-hydroxy-2-(4-nitrophenyl)ethyl]guanidine hydrobromide	0	0
Br.CC1=NC(CNC(=N)N)=CS1	N-[[2-methyl-1,3-thiazol-4-yl)methyl]guanidine hydrobromide	0	0
I.CCC(CC)(CNC(=N)N)NC(C)C=1C=CC=CC1	N-[[2-ethyl-2-[[1-phenylethyl]amino]butyl]guanidine hydroiodide	0	0
I.CCN(CCNC(=N)N)C=1C=CC=CC1C	N-[[2-ethyl(2-methylphenyl)amino]ethyl]guanidine hydroiodide	0	0
I.NC(=N)NCC1CCCCN1CC=2C=CC=CC2	N-[[1-(benzylpiperidin-2-yl)methyl]guanidine hydroiodide	0	0
I.NC(=N)NCC=1C=CC=C(COC2CCCC2)C1	N-[[3-[(cyclohexyloxy)methyl]phenyl]methyl]guanidine hydroiodide	0	0
I.CN1C=CN=C1SCCNC(=N)N	N-[[2-[[1-methyl-1H-imidazol-2-yl]sulfanyl]ethyl]guanidine hydroiodide	0	0
I.CC(C)(CNC(=N)N)C=1C=CC=C(C1)C(F)(F)F	N-[[2-methyl-2-[3-(trifluoromethyl)phenyl]propyl]guanidine hydroiodide	0	0
Cl.Cl.NC(=N)NCC=1C=CC(CNC(=N)N)=CC1N	N-[[4-[[4-(diaminomethylidene)amino]methyl]phenyl]methyl]guanidine dihydrochloride	0	0



I.NC(=N)NCC=1C=CC(COCC=2C=CC=CC2)=CC1	N-({4-(benzyloxy)methyl}phenyl)methylguanidine hydroiodide	0	1
CC=1C=C(C=CC1NC(=N)N)N2C=CN=C2	N-[4-(1H-imidazol-1-yl)-2-methylphenyl]guanidine	0	0
I.NC(=N)NCC=1C=CC=C(NC(=O)NC2CC2)C1	1-[3-(carbamidamidomethyl)phenyl]-3-cyclopropylurea hydroiodide	0	0
CC(=NNC(=N)N)CC1(CC2CC3CC(C2)C1)C3	N-{{1-(adamantan-1-yl)propan-2-ylidene}amino}guanidine	0	1
CC=1C=CC=2N=C(NC(=N)N)NC2C1	N-(6-methyl-1H-1,3-benzodiazol-2-yl)guanidine	0	0
Cl.NC(=N)NC=1C=CC(OC(F)(F)F)=CC1	N-[4-(trifluoromethoxy)phenyl]guanidine hydrochloride	0	0
Cl.CC1=CSC(NC(=N)N)=N1	N-(4-methyl-1,3-thiazol-2-yl)guanidine hydrochloride	0	0
NC(=N)NS(=O)(=O)C=1C=CC=CC1	N-(benzenesulfonyl)guanidine	0	0
Cl.COC=1C=CC(NC(=N)N)=CC1OC	N-(3,4-dimethoxyphenyl)guanidine hydrochloride	0	0
Br.CN(CCCNC(=N)N)CC=1C=CC=CC1	N-{3-[benzyl(methyl)amino]propyl}guanidine hydrobromide	0	0
I.CC(C)OC=1C=CC(CCC(C)NC(=N)N)=CC1	N-[4-[4-(propan-2-yloxy)phenyl]butan-2-yl]guanidine hydroiodide	0	0
I.CCC(CC)C(CNC(=N)N)N1CCCC1	N-[3-ethyl-2-(pyrrolidin-1-yl)pentyl]guanidine hydroiodide	0	0

**Table S2:** Functional enrichment of up- and downregulated proteins in *S. aureus* USA300 Lac (JE2) cells treated with various concentrations of **L15**. The enrichment terms were initially determined for protein-protein interactions with STRING<sup>151</sup> (6  $\mu$ M **L15** samples). For these samples, only proteins with a  $\log_2$ -fold enrichment ratio of  $\geq 1.2$  or  $\leq -1.2$  (with some exceptions, highlighted with two asterisks (\*\*)) and a  $-\log_{10}$  p-value of  $\geq 2$  (two sample t-test over normalized protein ratios) are depicted. To assess the influence of different compound concentrations, fold change values for the other tested **L15** concentrations are also included in this table, although not all of them reached the cut-offs for statistical significance ( $-\log_{10}$  p-value of  $\geq 2$ ) or fold change (1.5  $\mu$ M, 3  $\mu$ M:  $\geq 0.5/ \leq -0.5$ ; 4.5  $\mu$ M, 5  $\mu$ M, 5.5  $\mu$ M:  $\geq 1.2/ \leq -1.2$ ), labeled in grey. The table includes functional enrichment by biological process (BP), molecular function (MF), cellular component (CC), local network cluster (CL) (STRING), KEGG pathways<sup>176</sup>, and annotated keywords (KW) (UniProt)<sup>177,178</sup>. Proteins labeled with an asterisk (\*) were not directly included in the functional enrichment by STRING, but rather associated. Functional enrichment terms 'Fe sequestration', 'Peptide transport', and 'Hemin import' were annotated manually and not annotated by STRING. The data represent n = 4 biologically independent replicates.

Functional enrichment	UniProt ID	Gene name	Protein description	Log <sub>2</sub> fold change					
				1.5 $\mu$ M	3 $\mu$ M	4.5 $\mu$ M	5 $\mu$ M	5.5 $\mu$ M	6 $\mu$ M
<b>Upregulation</b>									
Protein folding (BP, CL)	A0A0H2XFR7	clpB	Chaperone protein ClpB	0.27	1.42	2.97	3.41	3.37	<b>3.47</b>
	Q2FGE4	dnaJ	Chaperone protein DnaJ	0.19	0.85	1.60	2.02	2.09	<b>2.31</b>
	Q2FGE2	grpE	Protein GrpE	0.28	0.89	1.76	2.09	1.95	<b>2.20</b>
	Q2FGE3	dnaK	Chaperone protein DnaK	0.05	0.61	1.45	1.76	1.67	<b>2.05</b>
	Q2FF95	groEL	Chaperonin GroEL	-0.10	0.41	1.34	1.72	1.57	<b>2.00</b>
	Q2FF94	groES	Co-chaperonin GroES	-0.38	0.64	1.09	1.82	1.49	<b>1.92</b>
	Q2FGE1	hrcA	Heat-inducible transcription repressor HrcA	0.26	0.74	1.21	1.82	1.74	<b>1.76</b>
	Q2FFQ5	prsA	Foldase protein PrsA	0.18	0.40	1.32	1.48	1.40	<b>1.38</b>
Stress response to	A0A0H2XEU5	SAUSA300_0508 (mcsA)	Excinuclease ABC subunit B	0.72	1.42	2.67	2.92	3.07	<b>3.24</b>

Cd and Co (BP, KW)	Q2FJB6	mcsB	Protein-arginine kinase	0.29	1.12	2.46	3.03	3.05	<b>3.17</b>
	Q2FJB5	clpC	ATP-dependent Clp protease ATP-binding subunit ClpC	0.40	1.12	2.54	2.85	2.91	<b>3.02</b>
	Q2FJB8	ctsR	Transcriptional regulator CtsR	0.48	1.24	2.62	2.85	2.83	<b>2.54</b>
	Q2FDV0*	copA	Copper-exporting P-type ATPase	0.21	0.63	1.40	1.28	1.19	<b>1.01**</b>
Lipid oxidation and fatty acid degradation (CL)	A0A0H2XJY2	fadE	Putative long chain fatty acid-CoA ligase VraA	0.54	1.64	2.79	3.40	3.80	<b>3.61</b>
	A0A0H2XGT7	SAUSA300_0229 (fadX)	Putative acyl-CoA transferase FadX	0.90	1.57	1.90	2.54	2.95	<b>3.42</b>
	A0A0H2XHZ4	fadD	Acyl-CoA dehydrogenase FadD	-0.21	0.97	1.20	2.19	2.40	<b>2.66</b>
	A0A0H2XFB6	SAUSA300_0226	Enoyl-CoA hydratase	0.39	1.33	1.99	2.52	2.80	<b>2.62</b>
	A0A0H2XKL6	SAUSA300_0225 (vraB)	Probable acetyl-CoA acyltransferase	0.90	1.03	1.27	2.00	2.28	<b>2.26</b>
	A0A0H2XIA4	SAUSA300_0559 (vraA)	Putative long chain fatty acid-CoA ligase VraA	0.21	0.15	0.66	1.09	1.14	<b>1.38</b>
Peptidoglycan anchor and cell wall (KW)	A0A0H2XGC9	vraR	DNA-binding response regulator	0.00	0.53	1.51	2.35	2.55	<b>3.12</b>
	A0A0H2XHE4	SAUSA300_1867	Cell wall-active antibiotics response LiaF-like C-terminal domain-containing protein	0.29	0.66	1.45	2.15	2.57	<b>3.04</b>
	A0A0H2XJC3*	vraS	Sensor protein VraS	0.28	0.53	1.79	2.36	2.63	<b>2.98</b>
	A0A0H2XHK2	clfB	Clumping factor B	0.08	0.19	1.65	1.83	1.94	<b>2.62</b>
	Q2FFM1*	mgt	Mono-functional glycosyltransferase	0.12	0.18	0.96	1.53	1.79	<b>2.08</b>
	A0A0H2XF70	SAUSA300_2581 (sasF)	Putative surface anchored protein	-0.02	0.25	1.60	1.90	1.87	<b>2.01</b>
	Q2FHV0	isdC	<b>Iron-regulated surface determinant protein C</b>	0.80	0.69	0.82	0.96	1.01	<b>1.73</b>
	A0A0H2XG16	clfA	Clumping factor A	0.17	-0.16	0.58	1.30	1.55	<b>1.68</b>



	Q2FJ77	sdrE	Serine-aspartate repeat-containing protein E	0.63	0.42	1.59	1.48	1.66	<b>1.66</b>
	Q2FJ79	sdrC	Serine-aspartate repeat-containing protein C	0.38	0.48	1.00	0.76	1.00	<b>1.54</b>
	Q2FG07	isdH	<b>Iron-regulated surface determinant protein H</b>	0.13	0.23	0.63	0.59	0.75	<b>1.37</b>
Secreted (KW)	A0A0H2XF17	ssaA	Secretory antigen SsaA	0.25	-0.09	2.37	2.63	2.73	<b>3.12</b>
	A0A0H2XHK2	clfB	Clumping factor B	0.08	0.19	1.65	1.83	1.94	<b>2.62</b>
	A0A0H2XF37	lytM	Lysostaphin	0.44	0.35	2.39	2.50	2.54	<b>2.45</b>
	A0A0H2XF70	SAUSA300_2581 (sasF)	Putative surface anchored protein	-0.02	0.25	1.60	1.90	1.87	<b>2.01</b>
	A0A0H2XE7	SAUSA300_1890 (sspP)	Staphopain A	-0.04	0.12	0.81	1.36	1.34	<b>1.97</b>
	Q2FF31	sceD	Probable transglycosylase SceD	0.54	0.60	2.70	2.63	2.61	<b>1.97</b>
	Q2FHV0	isdC	<b>Iron-regulated surface determinant protein C</b>	0.80	0.69	0.82	0.96	1.01	<b>1.73</b>
	A0A0H2XI01	SAUSA300_2579 (flgJ)	N-acetylmuramoyl-L-alanine amidase domain protein	0.25	0.22	2.31	2.74	2.33	<b>1.82</b>
	A0A0H2XG16	clfA	Clumping factor A	0.17	-0.16	0.58	1.30	1.55	<b>1.68</b>
	Q2FJ77	sdrE	Serine-aspartate repeat-containing protein E	0.63	0.42	1.59	1.48	1.66	<b>1.66</b>
	Q2FJ79	sdrC	Serine-aspartate repeat-containing protein C	0.38	0.48	1.00	0.76	1.00	<b>1.54</b>
	Q2FHS7	fliR	FPRL1 inhibitory protein	0.02	-0.02	1.79	1.71	1.96	<b>1.51</b>
	Q2FG07	isdH	<b>Iron-regulated surface determinant protein H</b>	0.13	0.23	0.63	0.59	0.75	<b>1.37</b>
Phosphate transport (KW)	Q2FH48	pstS	Phosphate-binding protein PstS	0.33	2.88	7.44	7.97	7.62	<b>7.20</b>
	A0A0H2XIK6	phoU	Phosphate-specific transport	0.19	1.29	6.21	6.65	6.31	<b>5.64</b>

			system accessory protein PhoU						
	Q2FH51	pstB	Phosphate import ATP-binding protein PstB	0.11	1.11	4.81	5.61	5.32	<b>5.32</b>
	A0A0H2XI00*	phoP	Alkaline phosphatase synthesis transcriptional regulatory protein PhoP	0.35	0.40	1.44	2.03	1.95	<b>1.42</b>
	A0A0H2XFS9*	phoR	Sensor protein kinase Walk	0.18	0.46	1.41	1.73	1.59	<b>1.27</b>
Fe sequestration	A0A0H2XF13	sbnC	Siderophore biosynthesis protein	0.58	0.44	1.23	1.52	1.95	<b>1.86</b>
	A0A0H2XG97	SAUSA300_0123 (sbnF)	Siderophore biosynthesis protein	0.37	0.28	0.83	1.10	1.33	<b>1.36</b>
	A0A0H2XHK0	sirA	Iron compound ABC transporter	0.42	0.61	1.34	1.40	1.43	<b>1.36</b>
	A0A0H2XEB0	SAUSA300_2136	Iron compound ABC transporter	0.42	0.55	1.25	1.29	1.44	<b>1.34</b>
	A0A0H2XH47	SAUSA300_0125 (sbnH)	Pyridoxal-dependent decarboxylase	0.21	0.19	0.57	0.97	1.23	<b>1.34</b>
	A0A0H2XFQ8	SAUSA300_0119 (sbnB)	Ornithine cyclo-deaminase	0.16	0.38	0.51	1.30	1.47	<b>1.26</b>
<b>Downregulation</b>									
Nitrate metabolic process (BP, CL)	A0A0H2XI54	nirD	Nitrite reductase [NAD(P)H], small subunit	-0.11	-0.86	-4.14	-5.10	-4.79	<b>-5.27</b>
	A0A0H2XHU0	nirB	Nitrite reductase [NAD(P)H], large subunit	-0.29	-0.80	-3.54	-3.50	-3.37	<b>-3.46</b>
	A0A0H2XJ07	narJ	Respiratory nitrate reductase, delta subunit	-0.21	-0.74	-2.57	-2.30	-2.23	<b>-2.44</b>
	Q2FEA5*	nreB	Oxygen sensor histidine kinase NreB	-0.18	-0.53	-2.12	-2.22	-2.28	<b>-2.23</b>
	A0A0H2XDS6	narI	Respiratory nitrate reductase, gamma subunit	-0.05	-0.60	-2.40	-2.28	-2.12	<b>-1.76</b>
	A0A0H2XJV6	narH	Respiratory nitrate reductase, beta subunit	-0.03	-0.53	-2.13	-1.79	-1.48	<b>-1.56</b>
	A0A0H2XEE7	SAUSA300_2343	Nitrate reductase (quinone)	-0.22	-0.87	-2.01	-1.56	-1.41	<b>-1.44</b>

Carotenoid biosynthetic process (BP, CL, KEGG, KW)	A0A0H2XJF9*	SAUSA300_0677	Putative deoxyribodipyrimidine photolyase	-0.12	-0.32	-1.83	-1.54	-1.98	<b>-2.19</b>
	Q2FDU6	crtN	4,4'-Diapophytoene desaturase	0.21	-0.02	-2.00	-1.80	-1.83	<b>-2.10</b>
	Q2FDU3	crtP	4,4'-Diaponeurosporene oxygenase	0.01	-0.19	-2.07	-1.75	-1.72	<b>-1.92</b>
	Q2FDU4	crtQ	4,4'-Diaponeurosporenoate glycosyltransferase	-0.08	-0.16	-2.07	-1.81	-1.80	<b>-1.77</b>
	Q2FDU5	crtM	4,4'-Diapophytoene synthase	0.06	-0.20	-1.68	-1.41	-1.35	<b>-1.59</b>
	Q2FDU2	crtO	Glycosyl-4,4'-diaponeurosporenoate acyltransferase	-0.05	-0.11	-2.47	-1.72	-1.58	<b>-1.02**</b>
Carboxylic acid and cellular amino acid catabolism (BP)	A0A0H2XHB0	SAUSA300_0177	Acyl-CoA dehydrogenase	0.14	0.04	-1.21	-1.73	-1.84	<b>-1.81</b>
	Q2FKP8	hutH	Histidine ammonia-lyase	0.11	0.30	-1.48	-1.76	-1.82	<b>-1.66</b>
	Q2FEG6	hutI	Imidazolone-propionase	0.12	0.22	-1.50	-1.98	-1.87	<b>-1.66</b>
	Q2FJU9	nanA	N-acetylneuraminate lyase	-0.21	-0.08	-1.63	-1.46	-1.48	<b>-1.57</b>
	Q2FG29	ald2	Alanine dehydrogenase 2	-0.13	-0.06	-1.26	-1.15	-1.32	<b>-1.52</b>
	A0A0H2XHP8	putA	Proline dehydrogenase	-0.30	-0.11	-2.18	-1.63	-1.51	<b>-1.51</b>
	A0A0H2XDW3	hutU	Urocanate hydratase	0.02	0.17	-1.62	-1.72	-1.58	<b>-1.13**</b>
	A0A0H2XHC2	gudB	Glutamate dehydrogenase	-0.05	0.01	-1.23	-1.07	-1.03	<b>-0.99**</b>
Phosphoenolpyruvate (PEP)-dependent sugar phosphotransferase system (BP, CL)	A0A0H2XH10	SAUSA300_0331	Uncharacterized protein	0.05	-0.45	-2.91	-4.51	-4.52	<b>-5.33</b>
	A0A0H2XGP6	mtlA	Mannitol-specific phosphotransferase enzyme IIA component	-0.09	-0.27	-2.74	-2.43	-2.18	<b>-3.71</b>
	A0A0H2XI57	SAUSA300_2106	Putative transcriptional regulator	0.00	-0.10	-1.68	-1.26	-1.42	<b>-2.67</b>
	A0A0H2XI15	SAUSA300_2576	Phosphotransferase system, fructose-specific IIBC component	0.30	-0.00	-0.95	-2.10	-1.93	<b>-2.44</b>
	A0A0H2XGD3	SAUSA300_0330 (sgaT)	Ascorbate-specific PTS system EIIC component	0.07	-0.53	-2.43	-2.81	-2.47	<b>-2.27</b>

	A0A0H2XDH0	glvC	PTS system, arbutin-like IIBC component	-0.01	-0.22	-1.19	-1.77	-1.88	<b>-2.04</b>
	A0A0H2XI14	SAUSA300_2575	Transcriptional antiterminator	0.29	0.11	-1.14	-1.90	-1.89	<b>-2.03</b>
	A0A0H2XK78	SAUSA300_0208	Putative maltose ABC transporter	0.20	-0.06	-0.74	-1.49	-1.77	<b>-1.89</b>
	A0A0H2XIE4	pfoR	Perfringolysin O regulator protein	-0.90	-0.50	-2.61	-2.04	-2.40	<b>-1.67</b>
	A0A0H2XHA7	SAUSA300_1809	Putative membrane protein	-0.79	-0.62	-2.51	-1.69	-2.12	<b>-1.29</b>
Trans-membrane transport (BP, MF)	A0A0H2XE61	SAUSA300_2399	ABC transporter	0.08	0.09	-1.98	-2.04	-2.16	<b>-3.17</b>
	A0A0H2XGF4	SAUSA300_0308 (tcyP)	L-cystine uptake protein TcyP	0.44	0.22	-1.50	-2.01	-2.08	<b>-1.83</b>
	Q2FFH9	sdsC	Sodium-dependent dicarboxylate transporter SdcS	-1.75	-0.94	-2.20	-2.22	-2.39	<b>-1.79</b>
	A0A0H2XKL1	glpT	Glycerol-3-phosphate transporter	-0.35	-0.25	-1.95	-2.05	-2.03	<b>-1.69</b>
	A0A0H2XJ46	SAUSA300_0314	Sodium:solute symporter family protein	-0.13	-0.01	-1.82	-1.79	-1.80	<b>-1.52</b>
	A0A0H2XEN8	lctP	L-lactate permease	-0.57	-0.57	-2.00	-1.88	-1.87	<b>-1.40</b>
	Q2FII2	metN2	Methionine import ATP-binding protein MetN 2	0.20	-0.07	-1.39	-1.45	-1.36	<b>-1.34</b>
	A0A0H2XGA6	SAUSA300_2313	L-lactate permease	-0.64	-1.07	-2.63	-2.08	-1.83	<b>-1.32</b>
	Q2FFJ3	putP	Sodium/proline symporter	-0.02	-0.29	-1.81	-1.80	-1.27	<b>-0.94**</b>
Peptide transport	A0A0H2XFS6	SAUSA300_0979	Thiamine ABC transporter permease	-0.66	-0.30	-2.48	-2.79	-2.79	<b>-2.78</b>
	A0A0H2XI71	SAUSA300_0200	Peptide ABC transporter	0.33	0.28	-0.93	-2.47	-2.31	<b>-2.44</b>
	A0A0H2XIJ9	SAUSA300_0978	ABC transporter	0.31	0.34	-1.10	-1.59	-1.61	<b>-1.81</b>
	A0A0H2XJ57	oppF	Oligopeptide ABC transporter	0.35	0.00	-1.38	-1.41	-1.47	<b>-1.75</b>
	A0A0H2XJ10	oppD	Oligopeptide ABC transporter	0.22	-0.02	-1.32	-1.55	-1.66	<b>-1.71</b>
	A0A0H2XK20	SAUSA300_0977	Cobalt transport family protein	0.54	0.36	-0.84	-1.42	-1.58	<b>-1.67</b>
	A0A0H2XID7	oppB	Oligopeptide ABC transporter	0.20	-0.14	-1.20	-1.48	-1.31	<b>-1.63</b>
	A0A0H2XEU4	oppC	Oligopeptide ABC transporter	0.15	-0.10	-1.45	-1.60	-1.49	<b>-1.50</b>
	A0A0H2XHT0	SAUSA300_2453	ABC transporter	0.12	0.16	-0.60	-1.01	-1.31	<b>-1.50</b>

	Q2FI12	metN2	Methionine import ATP-binding protein MetN 2	0.20	-0.07	-1.39	-1.45	-1.36	<b>-1.34</b>
Hemin import	Q2FED6	hrtB	Putative hemin transport system permease protein HrtB	0.05	0.57	-1.09	-1.34	-2.06	<b>-4.59</b>
	Q2FED7	hrtA	Putative hemin import ATP-binding protein HrtA	0.85	1.06	-0.46	-1.26	-1.81	<b>-3.65</b>
	A0A0H2XJF7	SAUSA300_2398	Putative membrane protein	-0.40	-0.65	-2.93	-2.92	-3.09	<b>-3.63</b>
	A0A0H2XE61	SAUSA300_2399	ABC transporter	0.08	0.09	-1.98	-2.04	-2.16	<b>-3.17</b>
	A0A0H2XI53	SAUSA300_2557	ABC transporter protein	-0.52	-0.42	-1.14	-1.60	-1.42	<b>-1.90</b>
	A0A0H2XFY2	SAUSA300_0271	ABC transporter	0.10	-0.31	-2.39	-1.60	-1.84	<b>-1.47</b>
	A0A0H2XG18	SAUSA300_0309	Putative hemin import ATP-binding protein HrtA	-0.68	-0.59	-2.00	-1.59	-1.86	<b>-1.10**</b>
	A0A0H2XFR0	SAUSA300_0272	ABC-2 type transporter transmembrane domain-containing protein	0.07	-0.55	-1.37	-1.56	-1.56	<b>-1.06**</b>
4Fe-4S cluster binding (BP, KW)	A0A0H2XI54	nirD	Nitrite reductase [NAD(P)H], small subunit	-0.11	-0.86	-4.14	-5.10	-4.79	<b>-5.27</b>
	Q2FK43	pflA	Pyruvate formate-lyase-activating enzyme	0.07	-0.62	-2.26	-3.32	-3.60	<b>-4.83</b>
	A0A0H2XHU0	nirB	Nitrite reductase [NAD(P)H], large subunit	-0.29	-0.80	-3.54	-3.50	-3.37	<b>-3.46</b>
	A0A0H2XFV6	queG	Epoxy-queuosine reductase	0.08	-0.06	-1.69	-2.27	-2.30	<b>-3.41</b>
	Q2FEI5	SAUSA300_2258	Putative formate dehydrogenase	0.03	-0.08	-1.87	-2.09	-2.26	<b>-3.29</b>
	A0A0H2XH15	SAUSA300_1858	Radical SAM core domain-containing protein	0.47	-0.02	-1.27	-1.75	-1.77	<b>-2.31</b>
	Q2FEA5	nreB	Oxygen sensor histidine kinase NreB	-0.18	-0.53	-2.12	-2.22	-2.28	<b>-2.23</b>
	A0A0H2XIP6	queH	Epoxy-queuosine reductase QueH	0.35	0.16	-0.28	-0.96	-1.21	<b>-2.08</b>
	Q2FHM0	rlmN	Probable dual-specificity	0.01	0.14	-0.81	-1.17	-1.42	<b>-1.91</b>

			RNA methyltransferase RlmN						
A0A0H2XH44	mutY		Adenine DNA glycosylase	0.11	-0.10	-1.11	-1.34	-1.37	<b>-1.85</b>
Q2FIE9	lipA		Lipoyl synthase	0.04	-0.04	-0.85	-1.19	-1.42	<b>-1.79</b>
A0A0H2XEL8	SAUSA300_1536		tRNA (N(6)-L-threonyl-carbamoyl-adenosine(37)-C(2))-methylthio-transferase	0.37	0.31	-0.19	-0.70	-0.92	<b>-1.68</b>
A0A0H2XIJ0	sdaAA		L-serine dehydratase	0.24	-0.06	-0.83	-1.45	-1.42	<b>-1.62</b>
A0A0H2XEE7	SAUSA300_2343		Nitrate reductase (quinone)	-0.22	-0.87	-2.01	-1.56	-1.41	<b>-1.44</b>
Q2FEM4	moaA		GTP 3',8-cyclase	0.02	-0.08	-1.14	-1.09	-1.11	<b>-1.44</b>
Q2FHE6	miaB		tRNA-2-methylthio-N(6)-dimethylallyl-adenosine synthase	0.12	-0.02	0.20	-0.03	-0.31	<b>-1.21</b>

## 4. Methods

Information about data and code availability, MD simulations as well as chemical synthesis and analysis are not included in this thesis. Detailed information on this can be found in the original publication. Information about biological samples and experimental procedures were all adapted from a previous study<sup>66</sup> and are included in this section.

Room temperature (RT) is defined as 22 – 25 °C.

### 4.1. HTS Guanidinium Library and Screen

*Stuart Ruddell, Kenji Schorpp, and Kamyar Hadian* helped with the library design.

All guanidinium compounds were commercially purchased from *Enamine Ltd*. The designed guanidinium library comprised 246 compounds. The library was first screened in *E. coli* K12 by *Kenji Schorpp* in a 384-well format at 100 µM compound concentration using either LB medium alone or LB medium with 25 mM NaHCO<sub>3</sub> added. Susceptibility to each compound was evaluated by measuring the optical density at 600 nm.

### 4.2. Chemical Compounds

**PK150** ((4-Chloro-3-(trifluoromethyl)phenyl)-3-(2,2-difluorobenzo[d][1,3]dioxol-5-yl)urea) was previously synthesized following a published procedure<sup>42</sup>. Dr. *Stephan Hacker* (Leiden University) generously supplied the heavy and light isoDTB tags<sup>169</sup>. All other chemical compounds used in this study were either synthesized as previously published<sup>66</sup> or obtained commercially from *Enamine Ltd* and were used without further purification.

### 4.3. Cell Culture

Cell culture media and supplements were sourced from *Sigma Life Science* and *Life Technologies*. HeLa cells were grown in *Dulbecco's Modified Eagle Medium* (DMEM) with high glucose (4.5 g/L), supplemented with 10% fetal bovine serum (FBS) and 2 mM L-glutamine. The cells were kept at 37 °C in a humidified atmosphere with 5% CO<sub>2</sub> and were detached using trypsin-EDTA.

### 4.4. Bacterial Strains

Available strains were obtained from the following suppliers: *Horizon Discovery Ltd*, UK (*E. coli* Keio Knockout: *E. coli* parent strain BW25113 (OEC5042), *E. coli* BW25113 ΔToIC JW5503 (OEC4987-213607439) and *E. coli* BW25113 ΔBamB JW2496 (OEC4987-200827790)), *Institute Pasteur*, France (*L. monocytogenes* EGD-e, *P. aeruginosa* PAO1), *American Type Culture Collection ATCC*, USA (*E. faecalis* V583/ATCC 700802, *S. aureus* USA300 Lac

JE(2)), Deutsche Sammlung von Mikroorganismen und Zellkulturen DSMZ, Germany (*A. baumannii* DSM 30007, *E. cloacae subsp. cloacae* DSM 30054, *E. faecium* DSM 20477, *E. faecium* DSM 17050, *K. pneumoniae* DSM 30104). Dr. Guisepppe Magistro (Department of Urology, Hospital of the Ludwig-Maximilians-Universität München, Germany) generously provided *E. coli* CFT073. The Network on Antimicrobial Resistance in *Staphylococcus aureus* (NARSA; Medical Center, University of Nebraska, USA) kindly provided the Nebraska Transposon Mutant Library<sup>149</sup>. The Chair of Organic Chemistry II (TUM) provided the following strains: *E. coli* K12, *E. coli* 536, *E. coli* BL21(DE3) and pLysS strains, and *S. enterica* serovar enteritidis.

For the cultivation of bacteria, the following media were used: All *E. coli* strains, *P. aeruginosa*, and *E. faecium* DSM 20477 were cultured in LB medium (Lysogeny broth, 10 g/L casein peptone, 5 g/L NaCl, 5 g/L yeast extract, pH 7.5). For *E. coli* BL21(DE3) and BL21(DE3) pLysS strains, the respective antibiotics were added to the culture. *L. monocytogenes*, *K. pneumoniae*, *A. baumannii*, *E. cloacae*, *E. faecalis*, *E. faecium* DSM 17050, and *S. enterica* were cultured in BHI medium (Brain heart infusion, 7.5 g/L brain infusion, 10 g/L heart infusion, 10 g/L casein peptone, 5 g/L NaCl, 2.5 g/L Na<sub>2</sub>HPO<sub>4</sub>, 2 g/L glucose, pH 7.4). All used *S. aureus* strains were cultured in B medium (Broth with 0.1% K<sub>2</sub>HPO<sub>4</sub>, 10 g/L casein peptone, 5 g/L NaCl, 5 g/L yeast extract, 1 g/L K<sub>2</sub>HPO<sub>4</sub>, pH 7.5). The addition of 25 mM NaHCO<sub>3</sub> to the media leads to a change in the pH to 8.0.

#### 4.5. Plasmids

Plasmids and their characteristics, used in subsequent sections for methods such as protein purification of MBP-tagged SpsB, and generation of *E. coli* membranes containing full-length SpsB (both wild-type and mutants), are detailed in a previous study<sup>163</sup>.

#### 4.6. Minimum Inhibitory Concentration Assay

Antibacterial activity against various bacteria was assessed using the minimum inhibitory concentration assay through the broth microdilution method in 96-well plates (Transparent Nunc 96-well flat bottom, *Thermo Fisher Scientific*). The bacterial inoculum used was 5x10<sup>5</sup> CFU/mL. Briefly, a 0.5 MacFarland of bacterial overnight culture was diluted 100-fold in a fresh medium containing 50 mM NaHCO<sub>3</sub>. Each 96-well plate was prepared by adding 50 µL of the cell suspension to wells containing 50 µL of serially diluted concentrations of each compound, supplemented with 2% DMSO (resulting in a final DMSO concentration of 1%). A negative control with no compound was also included (growth control). After 24 h of incubation at 37 °C and 200 rpm, microbial growth was analyzed by assessing turbidity. The optical density was measured at 600 nm using an Infinite™ M Nano Tecan 200Pro plate reader. MIC values were defined as the lowest compound concentration at which no bacterial growth was



visually detected. Each experiment was performed in  $n = 3$  biologically independent replicates per compound and concentration, and each biological replicate included three technical replicates.

#### 4.7. Hemolysis Assay in Sheep Blood

Hemolytic activity and potential effects on the cell membrane were evaluated in sheep blood using a liquid hemolysis assay conducted in 96-well plates (Transparent Nunc 96-well flat bottom, *Thermo Fisher Scientific*). 5 mL of sheep blood (100%) were washed three times with 10 mL of cold PBS for 5 min at 500 x g and RT, then diluted to 3.1% with cold PBS and 32.25 mM NaHCO<sub>3</sub>. Each well of the 96-well plate was carefully filled with 80  $\mu$ L of this dilution, followed by the addition of 20  $\mu$ L of each compound, resulting in a final erythrocyte concentration of 2.5%. A positive control of 0.5% Triton X-100 was used. After incubating for 30 min at 37 °C and 5% CO<sub>2</sub>, the cells were centrifuged for 10 min at 500 x g and RT. 50  $\mu$ L of the supernatant was carefully transferred into a new 96-well plate. The optical density was measured at 540 nm using an Infinite™ M Nano Tecan 200Pro plate reader. Each experiment included  $n = 3$  biologically independent replicates per compound and concentration, with three technical replicates each. Hemolytic activity was baseline-corrected with the lowest compound concentration before normalizing to Triton X-100.

#### 4.8. Human Metabolic Activity Assay

Cytotoxicity in human epithelial HeLa cells was evaluated using the MTT assay in 96-well plates (Transparent Nunc 96-well flat bottom, *Thermo Fisher Scientific*). Each well was seeded with 4000 HeLa cells in DMEM high glucose containing 10% FBS and 2 mM L-glutamine and incubated for 24 h at 37 °C and 5% CO<sub>2</sub>. The medium was then replaced with 100  $\mu$ L of fresh DMEM containing various concentrations of the compounds, ranging from 0.39  $\mu$ M to 100  $\mu$ M, or DMSO as a control (1% final DMSO concentration). After 24 h of incubation, 20  $\mu$ L of MTT solution (3-(4,5-dimethyl-2-thiazolyl)-2,5-diphenyltetrazolium bromide, 5 mg/mL in PBS) was added to each well, and the cells were incubated for an additional 2 h. The supernatant was then removed, and the formazan crystals were dissolved in 200  $\mu$ L DMSO. Optical density was measured at an excitation wavelength of 570 nm and an emission wavelength of 630 nm (background) using an Infinite™ M Nano Tecan 200Pro plate reader. Each experiment included  $n = 3$  biologically independent replicates per compound and concentration, with three technical replicates each. To calculate IC<sub>50</sub> values (the concentration at which 50% cell viability is achieved), background absorbance was subtracted, and each value was baseline-corrected with the highest compound concentration before normalization to the DMSO control. Data were fitted using a log(inhibitor) versus response variable slope (four parameters) non-linear regression model with *GraphPad Prism* 10.01.

#### 4.9. Membrane Depolarization Assay

The protocol was adapted from a published procedure<sup>138</sup>. Overnight cultures of *S. aureus* USA300 Lac (JE2) were diluted to an OD<sub>600</sub> of 0.05 in 20 mL of medium containing 25 mM NaHCO<sub>3</sub>. The cells were grown to the early exponential phase, reaching an OD<sub>600</sub> of 0.5, then adjusted to an OD<sub>600</sub> of 0.3 in 5 mM HEPES supplemented with 20 mM glucose and 25 mM NaHCO<sub>3</sub>. Fluorescence measurements were taken at an excitation wavelength of 610 nm and an emission wavelength of 660 nm using an Infinite™ M Nano Tecan 200Pro plate reader for 3 min following the addition of the fluorescence membrane potential-sensitive dye 3,3'-dipropylthiadicarbocyanine iodide at a final concentration of 1 μM. The dye was incubated, and measurements continued for an additional 15 min to reach equilibrium. Next, compounds at concentrations of 1.5 μM, 3 μM, 6 μM, and 12 μM, or DMSO as a control (1% final DMSO concentration), were added, and fluorescence was recorded for 1 h. Gramicidin (1 μM) was used as a positive control. Each experiment included n = 3 biologically independent replicates per compound and concentration, with three technical replicates each. Additionally, the same measurements were performed without any bacterial cells to assess the possible quenching effects of the compounds.

#### 4.10. Electron Microscopy Experiments

Electron microscopy was performed by *Mathias Müssen* with slight modifications to a previously published method<sup>42</sup>.

Overnight cultures of *S. aureus* USA300 Lac (JE2) were used to inoculate 10 mL of B medium with 25 mM NaHCO<sub>3</sub> to an OD<sub>600</sub> of 0.05 for each tested condition. The cells were grown at 200 rpm and 37 °C until reaching an OD<sub>600</sub> of 0.5, then treated with the compound (1% final DMSO concentration). DMSO was used as a control. After incubation for either 3 or 8 h, the treatment was stopped by adding 2 mL of 25% formaldehyde (resulting in a 5% final concentration) and 0.8 mL of 25% glutaraldehyde (resulting in a 2% final concentration) to 7.2 mL of the cell suspension. For scanning electron microscopy, samples were washed in TE buffer and dehydrated through a graded series of acetone. Critical point drying was performed using an automated CPD300 (*Leica Microsystems*) before coating samples with gold/palladium in a sputter coater SCD 500 (*Bal-Tec*). Images were acquired at an acceleration voltage of 5 kV using the field emission scanning electron microscope Merlin (*Zeiss*) with both the Everhart Thornley HESE2-detector and the in-lens SE-detector. For transmission electron microscopy, samples were treated with 1% osmium tetroxide in TE buffer for 1 h at RT following aldehyde fixation. After washing, samples were dehydrated through a graded series of EtOH, including an incubation step with 2% uranyl acetate at 70% EtOH. Samples were then infiltrated with LR White resin in a series of ratios (1:1, 2:1, 100% LR White/EtOH) and

polymerized at 55 °C for two days. Ultrathin sections, approximately 60 nm thick, were cut using a diamond knife on an Ultramicrotome Ultracut (*Reichert/Leica*) and counterstained with 4% aqueous uranyl acetate. Images were acquired using the transmission electron microscope Libra 120 (*Zeiss*) at an acceleration voltage of 120 kV and calibrated magnifications. EM experiments were performed in n = 2 biologically independent experiments per condition.

#### 4.11. Time-Kill Assay

Time-kill experiments were conducted as described in previous studies<sup>179</sup>. An overnight culture of *S. aureus* USA300 Lac (JE2) was diluted to a final OD<sub>600</sub> of 0.05 in B medium containing 25 mM NaHCO<sub>3</sub>. The cells were grown until they reached an OD<sub>600</sub> of 0.5 (early exponential phase). They were then further diluted to 1x10<sup>6</sup> CFU/mL in culture tubes containing 5 mL of B medium with 25 mM NaHCO<sub>3</sub>. The compound was added at concentrations of 1.5 μM, 3 μM, 6 μM, and 12 μM, with DMSO as a control (1% final DMSO concentration). The cultures were incubated at 200 rpm and 37 °C. At specified time points (1 h, 2 h, 4 h, 6 h, 8 h, and 24 h), serial dilutions of each sample were plated on agar plates with 25 mM NaHCO<sub>3</sub> for CFU calculation. These experiments were performed in n = 2 biologically independent replicates per concentration, each with four technical replicates.

#### 4.12. Minimum Bactericidal Concentration

The minimum bactericidal concentration was determined based on the MIC assay. Initially, the MIC was established using the standard MIC assay. For MBC calculation, CFUs were measured from the previously prepared MIC plate for the following conditions: (a) the growth control (without compound), (b) the MIC concentration, and (c) the next two higher concentrations of the compound. Each 10 μL of the respective serially diluted samples was plated on agar plates with 25 mM NaHCO<sub>3</sub>. The MBC is defined as the lowest concentration that results in a reduction of more than 99.9% of the initial inoculum's viability (a 3-fold log<sub>10</sub> reduction). The MBC was determined using n = 3 biologically independent replicates, each including three technical replicates.

#### 4.13. Frequency of Resistance Assay

Spontaneous **L15**-resistant mutants were generated using a frequency of resistance assay with a large inoculum approach<sup>98,180</sup>. An overnight culture of *S. aureus* USA300 Lac (JE2) grown in B medium with 25 mM NaHCO<sub>3</sub> was diluted to an OD<sub>600</sub> of 200. From this suspension, 10 μL was plated on agar plates with 25 mM NaHCO<sub>3</sub> containing 6 μM of **L15** or DMSO as a control (1% final DMSO concentration). To calculate the CFU/mL, serial dilutions of the same cell suspension were also plated on agar plates. After incubating for 24 h at 37 °C, colonies were counted. The FoR was calculated by dividing the number of resistant colonies on the

**L15**-containing agar plates by the CFU of the initial cell inoculum. FoR values were determined using  $n = 2$  biologically independent replicates.

#### 4.14. Growth Curves Experiments

*S. aureus* USA300 Lac (JE2) overnight cultures were inoculated to an  $OD_{600}$  of 0.06 in 5 mL B medium supplemented with various compound concentrations (1.5  $\mu$ M, 3  $\mu$ M, 3.5  $\mu$ M, 4  $\mu$ M, 4.5  $\mu$ M, 5  $\mu$ M, 5.5  $\mu$ M, and 6  $\mu$ M) or DMSO as a control (1% final DMSO concentration) and 25 mM  $NaHCO_3$ . The cells were grown for 8 h at 200 rpm and 37 °C. The  $OD_{600}$  was measured every 2 h within the first 4 h, followed by every 1 h. Growth curves were generated by plotting the measured  $OD_{600}$  values over time. The experiment was conducted with three technical replicates for each concentration in  $n = 2$  biologically independent experiments.

#### 4.15. Bacterial Genomics (Sequencing of FoR mutants)

Genomic sequencing was performed by *Howard Junca*.

*S. aureus* USA300 Lac containing plasmids pUSA01 and pUSA02, the plasmid-free derivative *S. aureus* USA300 Lac (JE2), and **L15**-resistant mutants from three replicates of FoR assays were subjected to total DNA extraction using the FastDNA Spin Kit for Soil (*MP Biomedicals*) according to the manufacturer's instructions. DNA libraries were prepared using the NEBNext® Ultra™ II FS DNA Library Prep Kit (*New England Biolabs*) without fragment size selection and sequenced on an Illumina MiSeq sequencer using a 300-bp paired-end protocol, resulting in an average of 1.2 million reads. Paired reads were merged by overlap using jgi.BBmerged (Version 38.84)<sup>181</sup>. The most closely related genome was identified through BlastN searches against the RefSeq genome database (Release 221, 6 November 2023) using *de novo* generated contigs by SPAdes<sup>182</sup>. The two closest nearly identical reference genomes in all cases were the USA300 genomes with accession numbers CP000255 and CP020619. Plasmids pUSA01 and pUSA02 (CP000256 and CP000257) were also identified accordingly. To detect all single nucleotide polymorphisms, the merged read datasets were mapped to the reference chromosome CP000255 using Geneious Prime Mapper (Geneious Prime 2023.1.1, <https://www.geneious.com>) with medium sensitivity and five iterations. A single SNP altering C to T at position 755513, changing the codon TCA to TTA, was identified in all FoR mutants, resulting in an amino acid change from S to L at position 366 in the 'quinolone-resistant protein NorA' (UniProt ID: A0A0H2XGK0, protein SAUSA300\_0680). This gene is highly conserved and part of the core genome defined for reference strains of *S. aureus*. The mutation is not found in any reference NorA proteins of *S. aureus* strains. Raw sequence datasets of evolved **L15**-resistant mutants and the initial wild-type strains of USA300 LAC used in the experiment are available in the SRA archive under NCBI BioProject number PRJNA1103407. Strains for

sequencing were recovered from different stocks of the USA300 strain and labeled as either old or new. Sequencing experiments were conducted in two independent experiments with  $n = 3$  biologically independent replicates each.

#### 4.16. Gel-based Fluorescent Labeling

For each biological replicate, a 1:100 dilution of *S. aureus* USA300 Lac (JE2) overnight cultures was prepared in 25 mL of B medium supplemented with 25 mM NaHCO<sub>3</sub>. The cells were grown for 10 h at 200 rpm and 37 °C, and the OD<sub>600</sub> was adjusted to 40 using sterile PBS. For each labeling condition (A/BPP: 3 μM **L15-P**, 6 μM **L15-P**, and DMSO; competitive A/BPP: 3 μM **L15-P** and 30 μM **L15**), 200 μL of cell suspension was transferred to an Eppendorf tube and treated with the respective compounds (1% final DMSO concentration). The treatment lasted for 30 min. After treatment, the cells were transferred to a 12-well tissue culture plate (Transparent 12-well, flat bottom, *Avantor VWR*) and UV-irradiated (FL8BL-B lamps, *Hitachi*) for 5 min while cooling. Non-UV samples underwent the same procedure without UV exposure. The cells were then transferred to Protein LoBind tubes (*Eppendorf*), centrifuged for 5 min at 6,000 x g and 4 °C, and the pellets were washed twice with 500 μL PBS. Enzymatic lysis was performed using 200 μL PBS supplemented with 0.05 mg/mL lysostaphin (*Sigma Life Science*) for 30 min at 1,000 rpm and 37 °C. Next, 4 μL of 20% SDS (0.4% final concentration) was added to each sample, followed by sonication for 10 s at 20% intensity (Sonopuls HD 2070 ultrasonic rod, *Bandelin electronic GmbH*). The lysate was cleared by centrifugation for at least 30 min at 21,000 x g and RT, and the supernatant was transferred to new LoBind tubes. The protein concentration of each sample was determined using the bicinchoninic acid (BCA) assay (Roti Quant, *Roth*) and adjusted to 2 mg/mL. A click mix solution was prepared by combining 1 μL of 10 mM rhodamine azide in DMSO, 3 μL of 1.67 mM tris(benzyltriazolymethyl)amine (TBTA) in a mixture of 80% tBuOH and 20% DMSO, 1 μL of 50 mM CuSO<sub>4</sub> in H<sub>2</sub>O, and 1 μL of 100 mM tris(2-carboxyethyl)phosphine (TCEP) in H<sub>2</sub>O. For each protein sample, 50 μL was transferred to individual Eppendorf tubes and mixed with 7 μL of the click mix solution. The samples were incubated for 60 min at RT. Proteins were precipitated by adding 500 μL ice-cold acetone and incubating for at least 2 h at -20 °C. After incubation, the proteins were pelleted by centrifugation for 10 min at 13,000 x g and 4 °C, and the resulting pellet was washed twice with 500 μL ice-cold MeOH *via* mild sonication for 10 s at 10% intensity (Sonopuls HD 2070 ultrasonic rod, *Bandelin electronic GmbH*). The supernatant was removed, and the protein pellets were air-dried for 10 min. The dried pellets were dissolved in Laemmli buffer by sonication for 10 s at 10% intensity. These samples were then subjected to SDS-PAGE using 15% polyacrylamide gels. Fluorescence was recorded with a *Fujifilm* Las-4000 Luminescent Image Analyzer equipped with a Fujinon VRF43LMD3 lens

and a 575DF20 filter. Coomassie staining of the gels was performed as a loading control. Gel-based labeling was conducted in n = 3 biologically independent experiments per condition.

#### 4.17. Preparative Labeling for LC-MS/MS Analysis

##### Labeling, Lysis, and Click.

For each biological replicate, a 1:100 dilution of *S. aureus* USA300 Lac (JE2) overnight cultures was prepared in 25 mL of B medium with 25 mM NaHCO<sub>3</sub>. The cells were grown for 10 h at 200 rpm and 37 °C, and the OD<sub>600</sub> was adjusted to 40 using sterile PBS. For each labeling condition (A/BPP: 3 μM **L15-P**, 6 μM **L15-P**, and DMSO; competitive A/BPP: 3 μM **L15-P** and 30 μM **L15**), 200 μL of the cell suspension was transferred to an Eppendorf tube and treated with the respective compounds (1% final DMSO concentration) for 30 min. After treatment, the cells were transferred to a 12-well tissue culture plate (Transparent, flat bottom, *Avantor VWR*) and UV-irradiated (FL8BL-B lamps, *Hitachi*) for 5 min while cooling. Non-UV samples followed the same procedure without UV exposure. After photo-crosslinking, the cells were transferred to Protein LoBind tubes (*Eppendorf*), centrifuged for 5 min at 6,000 x g and 4 °C, and washed twice with 500 μL PBS. Enzymatic lysis was performed with 200 μL PBS containing 0.05 mg/mL lysostaphin (*Sigma Life Science*) for 30 min at 1,000 rpm and 37 °C. Next, 4 μL of 20% SDS (0.4% final concentration) was added to each sample, followed by sonication for 10 s at 20% intensity (Sonopuls HD 2070 ultrasonic rod, *Bandelin electronic GmbH*). The lysate was cleared by centrifugation for at least 30 min at 21,000 x g and RT, and the supernatant was transferred to new LoBind tubes. Protein concentration for each sample was determined using the BCA assay (Roti Quant, *Roth*), and 45 μL of each protein sample (2.23 mg/mL) was transferred to a 96-well plate (Polypropylene, V-bottom, *Greiner* cat. 651201). A click mix solution was prepared by combining 0.6 μL of 20 mM biotin azide in DMSO, 2.5 μL of 1.67 mM TBTA in a mixture of 80% tBuOH and 20% DMSO, 1.2 μL of 50 mM CuSO<sub>4</sub> in H<sub>2</sub>O, and 0.6 μL of 100 mM TCEP in H<sub>2</sub>O. To each protein sample, 4.9 μL of the click mix solution was added, and the plate was incubated for 90 min at 950 rpm and RT. The reaction was quenched by adding 65 μL of 8 M urea in H<sub>2</sub>O with 10 mM TCEP and 20 mM iodoacetamide (IAA) for 15 min at 950 rpm and RT. The excess IAA was then quenched by adding 2 μL of 500 mM dithiothreitol (DTT) per sample.

##### Enrichment and Digestion.

All reagents used were of LC-MS grade. Sample processing adhered to an adapted protocol for magnetic bead enrichment<sup>122</sup>. To each sample, 10 μL of a 2-fold concentrated 1:1 mix of washed (3x with H<sub>2</sub>O) hydrophobic and hydrophilic carboxylate-coated magnetic beads (*Cytiva*, cat# 65152105050250 and 45152105050250) was added. This was followed by the



addition of 175  $\mu\text{L}$  EtOH to precipitate the proteins onto the beads. The subsequent steps were carried out using an automated liquid handling system (Hamilton Microlab Prep, *Hamilton*). The plate was incubated for 5 min at 500 rpm and RT before being washed. Each washing step utilized a 96-well ring magnet (Alpaqua, *Magnum FLX*). The plate was placed on the magnet, and the supernatant was removed slowly (20  $\mu\text{L/s}$ ) to avoid losing any beads. Washing involved removing the plate from the magnet, adding the respective washing solution, and shaking for 1 min at 800 rpm and RT. The samples were washed three times with 180  $\mu\text{L}$  of 80% EtOH and once with 180  $\mu\text{L}$  acetonitrile. Proteins were eluted from the beads by adding 75  $\mu\text{L}$  of 0.2% SDS in PBS, followed by 5 min of incubation at 800 rpm and 40  $^{\circ}\text{C}$ . The plate was placed back on the magnet to transfer the supernatant into new wells. This elution step was repeated, resulting in a total volume of 150  $\mu\text{L}$  eluted proteins. Next, 50  $\mu\text{L}$  of washed (3x with 0.2% SDS in PBS) streptavidin magnetic beads (*New England Biolabs*, cat# S1420S) were added to each well containing the eluted protein samples. The plate was sealed and incubated for 1 h at 800 rpm and RT in a plate shaker with a heated lid (ThermoMixer C, *Eppendorf*) to allow the labeled proteins to bind to the streptavidin beads. After incubation, the plate was further processed with the liquid handling system. The beads were washed three times with 180  $\mu\text{L}$  of 0.1% NP-40 in PBS, twice with 180  $\mu\text{L}$  of 6 M urea, and three times with 200  $\mu\text{L}$   $\text{H}_2\text{O}$ . Protein digestion was carried out with 1  $\mu\text{L}$  trypsin (trypsin/protein ratio 1:100, 0.5  $\mu\text{g}/\mu\text{L}$ , sequencing grade, *Promega*) in 100  $\mu\text{L}$  of 50 mM triethylammonium bicarbonate (TEAB) overnight at 800 rpm and 37  $^{\circ}\text{C}$  in a plate shaker with a heated lid. The plate was tightly sealed during digestion. The next day, peptides were eluted from the beads in the liquid handling system with 50  $\mu\text{L}$  3% FA and transferred into new wells for desalting. Desalting was performed using pre-equilibrated stage tips containing two layers of styrene-divinylbenzene-reverse phase sulfonate (SDB-RPS) disks (*Empore*, *3M*) as previously described<sup>183</sup>. The stage tips were equilibrated with 150  $\mu\text{L}$  wash buffer 1 (1% TFA in isopropanol) before loading the samples. Samples were loaded for 10 min at 500 x g, followed by washing with 150  $\mu\text{L}$  wash buffer 1 for 10 min at 800 x g, and another wash with 150  $\mu\text{L}$  wash buffer 2 (0.2% TFA in  $\text{H}_2\text{O}$ ). Peptides were eluted with 50  $\mu\text{L}$  elution buffer (1% ammonia, 80% acetonitrile) for 5 min at 300 x g, followed by 5 min at 800 x g. Eluted peptide samples were dried using a centrifugal evaporator (*Concentrator Plus*, *Eppendorf*) and then reconstituted in 35  $\mu\text{L}$  of 1% FA. Four microliters of each sample were used for LC-MS/MS measurements on a timsTOF Pro mass spectrometer (*Bruker*) in data-independent acquisition (DIA) mode. Preparative MS samples were conducted in n = 4 biologically independent replicates.

#### 4.18. Full Proteome Analysis

For each biological replicate, an overnight culture of *S. aureus* USA300 Lac (JE2) was inoculated to an  $\text{OD}_{600}$  of 0.06 in 5 mL B medium supplemented with various concentrations of

**L15** (1.5  $\mu$ M, 3  $\mu$ M, 4.5  $\mu$ M, 5  $\mu$ M, 5.5  $\mu$ M, and 6  $\mu$ M) or DMSO as a control (1% final DMSO concentration) and 25 mM NaHCO<sub>3</sub>. The cells were grown for 5 h at 200 rpm and 37 °C, and the OD<sub>600</sub> was adjusted to 2 using PBS. 1 mL of the adjusted cell suspension was used, and the cells were washed with PBS by centrifugation for 5 min at 6,000 x g and 4 °C. Lysis was performed with 150  $\mu$ L PBS supplemented with 0.5% SDS and 1% Triton X-100. Each sample was first sonicated for 10 s at 30% intensity (Sonopuls HD 2070 ultrasonic rod, *Bandelin electronic GmbH*), followed by mechanical cell disruption. The cell suspension was transferred to bead-mill tubes filled with 0.1 mm zirconium beads, and the cells were lysed with a bead beater homogenizer (Precellys 24 Homogenizer, *Bertin Technologies*) in three cycles: 30 s at 6,500 rpm, followed with a break for 30 s. The tubes were then centrifuged for 10 min at 10,000 x g and RT, and the supernatant was transferred to a new Eppendorf tube, followed by an additional centrifugation for at least 30 min at 21,000 x g and RT. The supernatant was transferred to new LoBind tubes (*Eppendorf*), and the protein concentration of each sample was determined using a BCA assay (Roti Quant, *Roth*). All samples were adjusted to a total protein amount of 15  $\mu$ g in a final volume of 80  $\mu$ L and transferred to a 96-well plate (Polypropylene, V-bottom, *Greiner* cat. 651201). For protein alkylation, a 1:2 mixture of 500 mM TCEP and 500 mM IAA was prepared, and 3  $\mu$ L was added to each sample. After incubation for 15 min at 950 rpm and RT, the excess IAA was quenched by adding 2  $\mu$ L of 500 mM DTT per sample. Further sample processing adhered to an adapted protocol for magnetic bead enrichment<sup>122</sup>. To each sample, 10  $\mu$ L of a 1:1 mix of washed (3x with H<sub>2</sub>O) hydrophobic and hydrophilic carboxylate-coated magnetic beads (*Cytiva*, cat# 65152105050250 and 45152105050250) was added. This was followed by the addition of 150  $\mu$ L EtOH to precipitate the proteins onto the beads. The subsequent steps were carried out using an automated liquid handling system (Hamilton Microlab Prep, *Hamilton*). The plate was incubated for 5 min at 500 rpm and RT, followed by washing of the beads. Each washing step was performed using a 96-well ring magnet (Alpaqua, *Magnum FLX*). The plate was placed on the magnet, and the supernatant was removed slowly (20  $\mu$ L/s) to avoid losing any beads. Washing involved removing the plate from the magnet, adding the respective washing solution, and shaking for 1 min at 800 rpm and RT. The samples were washed three times with 180  $\mu$ L of 80% EtOH and once with 180  $\mu$ L acetonitrile. Protein digestion was performed with 0.2  $\mu$ L trypsin (trypsin/protein ratio 1:100, 0.5  $\mu$ g/ $\mu$ L, sequencing grade, *Promega*) in 100  $\mu$ L of 50 mM TEAB overnight at 800 rpm and 37 °C in a plate shaker with a heated lid. The plate was tightly sealed during digestion. The next day, peptides were eluted from the beads in the liquid handling system with 50  $\mu$ L of 3% FA and transferred to new wells for desalting. Desalting was performed using pre-equilibrated stage tips containing two layers of SDB-RPS disks (*Empore*, *3M*) as previously described<sup>183</sup>. The stage tips were equilibrated with 150  $\mu$ L wash buffer 1 (1% TFA in isopropanol) before loading the samples. Samples were loaded for



10 min at 500 x g, followed by washing with 150  $\mu$ L wash buffer 1 for 10 min at 800 x g, and another wash with 150  $\mu$ L wash buffer 2 (0.2% TFA in H<sub>2</sub>O). Peptides were eluted with 50  $\mu$ L elution buffer (1% ammonia, 80% acetonitrile) for 5 min at 300 x g, followed by 5 min at 800 x g. Eluted peptide samples were dried using a centrifugal evaporator (Concentrator Plus, *Eppendorf*) and then reconstituted in 50  $\mu$ L of 1% FA. One microliter of each sample was used for LC-MS/MS measurements on a timsTOF Pro mass spectrometer (*Bruker*) in data-independent acquisition mode. Full proteome samples were performed in n = 4 independent replicates.

#### 4.19. LC-MS/MS Measurements and Data Analysis with timsTOF Pro

##### LC-MS/MS Measurements on timsTOF Pro.

Peptides were analyzed and separated online using an UltiMate 3000 nano HPLC system (*Dionex*) coupled to a *Bruker* timsTOF Pro mass spectrometer through a CaptiveSpray nano-electrospray ion source and a *Sonation* column oven. Initially, peptides were loaded onto the trap column (Acclaim PepMap 100 C18, 75  $\mu$ m ID x 2 cm, 3  $\mu$ m particle size, *Thermo Fisher Scientific*) and washed with 0.1% FA in H<sub>2</sub>O for 7 min at a flow rate of 5  $\mu$ L/min. Subsequently, they were transferred to the separation column (Aurora C18 column, 25 cm x 75  $\mu$ m, 1.7  $\mu$ m, *IonOpticks*) and separated using a gradient: 5% to 17% B over 36 min, 17% to 25% B over 18 min, 25% to 37% B over 6 min, and finally held at 95% B for 10 min before re-equilibration, at a flow rate of 400 nL/min. Mobile phase A was 0.1% FA in H<sub>2</sub>O, and mobile phase B was 0.1% FA in acetonitrile. The timsTOF Pro operated in data-independent dia-PASEF mode, with the dual TIMS analyzer configured to equal accumulation and ramp times of 100 ms each, and a 1/K0 ion mobility range from 0.60 to 1.60 V x s/cm<sup>2</sup> for MS1 scans. For fragmentation, dia-PASEF settings included a mass range of 400 to 1,201 m/z and an ion mobility range of 0.60 to 1.43 V x s/cm<sup>2</sup>. Each dia-PASEF scan comprised two ion mobility isolation windows of 26 m/z widths. The setup covered the mass range with 32 isolation windows and 1 m/z overlaps, resulting in 16 dia-PASEF scans per MS1 scan and a total cycle time of approximately 1.80 s (Table 11). The collision energy was ramped linearly from 59 eV at 1/K0 = 1.3 V x s/cm<sup>2</sup> to 20 eV at 1/K0 = 0.85 V x s/cm<sup>2</sup>. TIMS elution voltages were calibrated linearly using three *Agilent* ESI-L Tuning Mix ions (m/z 622, 922, and 1,222) spiked into the CaptiveSpray Source inlet filter to obtain the reduced ion mobility coefficients (1/K0).

**Table 11:** DIA-PASEF scan windows including ion mobility range (1/K<sub>0</sub>) and scan width (m/z). This table was adapted from a previous study<sup>66</sup>.

MS Type	Scan	Start IM [1/K <sub>0</sub> ]	End IM [1/K <sub>0</sub> ]	Start Mass [m/z]	End Mass [m/z]
MS1	0	0.6	1.6	100	1700
dia-PASEF	1	0.9	1.2	800	826
dia-PASEF	1	0.6	0.9	400	426
dia-PASEF	2	0.92	1.22	825	851
dia-PASEF	2	0.62	0.92	425	451
dia-PASEF	3	0.93	1.23	850	876
dia-PASEF	3	0.63	0.93	450	476
dia-PASEF	4	0.95	1.25	875	901
dia-PASEF	4	0.65	0.95	475	501
dia-PASEF	5	0.96	1.26	900	926
dia-PASEF	5	0.66	0.96	500	526
dia-PASEF	6	0.98	1.28	925	951
dia-PASEF	6	0.68	0.98	525	551
dia-PASEF	7	0.99	1.29	950	976
dia-PASEF	7	0.69	0.99	550	576
dia-PASEF	8	1.01	1.31	975	1001
dia-PASEF	8	0.71	1.01	575	601
dia-PASEF	9	1.02	1.32	1000	1026
dia-PASEF	9	0.72	1.02	600	626
dia-PASEF	10	1.04	1.34	1025	1051
dia-PASEF	10	0.74	1.04	625	651
dia-PASEF	11	1.06	1.36	1050	1076
dia-PASEF	11	0.76	1.06	650	676
dia-PASEF	12	1.07	1.37	1075	1101
dia-PASEF	12	0.77	1.07	675	701
dia-PASEF	13	1.09	1.39	1100	1126
dia-PASEF	13	0.79	1.09	700	726
dia-PASEF	14	1.1	1.4	1125	1151
dia-PASEF	14	0.8	1.1	725	751
dia-PASEF	15	1.12	1.42	1150	1176
dia-PASEF	15	0.82	1.12	750	776
dia-PASEF	16	1.13	1.43	1175	1201
dia-PASEF	16	0.83	1.13	775	801

### Data Analysis of timsTOF Pro Measurements.

MS data were processed using DIA-NN<sup>184</sup> (version 1.8.1) in library-free mode. The UniProt reference proteome for *S. aureus* USA300 (taxon identifier: 367830, downloaded on 30.06.2022) was used to generate the library. The settings for precursor ion generation

included creating a library and using deep-learning algorithms to predict spectra, retention times, and ion mobilities. Trypsin/P was specified as the protease, allowing for a maximum of two missed cleavages. The method included excising N-terminal methionine and applying carbamidomethylation to cysteines as a fixed modification, and no variable modifications were used. Peptide lengths were set to range from 7 to 30 residues, and precursor charges were set between 2 and 4. The precursor m/z range was set from 300 to 1,800, and the fragment m/z range was set from 200 to 1,800 for TIMS data.

The precursor FDR was set at 0.01. Settings for mass accuracy, MS1 accuracy, and scan window were all configured to 0. Features such as isotopologues, match-between-runs, and removal of likely interferences were activated. The neural network classifier operated in single-pass mode, conducting protein inference at the gene level with heuristic protein inference enabled (--relaxed-prot-inf). Quantification was carried out using the robust LC (high precision) strategy. Cross-run normalization was dependent on retention times, smart profiling was employed for library generation, and optimal settings were used for both speed and RAM usage.

After DIA-NN<sup>184</sup> analysis, LFQ quantities for all protein groups were analyzed using Perseus software<sup>185</sup> (version 2.03.1). LFQ intensities were log<sub>2</sub> transformed, and protein groups were filtered to retain those with at least three valid values in at least one group. Missing values in **L15-P** enrichment samples were imputed from a normal distribution with default settings (width = 0.3 and down shift = 1.8 for total matrix), while no imputation was done for full proteome samples. A two-sample student's t-test with permutation-based multiple testing correction (FDR = 0.05) was used for all relevant comparisons to determine fold change values and statistical significance. Results tables were exported, and graphs were generated using *GraphPad Prism* 10.01.

#### 4.20. Expression and Purification of MBP-tagged *S. aureus* SpsB in *E. coli*

Protein expression and purification of MBP-tagged *S. aureus* SpsB was performed by *M. K. von Wrisberg* as previously described<sup>163</sup>. The pETMBP-1a-His-MBP-SpsB vector was transformed into *E. coli* BL21 (DE3) for protein expression. An overnight culture of the transformed strain in LB medium with 50 µg/mL kanamycin was diluted 1:100 in fresh LB medium (1 L culture with 50 µg/mL kanamycin) and incubated at 200 rpm and 37 °C until the OD<sub>600</sub> reached 0.45 – 0.6. Protein expression was induced with 0.3 mM isopropyl-β-D-1-thiogalactopyranoside (IPTG), and the culture was incubated for an additional 3 h at 200 rpm and 25 °C. Cells were harvested by centrifugation for 10 min at 5,000 x g and 4 °C. Protein purification was conducted at 4 – 8 °C or on ice, unless otherwise specified, using two steps:

(1) MBP-affinity chromatography followed by (2) size-exclusion chromatography (SEC), both performed on an ÄKTA-FPLC system (*Cytiva*). For cell lysis, the pellet was resuspended in 30 mL lysis buffer (20 mM Tris, pH 8, 200 mM NaCl, 1 mM EDTA, 5% (w/v) glycerol, 1 mM DTT), containing 0.1 mg/mL DNase I (*AppliChem*) and one cOmplete ULTRA EDTA-free protease inhibitor tablet (*Roche*), followed by homogenization with an EmulsiFlexC5 (*Avestin Inc.*). The lysate was obtained by centrifugation for 30 min at 25,000 x g and 4 °C and filtered through a Whatman folded filter (*Cytiva*) before loading onto a MBPTrap HP column (*Cytiva*). The column was washed with wash buffer (20 mM Tris, pH 8, 200 mM NaCl, 1 mM EDTA, 5% (v/v) glycerol, 1 mM DTT) and the protein was eluted with elution buffer (20 mM Tris pH 8, 200 mM NaCl, 1 mM EDTA, 5% (v/v) glycerol, 1 mM DTT, 10 mM maltose). The fractions containing MBP-SpsB were pooled and concentrated using an Amicon Ultracell Centrifugal filter unit (MWCO 10 kDa, *Merck Millipore*). The second purification step involved loading the concentrated sample onto an equilibrated HiLoad Superdex 75 (16/60) column (*Cytiva*). The column was equilibrated with SEC buffer (20 mM Tris-HCl pH 8, 200 mM NaCl, 5% (v/v) glycerol, 1 mM DTT). Fractions containing pure MBP-SpsB were pooled and concentrated. For storage, protein aliquots were snap-frozen in liquid nitrogen and kept at -80 °C.

#### 4.21. Binding Site Identification by isoDTB A/BPP

Binding site identification studies of **L15-P** on SpsB were done by a mass spectrometry workflow using isotopically labeled desthiobiotin azide tags<sup>169,170</sup> as described previously<sup>163</sup>. All reagents used were of LC-MS grade.

##### Sample Preparation.

Eight samples of recombinantly purified MBP-tagged extracellular domain of SpsB were diluted in PBS to a final concentration of 5 µM. Each 100 µL sample was placed in a well of a transparent, flat-bottom 96-well plate (Transparent Nunc 96-well flat bottom, *Thermo Fisher Scientific*). **L15-P** was then added to each sample to reach a concentration of 5 µM, and the samples were incubated on a rolling plate for 45 min at RT. After incubation, the samples were UV-irradiated using FL8BL-B lamps (*Hitachi*) for 5 min, then transferred to Protein LoBind tubes (*Eppendorf*).

##### Click, Reduction, Alkylation, and Digestion.

Two click mix solutions with either heavy or light isoDTB tags were prepared by combining 36 µL of 0.9 mg/mL TBTA in 80% tBuOH and 20% DMSO, 12 µL of 13 mg/mL TCEP in H<sub>2</sub>O, and 12 µL of 50 mM CuSO<sub>4</sub> in H<sub>2</sub>O. To each click mix, 6 µL of heavy or light isoDTB (5 mM in DMSO) was added. Each SpsB sample (4x heavy and 4x light) received 12 µL of the final click mix solution, followed by incubation for 1 h at RT. For each replicate, a heavy and a light

sample were combined, and proteins were precipitated with 800  $\mu$ L ice-cold acetone, then incubated for at least 2 h at  $-20^{\circ}\text{C}$ . Proteins were pelleted by centrifugation for 10 min at  $13,000 \times g$  and  $4^{\circ}\text{C}$ , and the resulting pellet was washed twice with 500  $\mu$ L ice-cold MeOH *via* mild sonication for 10 s at 10% intensity (Sonopuls HD 2070 ultrasonic rod, *Bandelin electronic GmbH*). The supernatant was carefully removed, and the protein pellet was air-dried for 10 min. The pellet was then dissolved in 60  $\mu$ L of 8 M urea in 0.1 M TEAB *via* mild sonication for 10 s at 10% intensity. Each sample was reduced with 3  $\mu$ L of 31 mg/mL DTT in  $\text{H}_2\text{O}$  for 45 min at 850 rpm and  $37^{\circ}\text{C}$  (ThermoMixer C, *Eppendorf*). Free cysteines were then carbamidomethylated with 3  $\mu$ L of 74 mg/mL IAA in  $\text{H}_2\text{O}$  for 30 min at 850 rpm and  $37^{\circ}\text{C}$ . The remaining IAA was quenched with 3  $\mu$ L of 31 mg/mL DTT in  $\text{H}_2\text{O}$  for 30 min at 850 rpm and  $37^{\circ}\text{C}$ . Digestion was performed with 1  $\mu$ L trypsin (trypsin/protein ratio 1:100, 0.5  $\mu\text{g}/\mu\text{L}$ , sequencing grade, Promega) in 180  $\mu$ L of 0.1 M TEAB overnight at 220 rpm and  $37^{\circ}\text{C}$  (Incubator Shaker, *Eppendorf New Brunswick*).

#### Enrichment.

Each digested sample was incubated with 600  $\mu$ L of high-capacity streptavidin agarose beads (*Fisher Scientific*), which have been washed three times with 0.1% NP-40 in PBS, for 1 h on a disc rotator at RT. Samples were centrifuged for 2 min at  $1,000 \times g$  and RT to remove the supernatant. Then, 600  $\mu$ L of 0.1% NP-40 in PBS was added to each sample and transferred onto centrifugation columns (*Fisher Scientific Pierce*<sup>TM</sup>). The beads were washed sequentially with 600  $\mu$ L of 0.1% NP-40 in PBS, three times with 600  $\mu$ L PBS, and three times with 600  $\mu$ L  $\text{H}_2\text{O}$ . Elution was performed with 200  $\mu$ L of 0.1% TFA in 50% aqueous  $\text{H}_2\text{O}$ , followed by two additional elutions with 100  $\mu$ L of the same buffer each. Samples were dried using a centrifugal evaporator (Concentrator Plus, *Eppendorf*) and reconstituted in 12.5  $\mu$ L of 0.1% TFA for LC-MS/MS measurements on an Orbitrap Eclipse Tribrid mass spectrometer (*Thermo Fisher Scientific*) in data-dependent acquisition (DDA) mode.

#### LC-MS/MS Measurements on Orbitrap Eclipse Tribrid.

IsoDTB samples were analyzed according to a published procedure<sup>170</sup>. Peptides were examined using HPLC-MS/MS on a Vanquish Neo UHPLC system (*Thermo Fisher Scientific*) equipped with a PepMap<sup>TM</sup> Neo 5  $\mu\text{m}$  C18 300  $\mu\text{m}$  x 5 mm Trap Cartridge (*Thermo Fisher Scientific*) and Aurora Ultimate<sup>TM</sup> separation columns (3rd generation, 20 cm nanoflow UHPLC compatible, *Ionopticks*). A Nanospray Flex Ion Source (*Thermo Fisher Scientific*) was connected to an Orbitrap Eclipse Tribrid instrument (*Thermo Fisher Scientific*). The Vanquish Neo UHPLC operated in Trap-and-Elute-Injection mode, loading samples onto the trap column. Peptide separation occurred at a 400 nL/min flow rate using buffer A (0.1% FA in  $\text{H}_2\text{O}$ ) and buffer B (0.1% FA in acetonitrile). The separation column was maintained at  $40^{\circ}\text{C}$ .

Peptides were separated over a 75-minute gradient, starting from 5% to 40% buffer B for 60 min, then reaching 60% B over 5 min, followed by a 10-minute isocratic wash with 90% B. For washing and equilibration, the Vanquish Neo system settings were: 5% B, fast equilibration enabled, and equilibration factor set to 3; for the trap column: fast wash, equilibration, and zebra wash enabled (two zebra wash cycles, automatic equilibration factor). The Orbitrap Eclipse mass spectrometer operated in DDA mode with internal real-time mass calibration using a user-defined lock mass ( $m/z = 445.12003$ , positive). Full MS scans in the orbitrap covered a range of 300 – 1500  $m/z$  at a resolution of 120,000 with an AGC target of  $4e5$  and maximum injection time set to auto. The top 10 intense ions (charge states 2 – 7) were selected for MS2 scans with a minimum intensity threshold of  $5.0e3$ , isotope exclusion, and dynamic exclusion (30 s exclusion duration). Peaks with unassigned charges or a charge of +1 were excluded. MS2 spectra were collected at a resolution of 15,000 with an AGC target of  $5e4$ . The maximum injection time was kept at the default setting. Isolation in the quadrupole was performed with a 1.6  $m/z$  window. Fragments were generated using higher-energy collision-induced dissociation with a normalized collision energy of 30% and detected in the orbitrap. Data acquisition was conducted using *Thermo Scientific* Foundation software version 3.1sp9 and Xcalibur version 4.6. IsoDTB samples were analyzed in  $n = 4$  independent replicates.

#### Data Analysis of Orbitrap Eclipse Measurements.

The data analysis was conducted as previously described<sup>163,170</sup>, adjusted for binding site identification studies. Results and filtered outcomes from the open and modified closed searches are summarized and available in the PRIDE<sup>186</sup> partner repository with the dataset identifier PXD051986.

#### *General Setup of Analysis Software*

The raw data from LC-MS/MS analyses were converted into mzML format using the MSconvert tool (version 3.0.21193-ccb3e0136) from the ProteoWizard software<sup>187</sup> (version 3.0.21193, 64-bit), with default settings and vendor peak picking enabled. For subsequent data analysis, the FragPipe<sup>171–175</sup> interface (version 20.0) was used, incorporating MSFragger<sup>171</sup> (version 3.8), Philosopher<sup>188</sup> (version 5.0.0), IonQuant<sup>189</sup> (version 1.9.8), and Python (version 3.7.3). The UniProt reference proteome for *S. aureus* NCTC8325 (taxon identifier: 93061, downloaded on 22.08.2023, noting an annotation error in SpsB, Q2FZT7, which is missing amino acids 1-36) was utilized. Reverse sequences were manually appended to the FASTA databases.

#### *Open Search Analysis of Mass of Modifications with FragPipe<sup>171–175</sup>*

The observed mass shifts in the peptides of MBP-SpsB were analyzed using an *Open Search* with MSFragger<sup>171</sup>. The following parameters were applied for the analysis: precursor mass

tolerance ranged from -150 to 1,000 Da, and initial fragment mass tolerance was set to 20 ppm, with enabled mass calibration and parameter optimization. The isotope error was set to '0', and trypsin was specified as the enzyme with cleavage after 'KR' but not before 'P'. The settings allowed for up to two missed cleavages and enabled N-terminal clipping. Peptide lengths ranged from 7 to 50 amino acids, and peptide masses ranged from 500 to 5,000 Da, and no variable or fixed modifications were used. All other settings were kept at their defaults. Crystal-C<sup>172</sup> was enabled. PeptideProphet<sup>188</sup> was run with these parameters: '--nonparam --expectscore --decoyprobs --masswidth 1,000.0 --clevel -2'. PTMProphet was not utilized. ProteinProphet<sup>188</sup> was executed with the setting '--maxppmdiff 2,000,000'. Report generation was enabled with '--sequential --razor --mapmods --prot 0.01'; MS1 quantification and TMT-integrator were disabled. PTM-Shepherd<sup>175</sup> was activated using the following settings: a smoothing factor of '2', a precursor tolerance of '0.01 Da', a prominence ratio of '0.3', a peak picking width of '0.002 Da', a localization background of '4', and an annotation tolerance of '0.01 Da'. A custom mass shift list, including only UniMod modifications with molecular weights under 400 Da, was employed as previously published<sup>170</sup>. Modifications were assigned to 'b' and 'y' ion types, with the mass fragment charge set to '2'. The generation of a spectral library was disabled. For downstream data analysis, the 'global.modsummary.tsv' file was examined for mass shifts exceeding 482 Da (exact masses of light tag: 482.2834 Da and heavy tag: 488.2909 Da) and for mass shift differences of  $6.0075 \pm 0.0010$  Da between heavy and light isoDTB tags linked to **L15-P**. The filtered results are summarized in Table 9.

#### *Modified Closed Search Analysis for Binding Site Identification Studies with FragPipe<sup>171–175</sup>*

A modified *Closed Search* was carried out to identify the binding site of **L15-P** using MSFragger<sup>171</sup>, configured with the following parameters: a precursor mass tolerance of -20 to 20 ppm, a fragment mass tolerance of 20 ppm, and enabled mass calibration and parameter optimization. The isotope error was set to '0/1/2'. Trypsin was specified as the enzyme, with cleavage occurring after 'K' but not before 'P', allowing for up to two missed cleavages. N-terminal clipping was enabled. Peptide lengths were defined to range from 7 to 50 amino acids, and peptide masses from 500 to 5,000 Da, with no mass offsets. All other settings remained at their default values. The fixed and variable modifications were assigned to the masses 832.436 and 838.4426 Da, corresponding to the **L15-P**-isoDTB tag adducts that were identified in the *Open Search*. Crystal-C<sup>172</sup> was disabled. PeptideProphet<sup>188</sup> was executed with the parameters: '--decoyprobs --ppm --accmass --nonparam --expectscore'. PTMProphet was not utilized in this analysis. ProteinProphet<sup>188</sup> was run with the setting '--maxppmdiff 2,000,000'. Report generation was enabled with the options '--sequential --prot 0.01'. PTM-Shepherd<sup>175</sup> was disabled for this process. MS1 quantification was conducted with IonQuant<sup>189</sup> enabled, including MaxLFQ with a minimum of 2 ions. Detected masses from Table 9 were used for

labeling-based quantification of all amino acids (\*), with re-quantify enabled, the top 3 ions considered, a minimum frequency of 0.5, at least 1 scan, and a minimum of 2 isotopes. Normalization was turned off, the retention time window was set to 0.4 min, and the m/z window was set to 10 ppm. TMT-Integrator and spectral library generation were disabled. Each quadruplicate run was analyzed as an individual experiment. The 'ion\_label\_quant.tsv' files from the four experiments were individually reviewed. For each entry, the 'Modified Peptide' was identified as either the 'Light Modified Peptide' or the 'Heavy Modified Peptide' based on the higher 'PeptideProphet Probability'. Modification masses in the 'Modified Peptide' were replaced with '\*', and any carbamidomethylation mass (57.0215 Da) was removed. The full protein sequence was linked to the table. Peptide sequences that were not unique to the same protein were excluded, and the position of the modified residue was determined. The 'Identifier' was formatted as 'UniProtCode'\_\*residue number, where \* represents the one-letter code of the modified amino acid. The average 'Log<sub>2</sub> Ratio HL', which is the log<sub>2</sub>-transformed ratio of heavy and light ions, was calculated as the weighted average of all corresponding ions' 'Log<sub>2</sub> Ratio HL' values, weighted by the ion's 'Total Intensity'. This value was disregarded if the standard deviation of 'Log<sub>2</sub> Ratio HL' values exceeded 1.41 for all ions of the same 'Identifier'. For each 'Identifier', 'Total Intensity', 'Total Light Intensity', and 'Total Heavy Intensity' were summed across all individual ions. The shortest sequence was retained if multiple 'Modified Peptides' were found for the same 'Identifier'. Data from all four replicates were combined into a single table. The 'Log<sub>2</sub> Ratio HL' values for the replicates were labeled as 'Log<sub>2</sub> R Replicate 1', 'Log<sub>2</sub> R Replicate 2', 'Log<sub>2</sub> R Replicate 3', and 'Log<sub>2</sub> R Replicate 4'. The average of these values was calculated and termed 'Log<sub>2</sub> R Average', excluding values where the standard deviation between replicates exceeded 1.41. Values were kept if the identifier was quantified in at least one replicate. The peptide sequence consistently modified across all four replicates was identified as the **L15-P** binding site to SpsB (Table 10).

#### 4.22. Preparation of Membrane Fractions Harboring *S. aureus* SpsB in *E. coli*

Cloning of SpsB mutants and preparation of *E. coli* membrane fractions was done by *Michaela K. Fiedler*.

*E. coli* membrane fractions with overexpressed *S. aureus* SpsB were prepared according to a published procedure<sup>42,190</sup>. *E. coli* BL21(DE3) pLysS cells were first transformed with pET-55-DEST-fl-SpsB or respective mutant plasmids (F67A, Y75A, F158A, or Q165A)<sup>163</sup>. The transformed cells were grown in LB medium supplemented with 100 µg/mL ampicillin and 34 µg/mL chloramphenicol at 200 rpm and 37 °C until the OD<sub>600</sub> reached 0.6. Protein overexpression was induced with 0.5 mM IPTG, and cells were further incubated for 3 h at



200 rpm and 22 °C. Cells were harvested by centrifugation for 10 min at 6,000 x g and 4 °C. The cell pellet was washed once with PBS and resuspended in 5 mL of 50 mM Tris-HCl buffer (pH 7.5). Lysis was performed using a bead beater homogenizer (Precellys Ceramic Kit CK01L, 7.0 mL tubes; Precellys 24 Homogenizer, *Bertin Technologies*) in three cycles of 45 s at 5,500 rpm, with cooling for 30 s between cycles. To remove cell debris, the lysate was centrifuged for 10 min at 12,000 x g and 4 °C. The supernatant was then centrifuged for 75 min at 39,000 x g and 4 °C, and the cell membranes were collected. The membranes were resuspended in 50 mM ice-cold sodium phosphate buffer (pH 7.5), and the protein concentration was determined using a BCA assay (Roti Quant, *Roth*). Membranes were snap-frozen in liquid nitrogen and stored at -80 °C for future use. For the preparation of the *E. coli* membrane control fractions, the same procedure was followed without IPTG induction.

#### 4.23. FRET-based SpsB Assay with Membrane-bound SpsB

The activity of overexpressed full-length *S. aureus* SpsB or its mutants (F67A, Y75A, F158A, or Q165A) in *E. coli* membranes was measured using a FRET assay as previously described<sup>42,191</sup>. FRET assays were conducted with overexpressed wild-type SpsB or the respective mutants (F67A, Y75A, F158A, or Q165A) in *E. coli* membranes. Background activity was assessed using control membranes that were not induced with IPTG. A synthetic peptide based on SceD (DABCYL-AGHDAHASET-EDANS, #AS-64916, *AnaSpec*), modified with 4-(4-dimethylaminophenylazo)benzoic acid and 5-((2-aminoethyl)amino)-1-naphthalenesulfonic acid, was used as a FRET substrate. Each assay was performed with 100 µL of 50 µg/mL respective membranes in 50 mM sodium phosphate buffer (pH 7.5), treated with either the compound of interest or DMSO as a control for 5 min at 37 °C. Depending on the experimental requirements, detergents were added to the sodium phosphate buffer: 0.1% CHAPS, 0.001% NP-40, or 0.01% Tween-20. Following this, 1 µL of 10 mM FRET substrate in DMF was added to each sample, and fluorescence was recorded using an Infinite™ M Nano Tecan 200Pro plate reader at an excitation wavelength of 340 nm and an emission wavelength of 510 nm for at least 2 h at 37 °C. Background activity from non-induced *E. coli* membranes was subtracted, and initial substrate cleavage velocities within the first 1,000 s were determined *via* simple linear regression using *GraphPad Prism* 10.01. Each sample was normalized to DMSO, which represented 100% substrate cleavage. Each measurement was performed in n = 3 biologically independent replicates per condition, with three technical replicates each. Statistical significance was determined using ordinary one-way ANOVA.

#### 4.24. Molecular Dynamics (MD) Simulations

Modeling and MD studies were performed by *Shu-Yu Chen*.

The ternary complexes of SpsB-substrate-**L15** and SpsB-substrate-**D13** were created by docking **L15** or **D13** to the substrate-bound SpsB model following the method described previously<sup>163</sup> using Autodock Vina<sup>192</sup>. The best-scored binding poses were chosen for further simulations and analyses. These complexes were embedded in a dimyristoyl phosphatidylglycerol bilayer and solvated in water and 0.15 M NaCl *via* the CHARMM-GUI<sup>193</sup> online server. Interactions between atoms were described with ff19SB<sup>194</sup> for proteins, lipid21<sup>195</sup> for the membrane, GAFF2<sup>196</sup> for **L15** and **D13**, and OPC<sup>197</sup> for water molecules. Point charges for **L15** and **D13** were assigned using the AM1-BCC<sup>198</sup> charging method in Antechamber<sup>199</sup>. For each ternary complex, five 1  $\mu$ s simulations were conducted with randomly assigned initial atomic velocities. The simulations started with energy minimization and equilibration, as previously described<sup>163</sup>, using cuda-accelerated PMEMD in the Amber 22<sup>200</sup> package. Temperature and pressure were maintained at 303.15 K and 1 bar, using a Langevin thermostat<sup>201</sup> and Berendsen barostat<sup>202</sup>. A time step of 4 fs was used, enabled by the SHAKE algorithm<sup>203</sup> and hydrogen mass repartitioning<sup>204</sup>. Water accessibilities and geometric measurements between atoms were calculated using PTRAJ and CPPTRAJ<sup>205</sup>. Data for **PK150**-bound simulations were obtained from a previous study<sup>163</sup>.

## 5. Abbreviations

ABP	Activity-based probe
ABPP	Activity-based protein profiling
AfBP	Affinity-based probe
AfBPP	Affinity-based protein profiling
Ala or A	Alanine
AMR	Antimicrobial resistance
ANOVA	Analysis of variance
Asp or D	Aspartic acid
B	Broth
BCA	Bicinchoninic acid
BHI	Brain heart infusion
C	Cytosine
CFU	Colony forming unit
CHAPS	3-[(3-cholamidopropyl)dimethylammonio]-1-propanesulfonate
CLSI	Clinical and laboratory standards institute
Da	Dalton
DABCYL	4-(4-dimethylaminophenylazo)benzoic acid
DDA	Data-dependent acquisition
DIA	Data-independent acquisition
DiSC <sub>3</sub> (5)	3,3'-dipropylthiadicarbocyanine iodide
DMEM	<i>Dulbecco's</i> modified eagle's medium
DMF	<i>N,N</i> -Dimethylformamide
DMSO	Dimethyl sulfoxide
DNA	Desoxyribonucleid acid
DTT	Dithiotreitol

<i>E. coli</i>	<i>Escherichia coli</i>
EDANS	5-((2-aminoethyl)amino)-1-naphthalenesulfonic acid
EDTA	Ethylenediaminetetraacetic acid
EM	Electron microscopy
EtOH	Ethanol
FA	Formic acid
FBS	Fetal bovine serum
FDR	False discovery rate
FoR	Frequency of resistance
FRET	Förster resonance energy transfer
FtsZ	Filamenting temperature-sensitive mutant Z
Gln or Q	Glutamine
IPTG	Isopropyl $\beta$ -d-1-thiogalactopyranoside
LB	Lysogeny broth
Lys or K	Lysine
HeLa	Cervical cancer cell line
HTS	High-throughput screen
IAA	Iodoacetamide
IC <sub>50</sub>	Half-maximal inhibitory concentration
IE	Inoculum effect
isoDTB	Isotopically-labeled desthiobiotin
K	Lysine
LC-MS/MS	Liquid chromatography-tandem mass spectrometry
Leu or L	Leucine
LFQ	Label free quantification
LMIC	Low-and middle-income country

MBC	Minimum bactericidal concentration
MBP	Maltose-binding protein
MD	Molecular dynamics
MeOH	Methanol
MIC	Minimum inhibitory concentration
MoA	Mechanism of action
MRSA	Methicillin-resistant <i>Staphylococcus aureus</i>
MS	Mass spectrometry
MTT	3-(4,5-dimethyl-2-thiazolyl)-2,5-diphenyltetrazolium bromide
NaHCO <sub>3</sub>	Sodium bicarbonate
NP-40	Polyethylene glycol nonylphenyl ether
m/z	Mass-to-charge ratio
OD	Optical density
P	Proline
Phe or F	Phenylalanine
PMF	Proton motif force
ppm	parts per million
R	Arginine
RNA	Ribonucleid acid
RT	Room temperature
SAR	Structure-activity relationship
<i>S. aureus</i>	<i>Staphylococcus aureus</i>
s.d.	Standard deviation
SDB-RPS	Styrene-divinylbenzene-reverse phase sulfonate
SDS	Sodium dodecyl sulfate
SDS-PAGE	Sodium dodecyl sulfate polyacrylamide gel electrophoresis

SEC	Size-exclusion chromatography
Ser or S	Serine
SNP	Single nucleotide polymorphism
SpsB	Signal peptidase IB
T	Thymine
tBuOH	<i>Tert</i> -butanol
TBTA	Tris(benzyltriazolmethyl)amine
TCEP	Tris(2-carboxyethyl)phosphine
TEAB	Triethylammonium bicarbonate
TFA	Trifluoroacetic acid
Triton X-100	2-[4-(2,4,4-trimethylpentan-2-yl)phenoxy]ethanol
TWEEN-20	Polyoxyethylene (20) sorbitan monolaurate
Tyr or T	Tyrosine
UV	Ultraviolet
WHO	World health organization
wt	Wild-type

## 6. References

1. Tang, K. W. K., Millar, B. C. & Moore, J. E. Antimicrobial Resistance (AMR). *Br. J. Biomed. Sci.* **80**, 1–11 (2023).
2. Smith, W. P. J., Wucher, B. R., Nadell, C. D. & Foster, K. R. Bacterial defences: mechanisms, evolution and antimicrobial resistance. *Nat. Rev. Microbiol.* **21**, 519–534 (2023).
3. Granato, E. T., Meiller-Legrand, T. A. & Foster, K. R. The Evolution and Ecology of Bacterial Warfare. *Curr. Biol.* **29**, R521–R537 (2019).
4. Sengupta, S., Chattopadhyay, M. K. & Grossart, H. P. The multifaceted roles of antibiotics and antibiotic resistance in nature. *Front. Microbiol.* **4**, 1–13 (2013).
5. Darby, E. M. *et al.* Molecular mechanisms of antibiotic resistance revisited. *Nat. Rev. Microbiol.* **21**, 280–295 (2023).
6. Murray, C. J. *et al.* Global burden of bacterial antimicrobial resistance in 2019: a systematic analysis. *Lancet* **6736**, (2022).
7. O'Neill, J. Antimicrobial Resistance: Tackling a crisis for the health and wealth of nations. *Rev. Antimicrob. Resist.* 1–16 (2014) doi:10.4102/ajlm.v7i2.830.
8. World Health Organization. *Bacterial Priority Pathogens List, 2024. Bacterial Priority Pathogens List, 2024: bacterial pathogens of public health importance to guide research, development and strategies to prevent and control antimicrobial resistance* (2024).
9. World Health Organization. *Antibacterial products in clinical development for priority pathogens*. <https://www.who.int/observatories/global-observatory-on-health-research-and-development/monitoring/antibacterial-products-in-clinical-development-for-priority-pathogens> (2024).
10. Zampaloni, C. *et al.* A novel antibiotic class targeting the lipopolysaccharide transporter. *Nature* **625**, 566–571 (2024).
11. Butler, M. S., Henderson, I. R., Capon, R. J. & Blaskovich, M. A. T. Antibiotics in the clinical pipeline as of December 2022. *J. Antibiot. (Tokyo)*. **76**, 431–473 (2023).
12. Kong, X. *et al.* ePath: an online database towards comprehensive essential gene annotation for prokaryotes. *Sci. Rep.* **9**, 1–11 (2019).
13. Coates, A., Hu, Y., Bax, R. & Page, C. The future challenges facing the development

- of new antimicrobial drugs. *Nat. Rev. Drug Discov.* **1**, 895–910 (2002).
14. Salam, M. A. *et al.* Antimicrobial Resistance: A Growing Serious Threat for Global Public Health. *Healthc.* **11**, 1–20 (2023).
  15. Hawkey, P. M. & Jones, A. M. The changing epidemiology of resistance. *J. Antimicrob. Chemother.* **64**, (2009).
  16. Ifan, M., Almotiri, A. & AlZeyadi, Z. A. Antimicrobial Resistance and Its Drivers—A Review. *Antibiotics* **11**, (2022).
  17. Ventola, C. L. The antibiotic resistance crisis: part 1: causes and threats. Pharmacy and Therapeutics. *Pharm. Ther.* **40**, 277–283 (2015).
  18. Klein, E. Y. *et al.* Global increase and geographic convergence in antibiotic consumption between 2000 and 2015. *Proc. Natl. Acad. Sci. U. S. A.* **115**, E3463–E3470 (2018).
  19. Bartlett, J. G., Gilbert, D. N. & Spellberg, B. Seven ways to preserve the Miracle of antibiotics. *Clin. Infect. Dis.* **56**, 1445–1450 (2013).
  20. Reck, F., Jansen, J. M. & Moser, H. E. Challenges of antibacterial drug discovery. *Arkivoc* **2019**, 227–244 (2019).
  21. Larsson, D. G. J. & Flach, C. F. Antibiotic resistance in the environment. *Nat. Rev. Microbiol.* **20**, 257–269 (2022).
  22. Shallcross, L. J., Howard, S. J., Fowler, T. & Davies, S. C. Tackling the threat of antimicrobial resistance: From policy to sustainable action. *Philos. Trans. R. Soc. B Biol. Sci.* **370**, (2015).
  23. Årdal, C. *et al.* Antibiotic development — economic, regulatory and societal challenges. *Nat. Rev. Microbiol.* **18**, 267–274 (2020).
  24. Bassetti, M. & Giacobbe, D. R. A look at the clinical, economic, and societal impact of antimicrobial resistance in 2020. *Expert Opin. Pharmacother.* **21**, 2067–2071 (2020).
  25. Shrestha, P. *et al.* Enumerating the economic cost of antimicrobial resistance per antibiotic consumed to inform the evaluation of interventions affecting their use. *Antimicrob. Resist. Infect. Control* **7**, 1–9 (2018).
  26. Dadgostar, P. Antimicrobial Resistance: Implications and Costs. *Infect. Drug Resist.* **12**, 3903–3910 (2019).
  27. Majumder, M. A. A. *et al.* Antimicrobial stewardship: Fighting antimicrobial resistance



- and protecting global public health. *Infect. Drug Resist.* **13**, 4713–4738 (2020).
28. Anderson, M. *et al.* Challenges and opportunities for incentivising antibiotic research and development in Europe. *Lancet Reg. Heal. - Eur.* **33**, 100705 (2023).
  29. O'Neill, J. Tackling drug-resistant infections globally: Final report and recommendations. *Arch. Pharm. Pract.* 1–76 (2016) doi:10.4103/2045-080x.186181.
  30. Fleming, A. On the antibacterial action of cultures of a penicillium, with special reference to their use in the isolation of *B. influenzae*. *Br. J. Exp. Pathol.* **10**, 226–236 (1929).
  31. Lesch, J. E. *The First Miracle Drugs: How the Sulfa Drugs Transformed Medicine.* (Oxford University Press Inc., 2007).
  32. Silver, L. L. Challenges of antibacterial discovery. *Clin. Microbiol. Rev.* **24**, 71–109 (2011).
  33. Iskandar, K. *et al.* Antibiotic Discovery and Resistance: The Chase and the Race. *Antibiotics* **11**, 1–38 (2022).
  34. Zhanel, G. G. *et al.* A critical review of oxazolidinones: An alternative or replacement for glycopeptides and streptogramins? *Can. J. Infect. Dis.* **12**, 379–390 (2001).
  35. Hoeksema, H., Johnson, J. L. & Hinman, J. W. STRUCTURAL STUDIES ON STREPTONIVICIN, 1 A NEW ANTIBIOTIC. *J. Am. Chem. Soc.* **77**, 6710–6711 (1955).
  36. Sum, P. *et al.* Glycylcyclines. 1. A New Generation of Potent Antibacterial Agents through Modification of 9-Aminotetracyclines. *J. Med. Chem.* **37**, 184–188 (1994).
  37. Swanson, S. J., Ranfranz, L. M., Whittern, D. N., Buko, A. M. & McAlpine, J. B. Tiacumicins, a Novel Complex of 18-Membered Macrolides II. Isolation and Structure Determination. *J. Antibiot. (Tokyo)*. **40**, 575–588 (1987).
  38. Cook, M. A. & Wright, G. D. The past, present, and future of antibiotics. *Sci. Transl. Med.* **14**, 1–12 (2022).
  39. Ito, T. & Masubuchi, M. Dereplication of microbial extracts and related analytical technologies. *J. Antibiot. (Tokyo)*. **67**, 353–360 (2014).
  40. Schneider, Y. K. Bacterial natural product drug discovery for new antibiotics: Strategies for tackling the problem of antibiotic resistance by efficient bioprospecting. *Antibiotics* **10**, (2021).
  41. Martin, J. K. *et al.* A Dual-Mechanism Antibiotic Kills Gram-Negative Bacteria and

- Avoids Drug Resistance. *Cell* **181**, 1518-1532.e14 (2020).
42. Le, P. *et al.* Repurposing human kinase inhibitors to create an antibiotic active against drug-resistant *Staphylococcus aureus*, persisters and biofilms. *Nat. Chem.* **12**, 145–158 (2020).
  43. Ruggieri, F. *et al.* Antibiotics with novel mode of action as new weapons to fight antimicrobial resistance. *Eur. J. Med. Chem.* **256**, (2023).
  44. Brötz-Oesterhelt, H. & Brunner, N. A. How many modes of action should an antibiotic have? *Curr. Opin. Pharmacol.* **8**, 564–573 (2008).
  45. L. Peck, R., Hoffhine Jr., C. E. & Folkers, K. STREPTOMYCES ANTIBIOTICS. IX. DIHYDROSTREPTOMYCIN. *Empl. Assist. Q.* **10**, 37–45 (1995).
  46. Stephens, C. R., Murai, K., Rennhard, H. H., Conover, L. H. & Brunings, K. J. HYDROGENOLYSIS STUDIES IN THE TETRACYCLINE SERIES—6-DEOXYTETRACYCLINES. *J. Am. Chem. Soc.* **922**, 5324–5325 (1945).
  47. LODER, B., NEWTON, G. G. & ABRAHAM, E. P. The cephalosporin C nucleus (7-aminocephalosporanic acid) and some of its derivatives. *Biochem. J.* **79**, 408–416 (1961).
  48. Wu, Y.-J. Highlights of Semi-synthetic Developments from Erythromycin A. *Curr. Pharm. Des.* **6**, 181–223 (2005).
  49. Leshner, G. Y., Froelich, E. J., Gruett, M. D., Bailey, J. H. & Brundage, R. P. 1,8-Naphthyridine Derivatives. A New Class of Chemotherapeutic Agents. *J. Med* **3348**, 1063–1065 (1962).
  50. Slee, A. M. *et al.* Oxazolidinones, a new class of synthetic antibacterial agents: in vitro and in vivo activities of DuP 105 and DuP 721. *Antimicrob. Agents Chemother.* **31**, 1791–1797 (1987).
  51. Wright, P. M., Seiple, I. B. & Myers, A. G. The evolving role of chemical synthesis in antibacterial drug discovery. *Angew. Chem. Int. Ed.* **53**, 8840–8869 (2014).
  52. Singh, S. B., Young, K. & Miesel, L. Screening strategies for discovery of antibacterial natural products. *Expert Rev. Anti. Infect. Ther.* **9**, 589–613 (2011).
  53. Ayon, N. J. High-Throughput Screening of Natural Product and Synthetic Molecule Libraries for Antibacterial Drug Discovery. *Metabolites* **13**, (2023).
  54. Forsyth, R. A. *et al.* A genome-wide strategy for the identification of essential genes in *Staphylococcus aureus*. *Mol. Microbiol.* **43**, 1387–1400 (2002).

55. Liu, Y. *et al.* Drug repurposing for next-generation combination therapies against multidrug-resistant bacteria. *Theranostics* **11**, 4910–4928 (2021).
56. Singh, S. B. & Barrett, J. F. Empirical antibacterial drug discovery - Foundation in natural products. *Biochem. Pharmacol.* **71**, 1006–1015 (2006).
57. Corso, G., Stärk, H., Jing, B., Barzilay, R. & Jaakkola, T. DiffDock: Diffusion Steps, Twists, and Turns for Molecular Docking. *arXiv Prepr. arXiv* (2022).
58. Adeshina, Y. O., Deeds, E. J. & Karanicolas, J. Machine learning classification can reduce false positives in structure-based virtual screening. *Proc. Natl. Acad. Sci. U. S. A.* **117**, 18477–18488 (2020).
59. Galloway, W. R. J. D., Bender, A., Welch, M. & Spring, D. R. The discovery of antibacterial agents using diversity-oriented synthesis. *Chem. Commun.* 2446–2462 (2009) doi:10.1039/b816852k.
60. Tracanna, V., de Jong, A., Medema, M. H. & Kuipers, O. P. Mining prokaryotes for antimicrobial compounds: From diversity to function. *FEMS Microbiol. Rev.* **41**, 417–429 (2017).
61. Navre, M. Application of combinatorial chemistry to antimicrobial drug discovery. *Expert Opin. Investig. Drugs* **7**, 1257–1271 (1998).
62. Hollert, T. P., Evdokimov, A. G. & Narasimhan, L. Structural biology approaches to antibacterial drug discovery. *Expert Opin. Drug Discov.* **2**, 1085–1101 (2007).
63. Stokes, J. M. *et al.* A Deep Learning Approach to Antibiotic Discovery. *Cell* **180**, 688–702.e13 (2020).
64. Theuretzbacher, U., Blasco, B., Duffey, M. & Piddock, L. J. V. Unrealized targets in the discovery of antibiotics for Gram-negative bacterial infections. *Nat. Rev. Drug Discov.* **22**, 957–975 (2023).
65. Lewis, K. Platforms for antibiotic discovery. *Nat. Rev. Drug Discov.* **12**, 371–387 (2013).
66. Schum, D. *et al.* Screening Privileged Alkyl Guanidinium Motifs under Host- Mimicking Conditions Reveals a Novel Antibiotic with an Unconventional Mode of Action. *JACS Au* **4**, 3125–3134 (2024).
67. Ersoy, S. C. *et al.* Correcting a Fundamental Flaw in the Paradigm for Antimicrobial Susceptibility Testing. *EBioMedicine* **20**, 173–181 (2017).
68. Farha, M. A., French, S., Stokes, J. M. & Brown, E. D. Bicarbonate Alters Bacterial

- Susceptibility to Antibiotics by Targeting the Proton Motive Force. *ACS Infect. Dis.* **4**, 382–390 (2018).
69. Hinnu, M., Putriņš, M., Kogermann, K., Bumann, D. & Tenson, T. Making Antimicrobial Susceptibility Testing More Physiologically Relevant with Bicarbonate? *Antimicrob. Agents Chemother.* **66**, 28–31 (2022).
  70. Zgurskaya, H. I., López, C. A. & Gnanakaran, S. Permeability Barrier of Gram-Negative Cell Envelopes and Approaches to Bypass It. *ACS Infect. Dis.* **1**, 512–522 (2016).
  71. Ghai, I. A Barrier to Entry: Examining the Bacterial Outer Membrane and Antibiotic Resistance. *Appl. Sci.* **13**, 18–20 (2023).
  72. Nikaido, H. Prevention of Drug Access to Bacterial Targets: Permeability Barriers and Active Efflux. *Science* **264**, 382–388 (1994).
  73. Richter, M. F. & Hergenrother, P. J. The challenge of converting gram-positive-only compounds into broad-spectrum antibiotics. *Ann. N. Y. Acad. Sci.* **1435**, 18–38 (2019).
  74. Richter, M. F. *et al.* Predictive compound accumulation rules yield a broad-spectrum antibiotic. *Nature* **545**, 299–304 (2017).
  75. Perlmutter, S. J. *et al.* Compound Uptake into E. coli Can Be Facilitated by N-Alkyl Guanidiniums and Pyridiniums. *ACS Infect. Dis.* **7**, 162–173 (2021).
  76. Muñoz, K. A. & Hergenrother, P. J. Facilitating Compound Entry as a Means to Discover Antibiotics for Gram-Negative Bacteria. *Acc. Chem. Res.* **54**, 1322–1333 (2021).
  77. Strecker, A. Untersuchungen über die chemischen Beziehungen zwischen Guanin, Xanthin, Theobromin, Caffein und Kreatinin. *Justus Liebigs Ann. Chem.* **118**, 151–177 (1861).
  78. Chou, H.-C., Leow, D. & Tan, C.-H. Recent Advances in Chiral Guanidine-Catalyzed Enantioselective Reactions. *Chem. An Asian J.* **14**, 3803–3822 (2019).
  79. Dong, S., Feng, X. & Liu, X. Chiral guanidines and their derivatives in asymmetric synthesis. *Chem. Soc. Rev.* **47**, 8525–8540 (2018).
  80. Zamperini, C. *et al.* Identification, synthesis and biological activity of alkyl-guanidine oligomers as potent antibacterial agents. *Sci. Rep.* **7**, 1–11 (2017).
  81. Drozdov, F. V. & Kotov, V. M. Guanidine: a Simple Molecule With Great Potential: From Catalysts To Biocides and Molecular Glues. *Ineos Open* **3**, 200–213 (2021).

82. Selig, P. Guanidine Organocatalysis. in *Synthesis* 703–718 (2013).
83. Brown, D. G., May-Dracka, T. L., Gagnon, M. M. & Tommasi, R. Trends and exceptions of physical properties on antibacterial activity for gram-positive and gram-negative pathogens. *J. Med. Chem.* **57**, 10144–10161 (2014).
84. Yukawa, T. & Naven, R. Utility of Physicochemical Properties for the Prediction of Toxicological Outcomes: Takeda Perspective. *ACS Med. Chem. Lett.* **11**, 203–209 (2020).
85. Price, D. A., Blagg, J., Jones, L., Greene, N. & Wager, T. Physicochemical drug properties associated with in vivo toxicological outcomes: A review. *Expert Opin. Drug Metab. Toxicol.* **5**, 921–931 (2009).
86. Kim, S. H., Semanya, D. & Castagnolo, D. Antimicrobial drugs bearing guanidine moieties: A review. *Eur. J. Med. Chem.* **216**, 113293 (2021).
87. Berlinck, R. G. S., Bernardi, D. I., Fill, T., Fernandes, A. A. G. & Jurberg, I. D. The chemistry and biology of guanidine secondary metabolites. *Nat. Prod. Rep.* **38**, 586–667 (2021).
88. Maccari, G. *et al.* Synthesis of linear and cyclic guazatine derivatives endowed with antibacterial activity. *Bioorg. Med. Chem. Lett.* **24**, 5525–5529 (2014).
89. Coqueiro, A., Regasini, L. O., Stapleton, P., Da Silva Bolzani, V. & Gibbons, S. In vitro antibacterial activity of prenylated guanidine alkaloids from *Pterogyne nitens* and synthetic analogues. *J. Nat. Prod.* **77**, 1972–1975 (2014).
90. Bairwa, R. *et al.* Novel molecular hybrids of cinnamic acids and guanylhydrazones as potential antitubercular agents. *Bioorg. Med. Chem. Lett.* **20**, 1623–1625 (2010).
91. Massimba-Dibama, H., Mourer, M., Constant, P., Daffé, M. & Regnouf-De-Vains, J. B. Guanidinium compounds with sub-micromolar activities against *Mycobacterium tuberculosis*. Synthesis, characterization and biological evaluations. *Bioorg. Med. Chem.* **23**, 5410–5418 (2015).
92. Deodato, D. *et al.* Biological Characterization and in Vivo Assessment of the Activity of a New Synthetic Macrocyclic Antifungal Compound. *J. Med. Chem.* **59**, 3854–3866 (2016).
93. Ajdačić, V. *et al.* Synthesis and evaluation of thiophene-based guanylhydrazones (iminoguanidines) efficient against panel of voriconazole-resistant fungal isolates. *Bioorg. Med. Chem.* **24**, 1277–1291 (2016).

94. Gros, E. *et al.* Netamines O-S, Five New Tricyclic Guanidine Alkaloids from the Madagascar Sponge *Biemna laboutei*, and Their Antimalarial Activities. *Chem. Biodivers.* **12**, 1725–1733 (2015).
95. Campos, P. E. *et al.* Unguiculin A and Ptilomycalins E-H, Antimalarial Guanidine Alkaloids from the Marine Sponge *Monanchora unguiculata*. *J. Nat. Prod.* **80**, 1404–1410 (2017).
96. Pietrobono, S. *et al.* Targeted inhibition of Hedgehog-GLI signaling by novel acylguanidine derivatives inhibits melanoma cell growth by inducing replication stress and mitotic catastrophe. *Cell Death Dis.* **9**, (2018).
97. Pogorzelska, A., Sławiński, J., Kawiak, A., Stasiłojć, G. & Chojnacki, J. Synthesis of 3-(2-Alkylthio-4-chloro-5-methylbenzenesulfonyl)-2-(1-phenyl-3-arylprop-2-enylideneamino)guanidine Derivatives with Pro-Apoptotic Activity against Cancer Cells. *Int. J. Mol. Sci.* **24**, (2023).
98. Kaul, M. *et al.* A bactericidal guanidinomethyl biaryl that alters the dynamics of bacterial FtsZ polymerization. *J. Med. Chem.* **55**, 10160–10176 (2012).
99. Nizalapur, S. *et al.* Amphipathic guanidine-embedded glyoxamide-based peptidomimetics as novel antibacterial agents and biofilm disruptors. *Org. Biomol. Chem.* **15**, 2033–2051 (2017).
100. Baltzer, S. A. & Brown, M. H. Antimicrobial peptides-promising alternatives to conventional antibiotics. *J. Mol. Microbiol. Biotechnol.* **20**, 228–235 (2011).
101. Sun, Q. & Sever, P. Amiloride: A review. *JRAAS - J. Renin-Angiotensin-Aldosterone Syst.* **21**, (2020).
102. Holmes, B., Brogden, R., Heel, R., Speight, T. & Avery, G. Guanabenz. A review of its pharmacodynamic properties and therapeutic efficacy in hypertension. *Drugs* **26**, 212–229 (1983).
103. Finnerty, F. A. J. & Brogden, R. N. Guanadrel. A review of its pharmacodynamic and pharmacokinetic properties and therapeutic use in hypertension. *Drugs* **30**, 22–31 (1985).
104. Houston, M. C. Clonidine hydrochloride. *South. Med. J.* **75**, 713–719 (1982).
105. Echizen, H. & Ishizaki, T. Clinical pharmacokinetics of famotidine. *Clin. Pharmacokinet.* **21**, 178–194 (1991).
106. Foretz, M., Guigas, B., Bertrand, L., Pollak, M. & Viollet, B. Metformin: From

- mechanisms of action to therapies. *Cell Metab.* **20**, 953–966 (2014).
107. Rasul, A. *et al.* Target Identification Approaches in Drug Discovery. in *Drug Target Selection and Validation* 41–59 (2022).
  108. Tabana, Y., Babu, D., Fahlman, R., Siraki, A. G. & Barakat, K. Target identification of small molecules: an overview of the current applications in drug discovery. *BMC Biotechnol.* **23**, 1–19 (2023).
  109. Mann, M., Kumar, C., Zeng, W. F. & Strauss, M. T. Artificial intelligence for proteomics and biomarker discovery. *Cell Syst.* **12**, 759–770 (2021).
  110. Rajczewski, A. T., Jagtap, P. D. & Griffin, T. J. An overview of technologies for MS-based proteomics-centric multi-omics. *Expert Rev. Proteomics* **19**, 165–181 (2022).
  111. Meissner, F., Geddes-McAlister, J., Mann, M. & Bantscheff, M. The Emerging Role of Mass Spectrometry-based Proteomics in Drug Discovery. *Nat. Rev. Drug Discov.* **In Press**, 1–55 (2021).
  112. Rix, U. & Superti-Furga, G. Target profiling of small molecules by chemical proteomics. *Nat. Chem. Biol.* **5**, 616–624 (2009).
  113. Evans, M. J. & Cravatt, B. F. Mechanism-based profiling of enzyme families. *Chem. Rev.* **106**, 3279–3301 (2006).
  114. Fonović, M. & Bogoy, M. Activity-based probes as a tool for functional proteomic analysis of proteases. *Expert Rev. Proteomics* **5**, 721–730 (2008).
  115. Moellering, R. E. & Cravatt, B. F. How chemoproteomics can enable drug discovery and development. *Chem. Biol.* **19**, 11–22 (2012).
  116. Wang, S. *et al.* Advanced activity-based protein profiling application strategies for drug development. *Front. Pharmacol.* **9**, 1–9 (2018).
  117. Conway, L. P., Li, W. & Parker, C. G. Chemoproteomic-enabled phenotypic screening. *Cell Chem. Biol.* **28**, 371–393 (2021).
  118. Bird, R. E., Lemmel, S. A., Yu, X. & Zhou, Q. A. Bioorthogonal Chemistry and Its Applications. *Bioconjug. Chem.* **32**, 2457–2479 (2021).
  119. Wu, P. The Nobel Prize in Chemistry 2022: Fulfilling Demanding Applications with Simple Reactions. *ACS Chem. Biol.* **17**, 2959–2961 (2022).
  120. Parker, C. G. & Pratt, M. R. Click Chemistry in Proteomic Investigations. *Cell* **180**, 605–632 (2020).

121. Fu, Q., Murray, C. I., Karpov, O. A. & Van Eyk, J. E. Automated proteomic sample preparation: The key component for high throughput and quantitative mass spectrometry analysis. *Mass Spectrom. Rev.* **42**, 873–886 (2023).
122. Becker, T. *et al.* Transforming Chemical Proteomics Enrichment into a High-Throughput Method Using an SP2E Workflow. *JACS Au* **2**, 1712–1723 (2022).
123. Fang, H. *et al.* Recent advances in activity-based probes (ABPs) and affinity-based probes (AfBPs) for profiling of enzymes. *Chem. Sci.* **12**, 8288–8310 (2021).
124. Geurink, P. P., Prely, L. M., Marel, G. A. van der, Bischoff, R. & Overkleeft, H. S. Photoaffinity Labeling in Activity-Based Protein Profiling. in *Activity-Based Protein Profiling* 85–113 (2011).
125. Pan, S., Zhang, H., Wang, C., Yao, S. C. L. & Yao, S. Q. Target identification of natural products and bioactive compounds using affinity-based probes. *Nat. Prod. Rep.* **33**, 612–620 (2016).
126. Wright, M. H. & Sieber, S. A. Chemical proteomics approaches for identifying the cellular targets of natural products. *Nat. Prod. Rep.* **33**, 681–708 (2016).
127. Niu, H. *et al.* Identification of agents active against methicillin-resistant staphylococcus aureus usa300 from a clinical compound library. *Pathogens* **6**, (2017).
128. Vaara, M. & Vaara, T. Polycations sensitize enteric bacteria to antibiotics. *Antimicrob. Agents Chemother.* **24**, 107–113 (1983).
129. Adang, A. E. P., Lucas, H., De Man, A. P. A., Engh, R. A. & Grootenhuis, P. D. J. Novel acylguanidine containing thrombin inhibitors with reduced basicity at the P1 moiety. *Bioorg. Med. Chem. Lett.* **8**, 3603–3608 (1998).
130. Storey, B. T., Sullivan, W. W. & Moyer, C. L. The pKa Values of Some 2-Aminomidazolium Ions. *J. Org. Chem.* **29**, 3118–3120 (1964).
131. Brook, I. Inoculum Effect. *Rev. Infect. Dis.* **11**, 361–368 (1989).
132. Bidlas, E., Du, T. & Lambert, R. J. W. An explanation for the effect of inoculum size on MIC and the growth/no growth interface. *Int. J. Food Microbiol.* **126**, 140–152 (2008).
133. Smith, K. P. & Kirby, J. E. The inoculum effect in the era of multidrug resistance: Minor differences in inoculum have dramatic effect on MIC Determination. *Antimicrob. Agents Chemother.* **62**, (2018).
134. Lenhard, J. R. & Bulman, Z. P. Inoculum effect of  $\beta$ -lactam antibiotics. *Journal of Antimicrobial Chemotherapy* vol. 74 2825–2843 (2019).



135. Meredith, H. R., Srimani, J. K., Lee, A. J., Lopatkin, A. J. & You, L. Collective antibiotic tolerance: Mechanisms, dynamics and intervention. *Nat. Chem. Biol.* **11**, 182–188 (2015).
136. Loffredo, M. R. *et al.* Inoculum effect of antimicrobial peptides. *Proc. Natl. Acad. Sci. U. S. A.* **118**, 1–10 (2021).
137. Udekwu, K. I., Parrish, N., Ankomah, P., Baquero, F. & Levin, B. R. Functional relationship between bacterial cell density and the efficacy of antibiotics. *J. Antimicrob. Chemother.* **63**, 745–757 (2009).
138. te Winkel, J. D., Gray, D. A., Seistrup, K. H., Hamoen, L. W. & Strahl, H. Analysis of antimicrobial-triggered membrane depolarization using voltage sensitive dyes. *Front. Cell Dev. Biol.* **4**, 1–10 (2016).
139. Kowalska-Krochmal, B. & Dudek-Wicher, R. The minimum inhibitory concentration of antibiotics: Methods, interpretation, clinical relevance. *Pathogens* **10**, 1–21 (2021).
140. Rhee, K. Y. & Gardiner, D. F. Clinical relevance of bacteriostatic versus bactericidal activity in the treatment of gram-positive bacterial infections [2]. *Clin. Infect. Dis.* **39**, 755–756 (2004).
141. CLSI. *Methods for Dilution Antimicrobial Susceptibility Tests for Bacteria That Grow Aerobically; Approved Standard — Ninth Edition.* vol. 32 (2012).
142. Fernandes, P. B. *et al.* The frequency of in-vitro resistance development to fluoroquinolones and the use of a murine pyelonephritis model to demonstrate selection of resistance in vivo. *J. Antimicrob. Chemother.* **19**, 449–465 (1987).
143. Kaatz, G. W., Seo, S. M. & Ruble, C. A. Efflux-mediated fluoroquinolone resistance in *Staphylococcus aureus*. *Antimicrob. Agents Chemother.* **37**, 1086–1094 (1993).
144. Neyfakh, A. A., Borsch, C. M. & Kaatz, G. W. Fluoroquinolone resistance protein NorA of *Staphylococcus aureus* is a multidrug efflux transporter. *Antimicrob. Agents Chemother.* **37**, 128–129 (1993).
145. Li, H. Minimap2: Pairwise alignment for nucleotide sequences. *Bioinformatics* **34**, 3094–3100 (2018).
146. Poole, K. Efflux pumps as antimicrobial resistance mechanisms. *Ann. Med.* **39**, 162–176 (2007).
147. Kumar, S. *et al.* Functional and structural roles of the major facilitator superfamily bacterial multidrug efflux pumps. *Microorganisms* **8**, (2020).

148. Dashtbani-Roozbehani, A. & Brown, M. H. Efflux pump mediated antimicrobial resistance by staphylococci in health-related environments: Challenges and the quest for inhibition. *Antibiotics* **10**, (2021).
149. Fey, P. D. *et al.* A genetic resource for rapid and comprehensive phenotype screening of nonessential *Staphylococcus aureus* genes. *MBio* **4**, (2013).
150. Schmitz, F. J. *et al.* The effect of reserpine, an inhibitor of multidrug efflux pumps, on the in-vitro activities of ciprofloxacin, sparfloxacin and moxifloxacin against clinical isolates of *Staphylococcus aureus*. *J. Antimicrob. Chemother.* **42**, 807–810 (1998).
151. Szklarczyk, D. *et al.* STRING v11: Protein-protein association networks with increased coverage, supporting functional discovery in genome-wide experimental datasets. *Nucleic Acids Res.* **47**, D607–D613 (2019).
152. Belcheva, A. & Golemi-Kotra, D. A close-up view of the *VraSR* two-component system: A mediator of *Staphylococcus aureus* response to cell wall damage. *J. Biol. Chem.* **283**, 12354–12364 (2008).
153. Gardete, S., Wu, S. W., Gill, S. & Tomasz, A. Role of *VraSR* in antibiotic resistance and antibiotic-induced stress response in *Staphylococcus aureus*. *Antimicrob. Agents Chemother.* **50**, 3424–3434 (2006).
154. Yin, S., Daum, R. S. & Boyle-Vavra, S. *VraSR* two-component regulatory system and its role in induction of *pbp2* and *vraSR* expression by cell wall antimicrobials in *Staphylococcus aureus*. *Antimicrob. Agents Chemother.* **50**, 336–343 (2006).
155. Kuroda, M. *et al.* Two-component system *VraSR* positively modulates the regulation of cell-wall biosynthesis pathway in *Staphylococcus aureus*. *Mol. Microbiol.* **49**, 807–821 (2003).
156. Matsumoto, Y. *et al.* A critical role of mevalonate for peptidoglycan synthesis in *Staphylococcus aureus*. *Sci. Rep.* **6**, 1–14 (2016).
157. Paetzel, M., Karla, A., Strynadka, N. C. J. & Dalbey, R. E. Signal peptidases. *Chem. Rev.* **102**, 4549–4579 (2002).
158. Schimana, J. *et al.* Arylomycins A and B, new biaryl-bridged lipopeptide antibiotics produced by *Streptomyces* sp. Tü 6075. I. Taxonomy, fermentation, isolation and biological activities. *J. Antibiot. (Tokyo)*. **55**, 565–570 (2002).
159. Kulanthaivel, P. *et al.* Novel lipoglycopeptides as inhibitors of bacterial signal peptidase I. *J. Biol. Chem.* **279**, 36250–36258 (2004).

160. Smith, P. A. *et al.* Optimized arylomycins are a new class of Gram-negative antibiotics. *Nature* **561**, 189–194 (2018).
161. Wang, X., Zhou, B., Hu, W., Zhao, Q. & Lin, Z. Formation of active inclusion bodies induced by hydrophobic self-assembling peptide GFIL8. *Microb. Cell Fact.* **14**, 1–8 (2015).
162. Zhou, B., Xing, L., Wu, W., Zhang, X. E. & Lin, Z. Small surfactant-like peptides can drive soluble proteins into active aggregates. *Microb. Cell Fact.* **11**, 2–9 (2012).
163. Chen, S. *et al.* Unraveling the mechanism of small molecule induced activation of Staphylococcus aureus signal peptidase IB Check for updates. *Commun. Biol.* **7**, 895 (2024).
164. Hadkar, U. B. & Hadkar, A. S. Critical micelle concentration of surfactant using hadkar factor. *Indian J. Pharm. Educ. Res.* **49**, 134–139 (2015).
165. Dai, S. & Tam, K. C. Isothermal titration calorimetric studies of alkyl phenol ethoxylate surfactants in aqueous solutions. *Colloids Surfaces A Physicochem. Eng. Asp.* **229**, 157–168 (2003).
166. Chattopadhyay, A. & Harikumar, K. G. Dependence of critical micelle concentration of a zwitterionic detergent on ionic strength: Implications in receptor solubilization. *FEBS Lett.* **391**, 199–202 (1996).
167. Qin, X., Liu, M., Yang, D. & Zhang, X. Concentration-dependent aggregation of CHAPS investigated by NMR spectroscopy. *J. Phys. Chem. B* **114**, 3863–3868 (2010).
168. Humphrey, W., Dalke, A. & Schulten, K. VMD: Visual Molecular Dynamics. *J. Mol. Graph.* **14**, 33–38 (1996).
169. Zanon, P. R. A., Lewald, L. & Hacker, S. M. Isotopically Labeled Desthiobiotin Azide (isoDTB) Tags Enable Global Profiling of the Bacterial Cysteinome. *Angew. Chem. Int. Ed.* **59**, 2829–2836 (2020).
170. Zanon, P. R. A. *et al.* Profiling the proteome-wide selectivity of diverse electrophiles. *ChemRxiv* **1**, 1–10 (2021).
171. Kong, A. T., Lprevost, F. V., Avtonomov, D. M., Mellacheruvu, D. & Nesvizhskii, A. I. MSFragger: Ultrafast and comprehensive peptide identification in mass spectrometry-based proteomics. *Nat. Methods* **14**, 513–520 (2017).
172. Chang, H.-Y. *et al.* Crystal-C: A computational tool for refinement of open search

- results. *J. Proteome Res.* **19**, 2511–2515 (2021).
173. Yu, F. *et al.* Identification of modified peptides using localization-aware open search. *Nat. Commun.* **11**, 1–9 (2020).
  174. Teo, G. C., Polasky, D. A., Yu, F. & Nesvizhskii, A. I. Fast Deisotoping Algorithm and Its Implementation in the MSFragger Search Engine. *J. Proteome Res.* **20**, 498–505 (2021).
  175. Geiszler, D. J. *et al.* PTM-Shepherd: analysis and summarization of post-translational and chemical modifications from open search results. *bioRxiv* **353**, 1–31 (2010).
  176. Kanehisa, M. & Goto, S. KEGG: Kyoto Encyclopedia of Genes and Genomes. *Nucleic Acids Res.* **28**, 27–30 (2000).
  177. Apweiler, R. *et al.* UniProt: the Universal Protein knowledgebase. *Nucleic Acids Res.* **32**, (2004).
  178. Bateman, A. *et al.* UniProt: the universal protein knowledgebase in 2021. *Nucleic Acids Res.* **49**, D480–D489 (2021).
  179. Smith, P. A. & Romesberg, F. E. Mechanism of action of the arylomycin antibiotics and effects of signal peptidase I inhibition. *Antimicrob. Agents Chemother.* **56**, 5054–5060 (2012).
  180. O'Neill, A. J., Cove, J. H. & Chopra, I. Mutation frequencies for resistance to fusidic acid and rifampicin in *Staphylococcus aureus*. *J. Antimicrob. Chemother.* **47**, 647–650 (2001).
  181. Bushnell, B., Rood, J. & Singer, E. BBMerge – Accurate paired shotgun read merging via overlap. *PLoS One* **12**, 1–15 (2017).
  182. Bankevich, A. *et al.* SPAdes: A new genome assembly algorithm and its applications to single-cell sequencing. *J. Comput. Biol.* **19**, 455–477 (2012).
  183. Mann, M., Coscia, F. & Al., E. A streamlined mass spectrometry based proteomics workflow for large-scale FFPE.pdf. *The Journal of Pathology* - (2020).
  184. Demichev, V., Messner, C. B., Vernardis, S. I., Lilley, K. S. & Ralser, M. DIA-NN: neural networks and interference correction enable deep proteome coverage in high throughput. *Nat. Methods* **17**, 41–44 (2020).
  185. Tyanova, S. *et al.* The Perseus computational platform for comprehensive analysis of (prote)omics data. *Nat. Methods* **13**, 731–740 (2016).

186. Perez-Riverol, Y. *et al.* The PRIDE database resources in 2022: A hub for mass spectrometry-based proteomics evidences. *Nucleic Acids Res.* **50**, D543–D552 (2022).
187. Kessner, D., Chambers, M., Burke, R., Agus, D. & Mallick, P. ProteoWizard: Open source software for rapid proteomics tools development. *Bioinformatics* **24**, 2534–2536 (2008).
188. da Veiga Leprevost, F. *et al.* Philosopher: a versatile toolkit for shotgun proteomics data analysis. *Nat. Methods* **17**, 869–870 (2020).
189. Yu, F., Haynes, S. E. & Nesvizhskii, A. I. IonQuant enables accurate and sensitive label-free quantification with FDR-controlled match-between-runs. *Mol. Cell. Proteom* **20**, 100077 (2021).
190. Therien, A. G. *et al.* Broadening the Spectrum of  $\beta$ -Lactam Antibiotics through Inhibition of Signal Peptidase Type I. *Antimicrob. Agents Chemother.* **56**, 4662–4670 (2012).
191. Rao, S. *et al.* Enzymatic investigation of the *Staphylococcus aureus* type i signal peptidase SpsB - Implications for the search for novel antibiotics. *FEBS J.* **276**, 3222–3234 (2009).
192. Trott, O. & Olson, A. J. AutoDock Vina: Improving the speed and accuracy of docking with a new scoring function, efficient optimization, and multithreading. *J. Comput. Chem.* **31**, 455–461 (2010).
193. Lee, J. *et al.* CHARMM-GUI Input Generator for NAMD, GROMACS, AMBER, OpenMM, and CHARMM/OpenMM Simulations Using the CHARMM36 Additive Force Field. *J. Chem. Theory Comput.* **12**, 405–413 (2016).
194. Tian, C. *et al.* Ff19SB: Amino-Acid-Specific Protein Backbone Parameters Trained against Quantum Mechanics Energy Surfaces in Solution. *J. Chem. Theory Comput.* **16**, 528–552 (2020).
195. Dickson, C. J., Walker, R. C. & Gould, I. R. Lipid21: Complex Lipid Membrane Simulations with AMBER. *J. Chem. Theory Comput.* **18**, 1726–1736 (2022).
196. Wang, J., Wolf, R. M., Caldwell, J. W., Kollman, P. A. & Case, D. A. Development and testing of a general Amber force field. *J. Comput. Chem.* **25**, 1157–1174 (2004).
197. Izadi, S., Anandakrishnan, R. & Onufriev, A. V. Building Water Models: A Different Approach. *J. Phys. Chem. Lett.* **5**, 3863–3871 (2014).

198. Jakalian, A., Bush, B. L., Jack, D. B. & Bayly, C. I. Fast, Efficient Generation of High-Quality Atomic Charges. AM1-BCC Model: I. Method. *Journal of Computational Chemistry* vol. 21 132–146 (2000).
199. Wang, J., Wang, W., Kollman, P. A. & Case, D. A. Automatic atom type and bond type perception in molecular mechanical calculations. *J. Mol. Graph. Model.* **25**, 247–260 (2006).
200. Case, D. A. *et al.* Amber 2022. University of California, San Francisco. (2022).
201. Goga, N., Rzepiela, A. J., De Vries, A. H., Marrink, S. J. & Berendsen, H. J. C. Efficient algorithms for langevin and DPD dynamics. *J. Chem. Theory Comput.* **8**, 3637–3649 (2012).
202. Berendsen, H. J. C., Postma, J. P. M., Van Gunsteren, W. F., Dinola, A. & Haak, J. R. Molecular dynamics with coupling to an external bath. *J. Chem. Phys.* **81**, 3684–3690 (1984).
203. Andersen, H. C. Rattle: A ‘velocity’ version of the shake algorithm for molecular dynamics calculations. *J. Comput. Phys.* **52**, 24–34 (1983).
204. Balusek, C. *et al.* Accelerating Membrane Simulations with Hydrogen Mass Repartitioning. *J. Chem. Theory Comput.* **15**, 4673–4686 (2019).
205. Roe, D. R. & Cheatham, T. E. PTRAJ and CPPTRAJ: Software for processing and analysis of molecular dynamics trajectory data. *J. Chem. Theory Comput.* **9**, 3084–3095 (2013).

## 7. License Agreement

*JACS Au* 2024, 4, 8, 3125–3134

<https://doi.org/10.1021/jacsau.4c00449>

Published July 16, 2024

Copyright © 2024 The Authors. Published by American Chemical Society. This publication is licensed under

[CC-BY 4.0](https://creativecommons.org/licenses/by/4.0/).